Laser and Particle Beams (2012), *30*, 117–174.

doi:10.1017/S0263034611000644

The Current Trends in SBS and phase conjugation

T. OMATSU,[1] H.J. KONG,[2] S. PARK,[2] S. CHA,[2] H. YOSHIDA,[3] K. TSUBAKIMOTO,[3] H. FUJITA,[3] N. MIYANAGA,[3] M. NAKATSUKA,[3] Y. WANG,[4] Z. LU,[4] Z. ZHENG,[4] Y. ZHANG,[4] M. KALAL,[5] O. SLEZAK,[5] M. ASHIHARA,[1] T. YOSHINO,[1] K. HAYASHI,[1] Y. TOKIZANE,[1] M. OKIDA,[1] K. MIYAMOTO,[1] K. TOYODA,[1] A.A. GRABAR,[6] Md. M. KABIR,[7] Y. OISHI,[7] H. SUZUKI,[7] F. KANNARI,[7] C. SCHAEFER,[8] K.R. PANDIRI,[9] M. KATSURAGAWA,[9] Y.L. WANG,[4] Z.W. LU,[4] S.Y. WANG,[4] Z.X. ZHENG,[4] W.M. HE,[4] D.Y. LIN,[4] W.L.J. HASI,[4] X.Y. GUO,[4] H.H. LU,[4] M.L. FU,[4] S. GONG,[4] X.Z. GENG,[4] R.P. SHARMA,[10] P. SHARMA,[10] S. RAJPUT,[10] A.K. BHARDWAJ,[11] C.Y. ZHU,[4] AND W. GAO[12]

[1]Graduate School of Advanced Integration Science, Chiba University, Chiba, Japan
[2]Department of Physics, Korea Advanced Institute of Science and Technology, Daejeon, Republic of Korea
[3]Institute of Laser Engineering, Osaka University, Osaka, Japan
[4]Harbin Institute of Technology, Harbin, China
[5]Faculty of Nuclear Sciences and Physical Engineering, Czech Technical University, Prague, Czech Republic
[6]Uzhgood National University, Ukraine
[7]Department of Electronics and Electrical Engineering, Keio University, Yokohama, Japan
[8]National Institute of Information and Communication Technology, Tokyo, Japan
[9]University of Electro-Communications, Chofu, Japan
[10]Centre for Energy Studies, Indian Institute of Technology, New Delhi, India
[11]N.S.C.B. Government Post Graduate College, Biaora, India
[12]Department of Optics information Science and Technology, Harbin University of Science and Technology, Harbin, China

(RECEIVED 7 July 2011; ACCEPTED 10 October 2011)

Abstract

The current trends in stimulated Brillouin scattering and optical phase conjugation are overviewed. This report is formed by the selected papers presented in the "Fifth International Workshop on stimulated Brillouin scattering and phase conjugation 2010" in Japan. The nonlinear properties of phase conjugation based on stimulated Brillouin scattering and photorefraction can compensate phase distortions in the high power laser systems, and they will also open up potentially novel laser technologies, e.g., phase stabilization, beam combination, pulse compression, ultrafast pulse shaping, and arbitrary waveform generation.

Keywords: Beam combination; Laser amplification; Laser oscillators; Optical fibers; Phase conjugate mirror; Phase control; Pulse compression; Photorefractive nonlinear optics; Stimulated Brillouin scattering

1. PHASE CONTROLLED SBS-PCM AND ITS APPLICATION TO A COHERENT BEAM COMBINATION LASER (H.J. Kong, S. Park, and S. Cha)

1.1. Introduction

People swiftly began researching the inertial confinement fusion using a high power laser, but after more than 50 years, we are finally on the verge of a milestone. The National Ignition Facility at Lawrence Livermore National Laboratory is now delivering its full potential of 4.2 MJ and it will be the first machine on earth that will achieve a controlled ignition of fusion (Moses, 2009). On the other hand, for practical inertial fusion energy, there is a race on increasing the output energy of high repetition rate laser (Zheng *et al.*, 2008; Albach *et al.*, 2008; Chanteloup *et al.*, 2010). Inertial fusion is not the only objective of lasers with high power and high repetition rate. There are many research fields that utilizes the high power and high repetition rate laser such as laser acceleration of particles, high energy density states of matter, laser induced plasma generation, X-ray and extreme ultraviolet generation (Batanov *et al.*, 1972; Tajima & Dawson, 1979; Jin & Richardson, 1995; Salamin *et al.*, 2006). There are also many applications in

Address correspondence and reprint requests to: Hong Jim Kong, Department of Physics, KAIST, 373-1 Gusong-dong, Yusong-gu Daejon, Korea 305-701. E-mail: hjkong@kaist.ac.kr

industry such as laser processing of materials, laser peening, next generation lithography using extreme ultraviolet, and medical lasers (Spalding, 1978; Masse & Barreau, 1995; Sumiyoshi *et al*., 1999; Salamin *et al*., 2008).

To increase the output energy of a laser while maintaining its repetition rate, researchers tried many techniques. They researched on laser materials (cryogenic Yb:YAG and ceramic Nd:YAG), pumping methods (laser diode pumping), and advanced laser schemes (beam combining, fiber laser) (Zhou *et al.*, 1985; Barnes *et al.*, 1990; Kong *et al.*, 1997; Ikesue, 2002; Limpert *et al.*, 2005; Lee *et al.*, 2007; Kawanaka *et al.*, 2010). Among these, the most practical solution for the laser fusion driver is the beam combination laser using stimulated Brillouin scattering-phase conjugate mirror (SBS-PCM) due to its unlimited scalability without thermal problems (Kong *et al.*, 1997, 2005*b*, 2005*c*, 2005*d*). Like other beam combination techniques, it can be operated with a high repetition rate over 10 Hz since only small amplifiers are needed to obtain the high output energy. Also, SBS-PCM can compensate a wavefront distortion automatically and removes a need of complicated and expensive deformable mirrors (Rockwell, 1988). Finally, the self-phase locking of SBS-PCM enables the separate phase controlling/locking of each beam lines (Kong *et al.*, 1997, 2005*b*, 2005*d*); thereby the number of beams can be increased without limit in the number of beams.

In this work, we introduce key concepts of the beam combination laser using the SBS-PCM with necessary experiments. After that, we present four beam combining results, both with and without amplifiers. Recent progresses on a prepulse technique of the SBS-PCM will also be showed.

1.2. Progresses and Experimental Results

1.2.1. Beam Combination Laser Using Self-Phase Controlled SBS-PCM

The self-phase controlling/locking of SBS-PCM is the most important feature of the coherent beam combination laser using SBS-PCM. Since a phase conjugate wave of the normal SBS-PCM is originated from an acoustic noise in the medium, it has a random phase with respect to a phase of the input beam (Rockwell, 1988; Boyd *et al.*, 1990). Figure 1 shows the schemes of the self-phase locking. Feedback mirror is installed at the back side of the SBS-PCM and the interference between the original beam and the returning beam makes an optical standing wave at the focus. The optical standing wave ignites and generates a moving Bragg grating by electrostriction at the right moment. The phase conjugate wave of the self-phase controlled SBS-PCM is originated from this moving Bragg grating and has a definite phase. It is proved that the self-phase controlling/locking of SBS-PCM effectively locks and controls the phase of the SBS wave with a very simple optical configuration (Kong *et al.*, 1997).

Figures 2 and 3 shows the proposed scheme of the coherent beam combination laser using SBS-PCMs with the wavefront dividing and the amplitude dividing schemes, respectively. Cross-type feature of the scheme is treated heavily in a previous review (Kong *et al.*, 2007*a*) and we will concentrate on the amplifier arm in this work.

When a beam enters the beam combination amplifier stage, it is separated into several sub-beams. In the wavefront dividing scheme, the input beam is divided spatially by an apertures and prisms. In the amplitude dividing scheme, the input beam is divided energetically by wave-plates and polarizing beam splitters (PBSs). Each of the sub-beams passes through an amplifier and a Faraday rotator. The Faraday rotator not only rotates the polarization of the beam, but also compensates thermal depolarization induced by the amplifier in the double pass configuration (Han & Kong, 1995). Finally, sub-beams are combined into the output beam coherently.

1.2.1.1. Compensation of Thermal Depolarization. Thermally induced birefringence (TIB) is one of the most significant thermal effects seen in the amplifiers. It is known that among four configurations given in Figure 4, only Figure 4d would

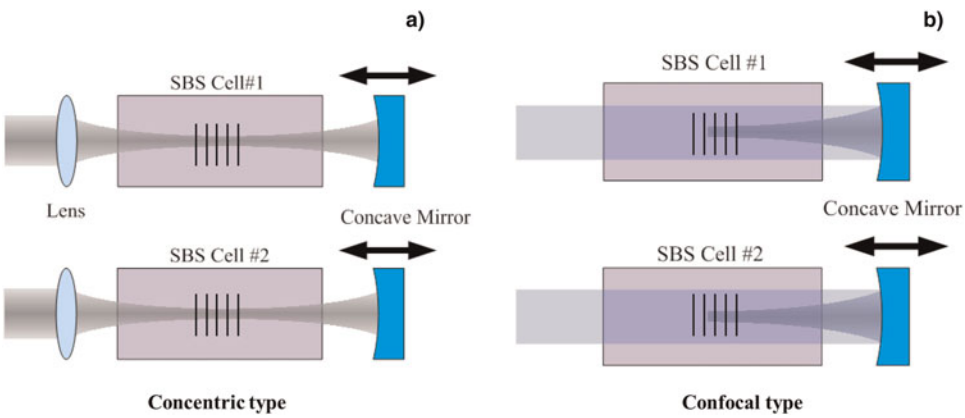

Fig. 1. (Color online) The proposed scheme of the self-phase controlling method. Counter-propagation beams from the feedback mirror and incident beams make a standing density modulation in the SBS-medium. Standing density modulation locks the ignition position of moving Bragg grating, and the Bragg grating locks the phase of the SBS-wave.

https://doi.org/10.1017/S0263034611000644 Published online by Cambridge University Press

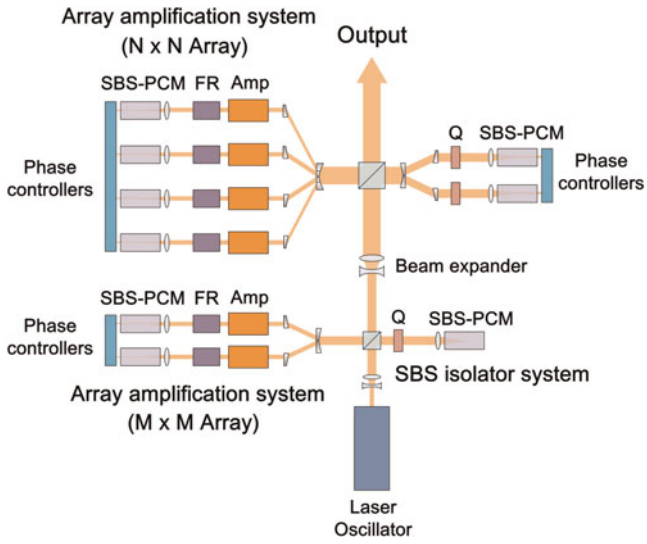

Fig. 2. (Color online) The experimental setup of the beam-combined laser system with the wavefront dividing scheme. The beam is divided by prisms. PBS = polarized beam splitter; FR = Faraday rotator; Amp = amplifier; Q = quarter wave plate.

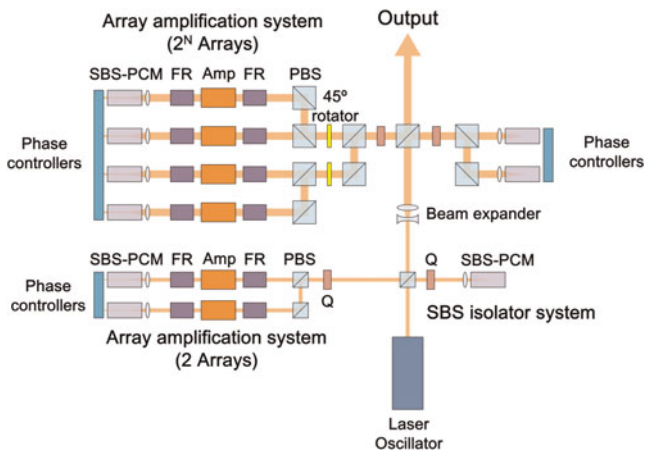

Fig. 3. (Color online) The experimental setup of the beam-combined laser system with the amplitude dividing scheme. The beam is divided by PBSs. PBS = polarized beam splitter; FR = Faraday rotator; Amp = amplifier; Q = quarter wave plate.

completely compensate depolarization effect by TIB with a 90° rotated polarization (Han & Kong, 1995).

Figure 4 shows the experimental setup for the measurement of the leak beam patterns and the depolarization ratios using the four possible optical schemes in a double-pass Nd:YAG amplifier with an SBS-PCM (Shin *et al.*, 2010*a*). The laser beam from the 1064 nm pulsed Nd:YAG oscillator has a quasi-Gaussian shape with a beam diameter of 8 mm. This beam is double-pass amplified using the four possible schemes with the help of an SBS-PCM as a reflector. The electrical input energy to the pumping flashlamp is adjustable from 0 to 37.5 J. After the laser amplification, small depolarized part of the output beam passes through

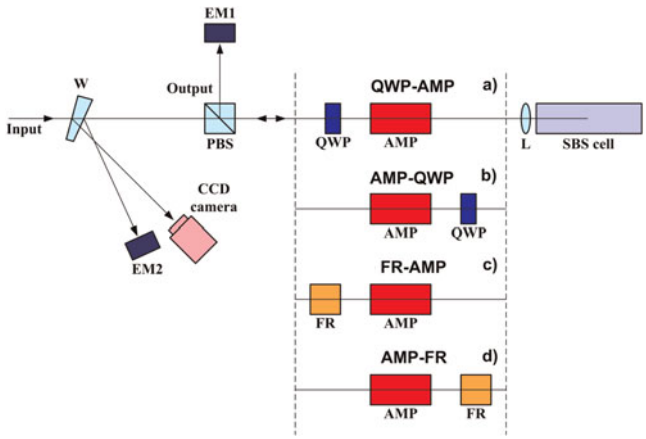

Fig. 4. (Color online) Experimental setup for the measurement of the leak beam patterns and the depolarization ratio for the four possible optical schemes in a double-pass Nd:YAG rod amplifier with a SBS-PCM (W = wedged window; EM1 and EM2 = energy meters; PBS = polarizing beam splitter; QWP = quarter wave plate; AMP = Nd:YAG rod amplifier; FR = Faraday rotator; L = lens). (**a**) QWP-AMP (quarter wave plate located before the amplifier), (**b**) AMP-QWP (quarter wave plate located after the amplifier), (**c**) FR-AMP (Faraday rotator located after the amplifier), (**d**) AMP-FR (Faraday rotator located before the amplifier).

the PBS with a *p*-polarization. An optical wedge is located before the PBS and reflects a small amount of the beam. An energy meter measures the energy and a charge coupled device camera measures the beam pattern.

Figure 5 shows the depolarization ratios versus the electrical input energy for the four different optical schemes. Figure 5 also shows the theoretical fits from the Jones matrix calculation with a Faraday rotation angle of 44.3°. Figure 6 shows the theoretically and experimentally obtained leak beam patterns when the electrical input energy is 30.4 J. The theoretical leak beam patterns are obtained from the Jones matrix calculations and the fitted value. The results

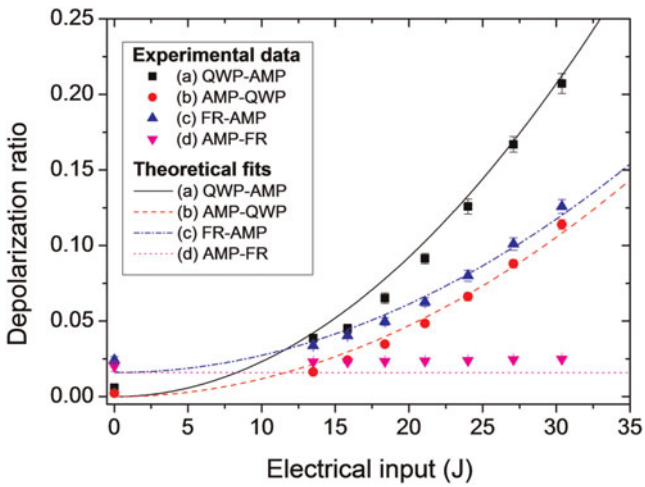

Fig. 5. (Color online) Experimental data and theoretical fits of the depolarization ratios versus the electrical input energy to the Xenon flashlamp for the four different optical schemes. (**a**) QWP-AMP, (**b**) AMP-QWP, (**c**) FR-AMP, (**d**) AMP-FR.

https://doi.org/10.1017/S0263034611000644 Published online by Cambridge University Press

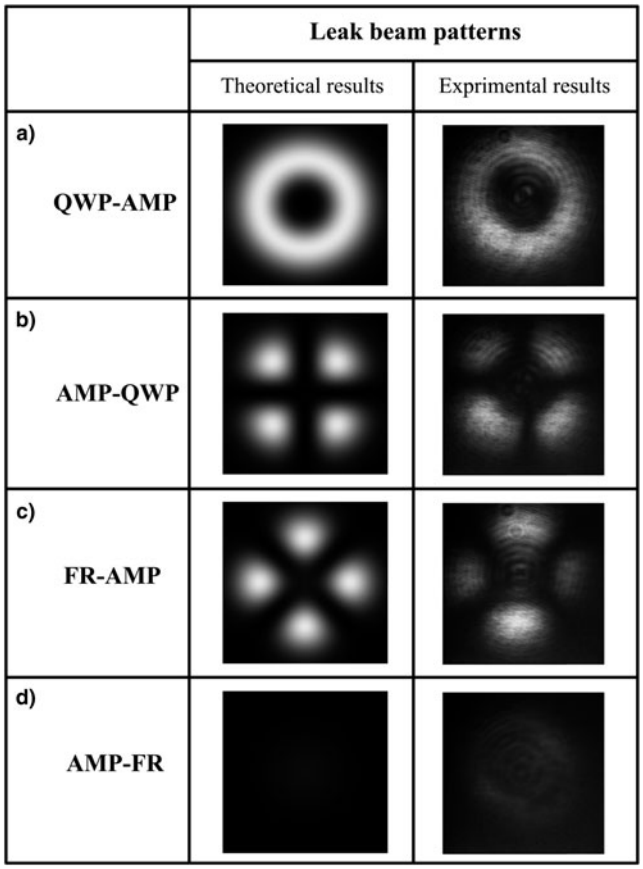

Fig. 6. Theoretically and experimentally obtained leak beam patterns for the four possible optical schemes when the electrical input energy to the Xenon flashlamp is 30.4 J. (**a**) QWP-AMP, (**b**) AMP-QWP, (**c**) FR-AMP, (**d**) AMP-FR.

show a good agreement between the theoretical and experimental results.

1.2.1.2. Feedback Control of Long-Term Phase Fluctuation. Due to the air fluctuations and other effects, lengths of the sub-beam paths are varying in long term. It can be seen as slowly changing relative phase between the beams. A typical time scale is much larger than the period of the laser pulses (0.1 s).

To solve this long-term problem, we actively control the beam path lengths using piezoelectric translator (PZT) (Kong *et al.*, 2006, 2008). At first, the relative phases between the beams are measured from the interference pattern between the sub-beams or by measuring the relative polarization components of the combined beam. Using the measured relative phases, the position of the feedback mirror is adjusted by applying the feedback voltages to the attached PZTs. Note that the process is done between the pulses. Therefore expensive real-time modules are unnecessary. The control of long-term phase fluctuation extends the period of phase locking from less than a minute to an hour or more.

1.2.1.3. Two Beam Combination Laser — Wavefront Dividing Scheme. Figure 7 shows the experimental setup of the two

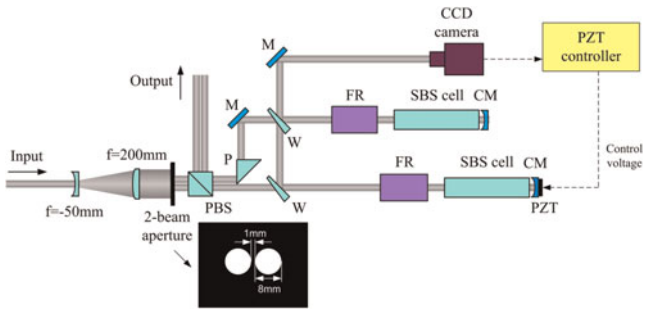

Fig. 7. (Color online) The experimental setup for the long-term phase stabilization assessment in the wavefront dividing scheme. PBS = polarizing beam splitter; M = mirror; W = wedged window; FR = Faraday rotator; CM = concave mirror; PZT = piezoelectric translator.

beam combination laser with the wavefront dividing scheme. The laser beam is expanded by a beam expander, which consists of a pair of lenses. The beam is expanded four times and passes through the aperture. The aperture divides the beam into two beams. Two beams pass through the PBS, and one beam line is reflected from the prism and the mirror to the SBS-PCM. Another beam propagates through the PBS and the Faraday rotator. Two beams are reflected from the SBS-PCMs, and the reflected beams are split by the wedges. The length of the SBS cell is 300 mm, and the radius of curvature of the feedback convex mirror is 300 mm. The charge-coupled device camera detects the interference pattern of the two beams and calculates the relative phase to make the input voltage into the PZT controller. The PZT controller adjusts the position of the feedback mirror with the PZT.

Without the long-term phase control, Figure 8 shows the relative phase and the output energy measured during 1000 shots (100 s). It shows the slow varying relative phase and

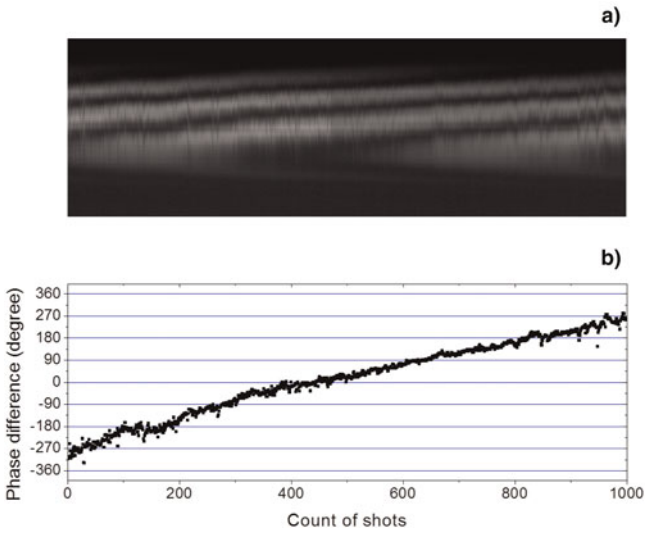

Fig. 8. The experimental results of the wavefront dividing two-beam combination without long-term phase stabilization. (**a**) Mosaic intensity profile of the horizontal lines from interference patterns during 1000 shots. (**b**) The phase difference during 1000 shots.

https://doi.org/10.1017/S0263034611000644 Published online by Cambridge University Press

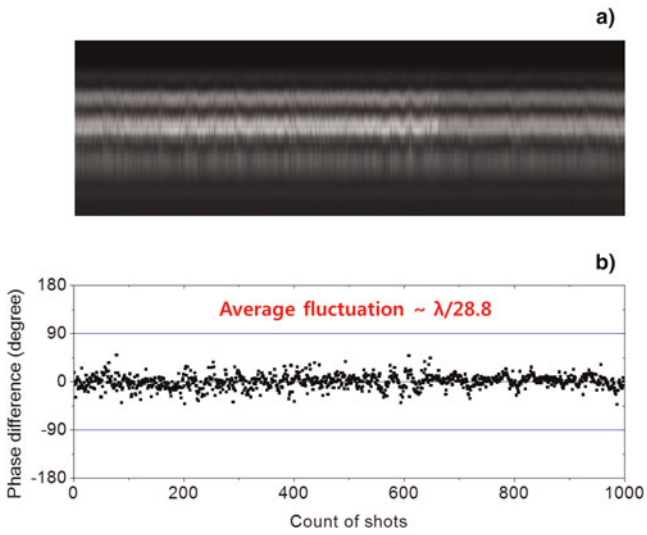

Fig. 9. (Color online) The experimental results of the wavefront dividing two-beam combination with long-term phase stabilization. (**a**) Mosaic intensity profile of the horizontal lines from interference patterns during 1000 shots. (**b**) The phase difference during 1000 shots. The standard deviation of the phase difference is λ/28.8.

the output energy. With the long-term phase control, Figure 9 shows the relative phase and the output energy measured during 1000 shots (250 s). The phase fluctuation is λ/28.8 in standard deviation, and the output energy is stabilized near its maximum value.

1.2.1.4. Two Beam Combination Laser — Amplitude Dividing Scheme. Figure 10 shows the experimental setup of the two beam combination laser with the amplitude dividing scheme. The laser beam passes through the isolator, the PBS, the Faraday rotators, the half wave plate (HWP). After that, the beam propagates through the PBS, the FR, and the BS. The beam is split into two beams by the PBS and reflected from the SBS-PCMs. The reflected beam is split by the BS, passes through the quarter wave plate (QWP), and is split into two beams again by the PBS. The

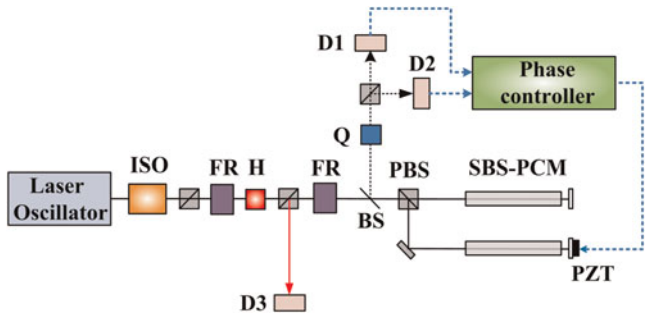

Fig. 10. (Color online) The experimental setup of the long-term phase stabilization assessment with the amplitude dividing scheme without amplifiers. ISO = isolator; FR = Faraday rotator; H = half wave plate; Q = Quarter wave plate; BS = Beam splitter; PBS = Polarized beam splitter; D1-D3 = Detector.

divided beams are measured in terms of their energy by the detectors, D1 and D2.

Without the long-term phase control, Figure 11 shows the relative phase and the output energy measured during 2500 shots (250 s). It shows the slowly varying relative phase and the output energy. With the long-term phase control, Figure 12 shows the relative phase and the output energy measured during 2500 shots (250 s). The phase fluctuation is λ/46.7 in standard deviation, and the output energy is stabilized near its maximum value.

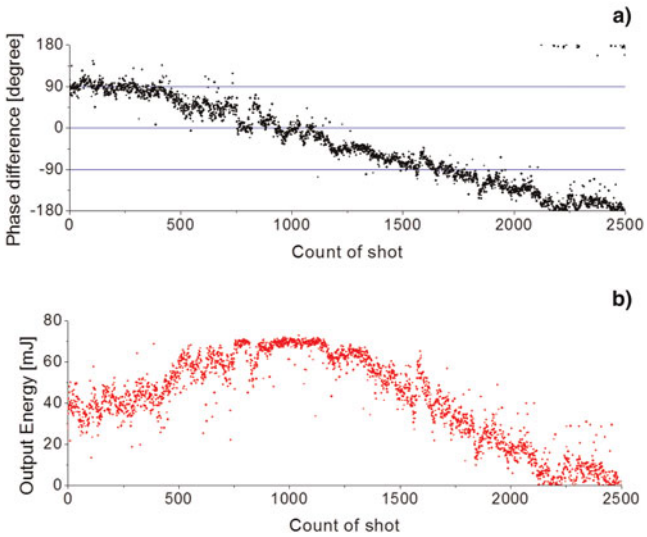

Fig. 11. (Color online) The experimental results of the amplitude dividing two-beam combination without long-term phase stabilization. (**a**) Phase difference during 2500 shots. (**b**) Output energy during 2500 shots.

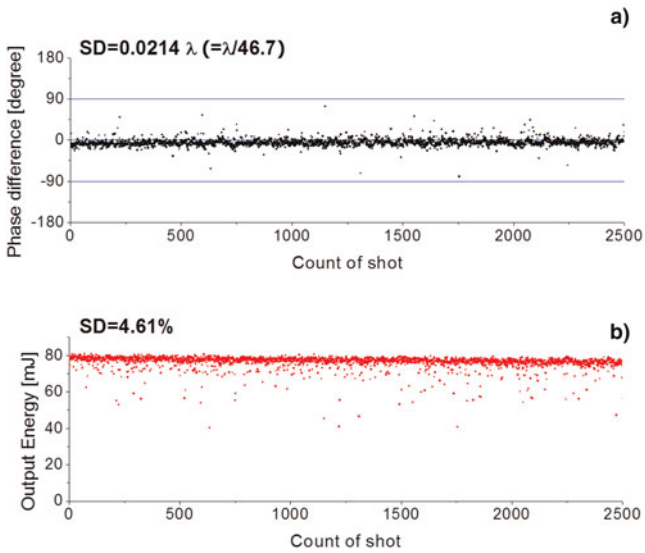

Fig. 12. (Color online) The experimental results of the amplitude dividing two-beam combination with long-term phase stabilization. (**a**) Phase difference during 2500 shots. The standard deviation of the phase difference is λ/46.7. (**b**) Output energy during 2500 shots. Maximum energy is 80.9 mJ, and median energy is 77.1 mJ, Mean energy is 76.3 mJ.

https://doi.org/10.1017/S0263034611000644 Published online by Cambridge University Press

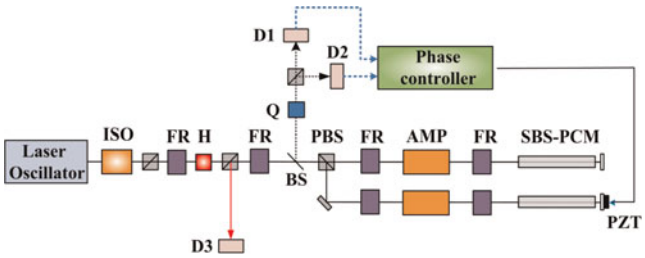

Fig. 13. (Color online) The experimental setup of the long-term phase stabilization assessment with the amplitude dividing scheme with amplifiers. ISO = isolator; FR = Faraday rotator; AMP = amplifier; H = half wave plate; Q = Quarter wave plate; BS = Beam splitter; PBS = Polarized beam splitter; D1-D3 = Detector; PZT = piezoelectric transducer.

Figure 13 shows the experimental setup in which the Faraday rotators and the amplifiers are added to Figure 10. This setup is designed to investigate the coherent beam combination characteristics during the laser amplification process. Figure 14 shows the result with the PZT control during 2500 shots (250 s). The phase fluctuation is $\lambda/22.5$ and the standard deviation of the output energy is 7.18%.

1.2.2. *Coherent Four Beam Combination Laser Using SBS-PCM*

Two beam coherent combination lasers can represent the scalability that is one of the most important features of the beam combination laser using SBS-PCM. Moreover, the relative phase between the two sub-beams can be measured by using simple interferogram between the beams. On the other hand, four beam combination lasers can also show that it can be expanded to have more sub beams by successive splitting of the input laser beam.

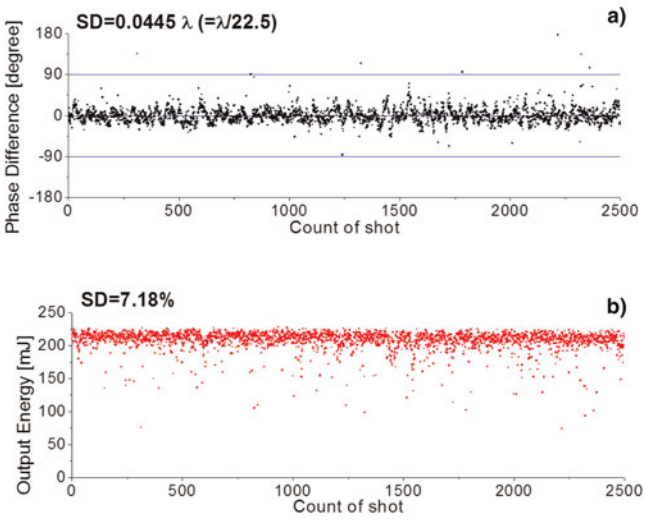

Fig. 14. (Color online) The experimental results of the amplitude dividing two-beam combination with long-term phase stabilization. (**a**) Phase difference during 2500 shots. The standard deviation of the phase difference is $\lambda/22.5$. (**b**) Output energy during 2500 shots. Maximum energy is 228 mJ, and median energy is 211 mJ, Mean energy is 208 mJ.

Also, the phase measurement methods can be applied to more complex beam combination systems.

1.2.2.1. Four Beam Combination Laser Amplifier — Wavefront Dividing Scheme. A four-beam combined laser with the wavefront dividing scheme was successfully demonstrated both with and without amplifiers (Kong *et al.*, 2009*b*; Shin *et al.*, 2010*b*). Figure 15 shows the experimental setup of the four-beam combined laser with the wavefront dividing scheme. A beam expander expands the size of the laser beam by four times and a four-circular aperture shapes the laser beam into the four circular beams. After passing through PBS1, the beam is split spatially by three prisms, P1, P2, and P3. Four beams are named beam 1, beam 2, beam 3, and beam 4. Each sub-beam passes through the amplifiers and the Faraday rotators. At the end of each beam line, the self-phase controlled SBS-PCM reflects the beam. Combined output beam is reflected from the PBS1.

To measure the relative phase differences between sub-beams, an optical wedge reflects a part of beam 1. We will name it beam 0. On the other hand, using HWP2, a small amount of the output beam passes through PBS2. This part of the output beam forms an interference pattern with the expanded beam 0. The relative phases are measured from the interferogram, and the phase controlling electronics controls the PZTs.

Figure 16 shows the output beam profiles and the interferograms. Figure 17 shows the measured phase distributions of each sub-beams without amplifiers, and Figure 18 show the measured phase distributions of each sub-beams with amplifiers. When the amplifiers are not operating, the input energy is 32.2 mJ ± 0.3 mJ and the output energy is 9.9 mJ ± 0.5 mJ. The standard deviation of the phase difference between beam 0 and the four parts of output beam are measured to be $\lambda/86.2$, $\lambda/36.3$, $\lambda/35.8$, and $\lambda/43.4$. When the amplifiers are operating, the input energy is 32.2 mJ ± 0.3 mJ and the output energy is increased to be 169 mJ ±6 mJ. The standard deviation of the phase difference between the beam 0 and the

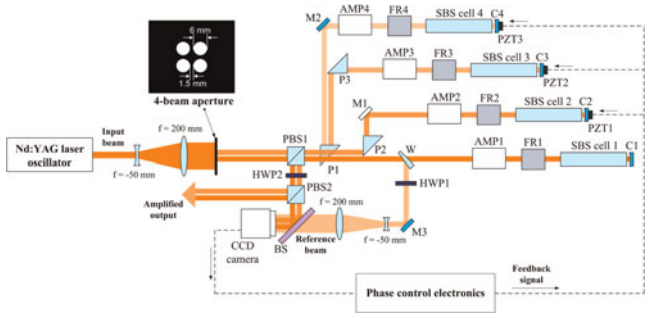

Fig. 15. (Color online) The experimental setup of the wavefront dividing four-beam combined laser. PB1 and PBS2 = polarizing beam splitters; HWP1 and HWP2 = half wave plate; P1, P2, and P3 = 45° prisms; BS = beam splitter; W = wedged window; FR1, FR2, FR3, and FR4 = Faraday rotators; C1, C2, C3, and C4 = concave mirrors; PZT1, PZT2, and PZT3 = piezoelectric transducers.

https://doi.org/10.1017/S0263034611000644 Published online by Cambridge University Press

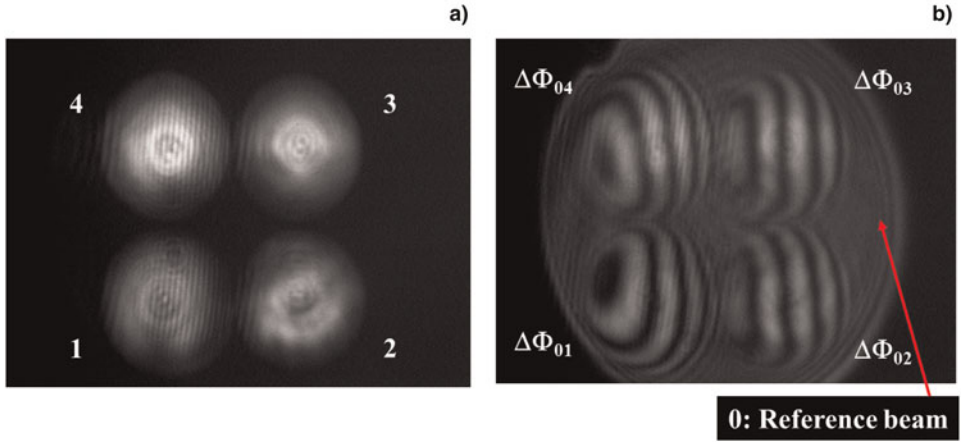

Fig. 16. (Color online) The experimental results of the beam profile and interferograms. (**a**) The output beam profile. (**b**) The interferograms. The large beam profile, noticed by red arrow, is the reference beam.

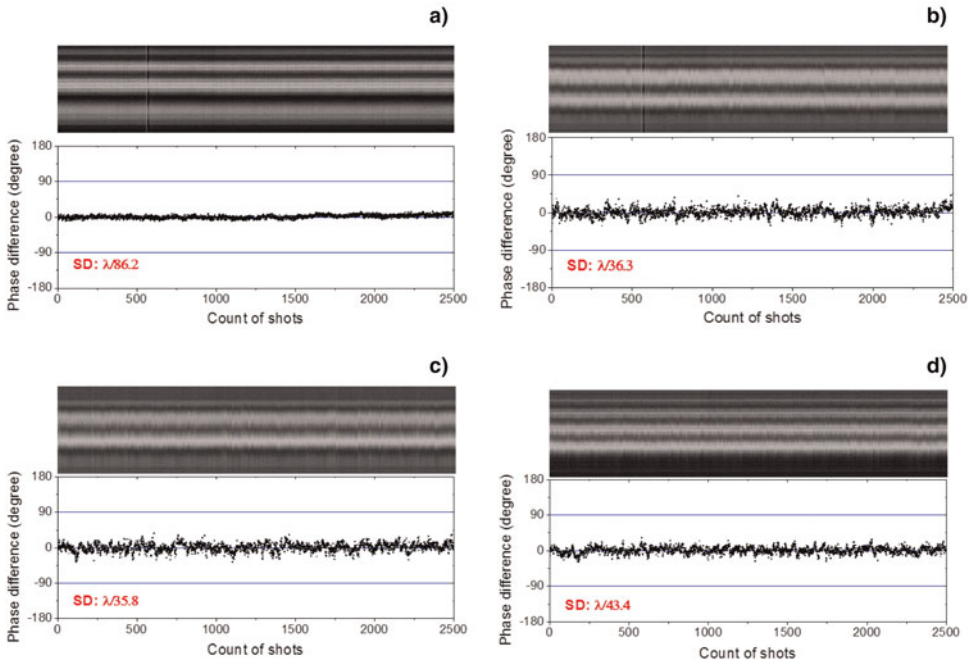

Fig. 17. (Color online) The mosaic intensity profile of the horizontal lines from interference patterns and phase difference of the wavefront dividing four-beam combined laser without amplifiers. (**a**) for ΔΦ01, (**b**) for ΔΦ02, (**c**) for ΔΦ03, and (**d**) for ΔΦ04.

four parts of output beam are determined to be λ/68.8, λ/26.5, λ/28.0, and λ/26.1.

1.2.2.2. Four Beam Combination Laser Amplifier — Amplitude Dividing Scheme. A four-beam combined laser with the amplitude dividing scheme was successfully demonstrated (Kong *et al.*, 2009*a*). Figure 19 shows the experimental setup of the four-beam combined laser with the amplitude dividing scheme. After passing through the PBS, QWP changes the polarization of the laser beam from *p*-polarization to circular polarization. Another PBS splits the beam into two sub-beams. For each beam, the polarization is rotated 45° by PBS. Finally, two more PBS split sub-beams into four sub-beams. At the end of each beam line, the self-phase controlled SBS-PCM reflects the beam. Combined output beam is reflected from the first PBS.

To measure the relative phase differences between sub-beams, beam splitters reflect a part of combining beams. BS1 and BS2 reflect a part of the two beam combined outputs. From the reflected beams of BS1 and BS2, the relative phases between two beams are measured. BS3 reflects a part of the four beam combined output. From the reflected beam of BS3, the relative phase between the two two-beam combined beams is measured. The phase controllers control the PZTs.

Figure 20 shows the measured phase differences between the beams. Figures 20a and 20b shows the measured phase differences between the two beams and Figure 20c shows

https://doi.org/10.1017/S0263034611000644 Published online by Cambridge University Press

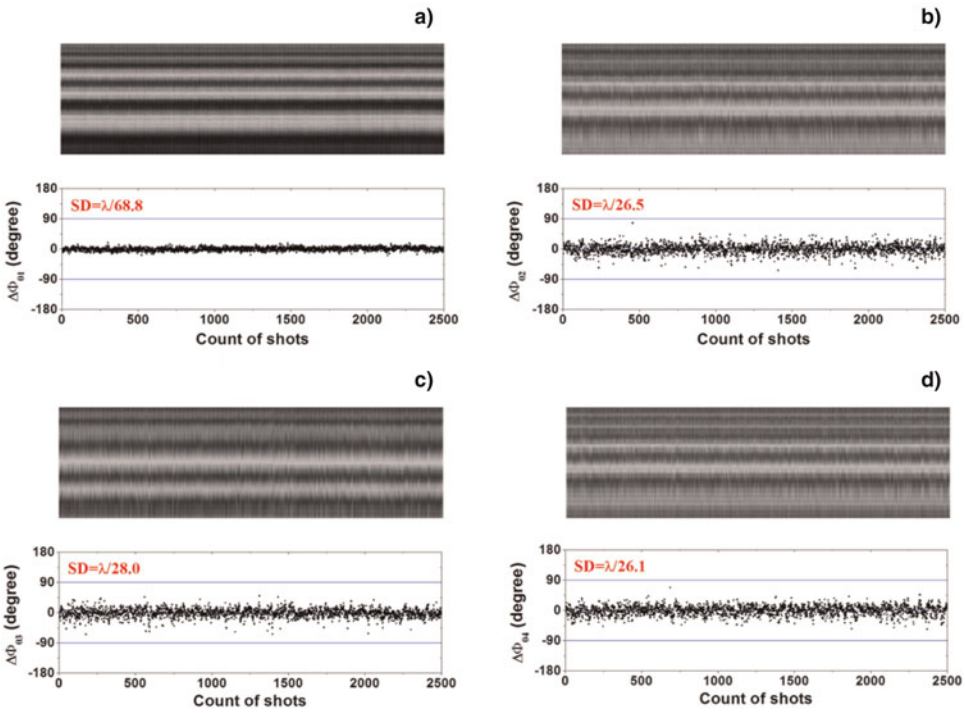

Fig. 18. (Color online) The mosaic intensity profile of the horizontal lines from interference patterns and phase difference of the wavefront dividing Four-beam combined laser with amplifiers. (**a**) for ΔΦ01, (**b**) for ΔΦ02, (**c**) for ΔΦ03, and (**d**) for ΔΦ04.

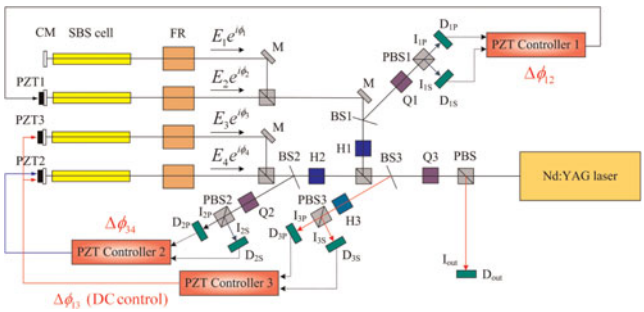

Fig. 19. (Color online) The experimental setup of the amplitude dividing four-beam combined laser. PB1 = polarized beam splitter; HWP1 and HWP2 = half wave plate; QWP = quarter wave plate; BS1, BS2, and BS3 = beam splitters; CM = concave mirror; PZT1, PZT2, and PZT3 = piezoelectric transducers.

the measured phase differences between two-beam combined beams. The standard deviations of the phase differences are λ/34.3, λ/44.1, and λ/37.6. The fluctuation of the output energy is 6.16%.

1.2.3. Recent Progresses on the Prepulse Technique

It is known that the front part of reflected pulse from SBS-PCM is consumed to generate the moving Bragg grating (Kong *et al.*, 2005*a*; 2005*c*). To preserve the waveform of the pulse, the prepulse technique is suggested and demonstrated (Kong *et al.*, 2005*a*; Beak *et al.*, 2008; Yoon *et al.*, 2009). In the prepulse technique, an input pulse is split into the prepulse and the main pulse. The prepulse has energy of about the threshold energy of the SBS-PCM. The prepulse arrives at the SBS-PCM earlier and ignites a moving Bragg grating. The front part of the main pulse is highly reflected by the preformed moving grating and the waveform of the reflected pulse is preserved.

1.2.3.1. Relationship Between the Optimum Prepulse Energy and the Delay Time for the Waveform Preservation. Figure 21 shows the experimental setup for measuring the waveforms of SBS waves with varying prepulse energy levels and delay time. An input pulse has a pulse width of 7–8 ns and a repetition rate of 10 Hz. After passing through an optical isolator, the input beam passes through HP2 and is divided by PBS2 into two sub-beams — the main pulse and the prepulse. The main pulse energy is fixed at 10 mJ. The main pulse is reflected by PBS4 and passes the delay line twice. A quarter wave plate (QP) in the delay line rotates the polarization of the main pulse by 90°, so the main pulse passes through the PBS4. HP3 and PBS3 play the role of adjusting the prepulse energy. HP4 and HP5 and the Faraday rotators (FR1 and FR2) rotate the polarization by −45° and 45°, respectively, and thus the main pulse with *p*-polarization and the prepulse with *s*-polarization are combined at PBS5 with some time delay. Finally, both pulses enter the SBS-PCM. The focal length of the focusing lens is 15 cm. The reflected prepulse retraces the path of the incident prepulse beam and is dumped out at PBS3 because its polarization is changed by HP4 and FR1. By the same reason, the reflected main pulse is reflected by PBS4 and photodiode (PD)

https://doi.org/10.1017/S0263034611000644 Published online by Cambridge University Press

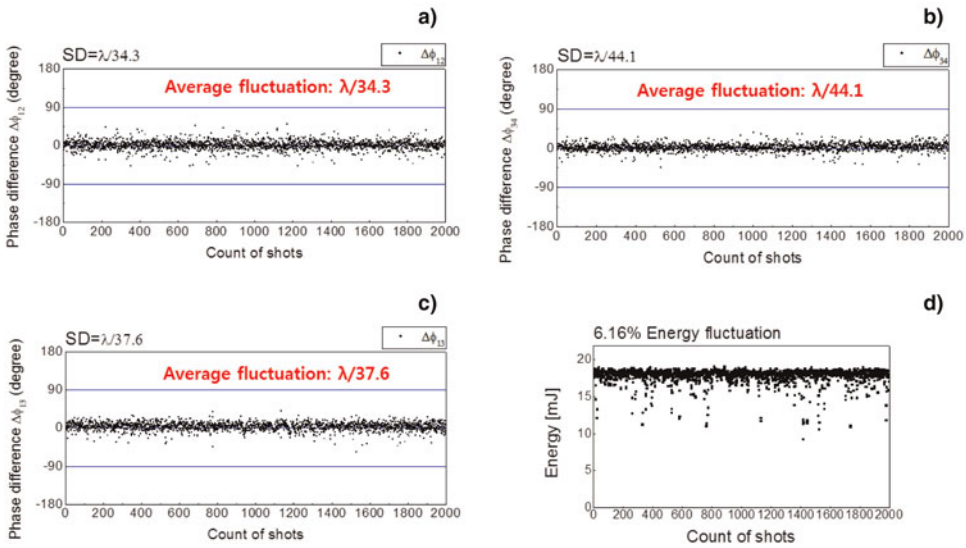

Fig. 20. (Color online) The phase difference of the amplitude dividing four-beam combined laser without amplifiers for 2500 shots and energy distribution for 2500 shots. (**a**) for ΔΦ12, (**b**) for ΔΦ34, (**c**) for ΔΦ13, and (**d**) Energy distribution for 2500 shots.

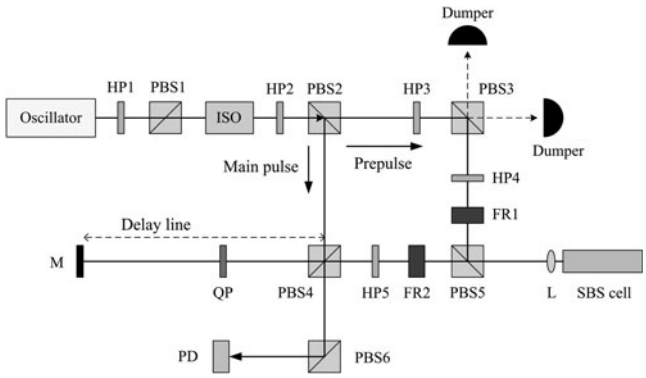

Fig. 21. Experimental setup for the prepulse injection method. HPs = half-wave plates; PBSs = polarizing beam splitters; ISO = optical isolator; FRs = Faraday rotators; QP = quarter-wave plate; M = mirror; L = focusing lens; PD = photodiode.

measures the waveform of the main pulse. The signal from the PD was measured by an oscilloscope operating with a bandwidth of 500 MHz and a sampling rate of 500 Msamples/s.

Figure 22 shows the temporal waveforms measured at a delay time of 15 ns. As the prepulse energy increases, the waveform of the reflected pulse becomes more similar to that of the input pulse. When the prepulse energy is more than 2 mJ, the pulse shape is perfectly preserved. Figure 23 shows the simulation and the experimental results of the minimum prepulse energies required to preserve the waveform over the prepulse delay time. The simulation result is obtained by calculating the energy stored in the acoustic grating at the time of the main pulse arrival. From the experimental result, we can conclude that the optimum prepulse delay time is 15 ns and the required prepulse energy at this delay is 2 mJ per pulse.

1.3. Conclusion

In this work, we introduced the recent progress of the coherent beam combination laser using the Self-phase-controlled SBS-PCMs. We have constructed two-beam coherent combination laser and four-beam coherent combination laser both the amplitude dividing scheme and the wavefront dividing scheme. Furthermore, we have preserved the waveform of the SBS wave pulses by pre-pulse technique. The research on the key techniques of the coherent beam combination laser has been completed. From these techniques, we can make a 16 J at 10 kHz laser by 4×4 beam combination of 1 J at 10 kHz lasers for the laser machining by hologram, extreme ultraviolet source for extreme ultraviolet lithography, and so on, and a 2.5 kJ at 10 Hz laser by 5×5 beam combination of 100 J at 10 Hz lasers for the laser machining by hologram, laser peening, the neutron/proton generator, and the laser fusion. Also the key techniques of SBS-PCMs are related with the self-navigation technique for the laser fusion driver, so these techniques have various applications, and the beam combination laser using the self-phase controlled SBS-PCM is a key of the future dream laser generating an unlimited output energy/power with high repetition rate operation.

2. TEMPORAL COMPRESSION BY STIMULATED BRILLOUIN SCATTERING WITH HEAVY FLUOROCARBON LIQUID AT 532-NM WAVELENGTH PUMPING (H. Yoshida, K. Tsubakimoto, H. Fujita, N. Miyanaga, and M. Nakatsuka)

2.1. Introduction

The stimulated Brillouin scattering (SBS) in various solids, liquids, and gases is a very powerful tool to build the

https://doi.org/10.1017/S0263034611000644 Published online by Cambridge University Press

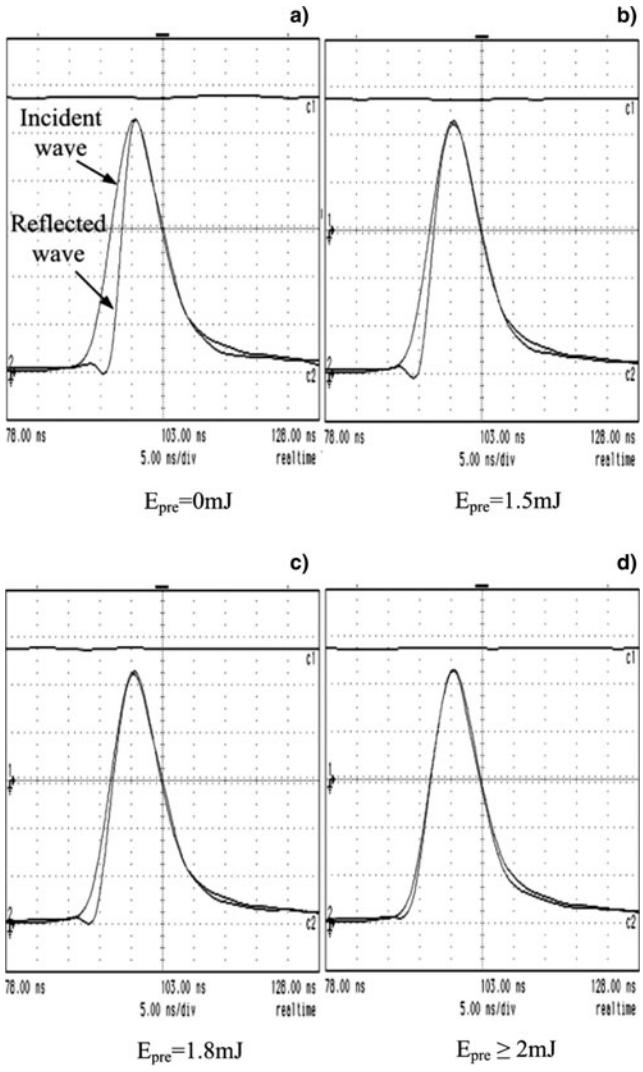

Fig. 22. Reflected waveforms when $td = 15$ ns: (**a**) $E_{pre} = 0$ mJ, (**b**) $E_{pre} = 1.5$ mJ, (**c**) $E_{pre} = 1.8$ mJ, and (**d**) $E_{pre} >> 2$ mJ.

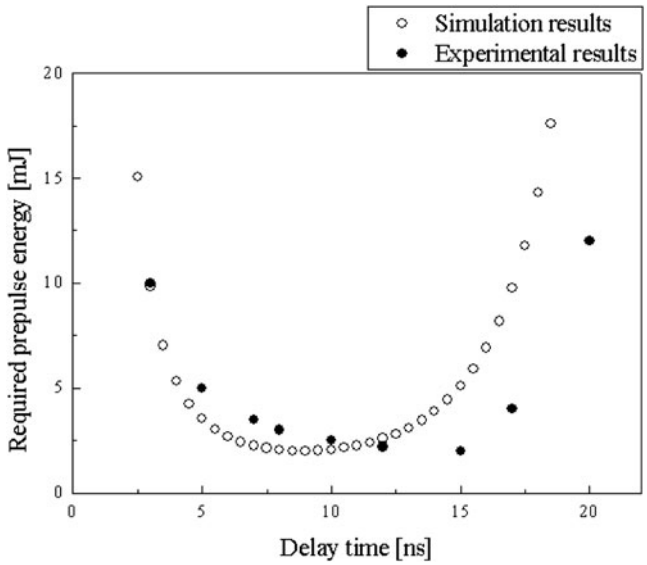

Fig. 23. Required prepulse energy versus the delay time [the experimental results (filled dots) and the simulation results (blank dots)].

phase conjugation mirror (PCM) in high-power laser systems (Rockwell, 1988; Dane *et al.*, 1994*a*; Yoshida *et al.*, 1997, 1999, 2003, 2004; Kong *et al.*, 2005*b*, 2005*c*, 2006, 2007*a*; Meister *et al.*, 2007; Kappe *et al.*, 2007; Yasuhara *et al.*, 2008). A PCM based on the SBS process can be successfully used to compensate thermally induced phase distortion in high power laser systems. A PCM is very efficient for enhancing the laser beam quality especially in designing a double pass laser amplifier systems. Also, the SBS process can be applied for the high-efficiency pulse compression of an energetic laser pulse.

The SBS compression of laser pulse has been investigated theoretically and experimentally for various laser wavelengths and active SBS media (Dane *et al.*, 1994*a*; Schiemann *et al.*, 1997; Kmetik *et al.*, 1998). The SBS compressor provides enhancement of peak intensity of pulses while maintaining its high energy, and make available laser pulse duration of a few 100 ps. It is difficult to generate mode-locking pulses without damage at high peak power. On the other hand, this method of short-pulse generation is very simple and can be used to achieve high brightness. The heavy fluorocarbon satisfies the demands for SBS medium in the view of excellent optical quality, low absorption in wide spectral region from ultraviolet to infrared, a high threshold of optical breakdown, good thermodynamic properties, and desirable chemical stability. We previously reported that a 8 ns Nd:YAG laser pulse was temporally compressed to a SBS phase conjugation pulse of 600 ps using a 1.7-m-long cell FC-75 liquid (Mitra *et al.*, 2006). A 13-ns Nd:YAG laser pulse was temporally compressed to about 160-ps phase-conjugated pulse in heavy fluorocarbon FC-40 liquid at a 1064 nm wavelength (Yoshida *et al.*, 2010). We are developing a high-average-power short pulse laser system based on optical parametric chirped pulse amplifier (OPCPA) technique. A few hundred ps 532-nm pulse laser will be used to pump the OPCPA system.

For the first time to our knowledge, we demonstrated the efficient compression of 10 ns pulse duration to 160 ps or less at second harmonics of an Nd:YAG laser. The compressed pulse brightness is about 56-fold higher than that of the incident pulse. The heavy fluorocarbon liquid can also be used as phase conjugators for high-average-power.

2.2. Experimental Results

The experimental layout of temporal SBS compression is shown in Figure 24. The laser used was a linearly polarized Q-switched Nd:YAG oscillator at single-frequency and TEM_{00} mode operation. The amplified output was 10 ns pulse of approximately 500 mJ at a 10 Hz repetition rate. The beam quality was 1.5 times diffraction-limited. The 1064-nm output beam is externally doubled to 532 nm

https://doi.org/10.1017/S0263034611000644 Published online by Cambridge University Press

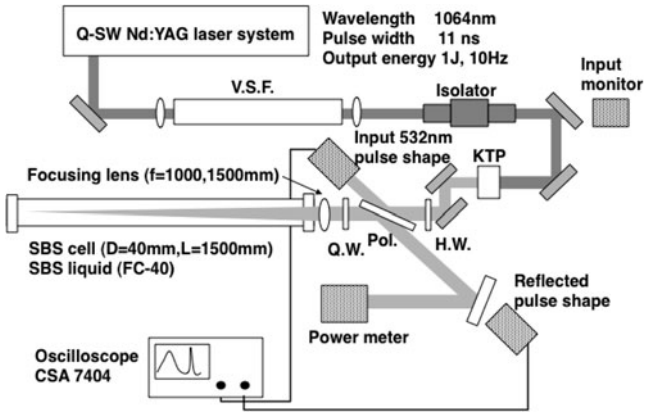

Fig. 24. The experimental layout of temporal SBS compression.

with a $KTiOPO_4$ (KTP) crystal. KTP was chosen as the nonlinear crystal because of its high effective nonlinear coefficient. The laser light was focused into a SBS cell through a variable attenuator using a combination of a half-wave plate and a thin-film polarizer. The reflected laser beam was separated using a dielectric thin-film polarizer and a quarter-wave plate.

We have fabricated a long cell for liquid phase conjugation mirror of length 1.5 m and diameter 4 cm. Windows of the cell had antireflection coating at 532 nm. These cells were filled up with FC-40 liquid. Before filling we filter the liquid by using Millipore filters of pore size 0.020 μm. This filtering was important to increase the optical breakdown threshold. The circularly polarized laser beam was focused inside the cell by a lens with focal length of 500 or 1000 mm. The absorption coefficient of FC-40 liquid at 532 nm wavelength was about 1×10^{-5} cm^{-1}. Experiments on SBS compression were performed using a combined generator-amplifier system. The circularly polarized laser beam was transmitted through the 1.5-m long SBS cell, and was focused into the other 1.5-m long generator using a lens of focal length 750 mm. The pulse shapes of the pump and reflected beams were monitored using a Hamamatsu R1328U-51 biplanar phototube (rise time; 55 ps) and a Tektronix CSA7404 signal analyzer (analog bandwidth; 4 GHz and rise time; 100 ps). The reflected energy was directly measured with a power meter. The SBS backward reflectivity from the FC liquid was also compared with the total reflection from a conventional thin-film mirror ($R = 99.5\%$).

The SBS gain coefficient was independent of the pumping wavelength in the transparent medium. The FC-40 was reported to be 2 cm/GW at 1064 nm. The phonon lifetime τ_B and Brillouin bandwidth $\Delta\nu_B$ depend inversely on the pump wavelength assuming that $\tau_B \propto \lambda_p^{-2}$ and $\Delta\nu_B = 1/2\pi\,\tau_B$. The phonon lifetime τ_B is proportional to λ_p^{-2}, so that τ_B at 1064 nm is one-fourth that at 532 nm. FC-40 liquid with a fast SBS relaxation time was selected from a lot of heavy fluorocarbon. The τ_B value at 1064 and 532 nm for FC-40 were approximately 250 and 70 ps, respectively.

Because SBS begins from a leading edge of the propagating pulse, an optimum reflection is expected for a spatial length of the pulse, $(c/2n)\,\tau_\pi$, where τ_π is the pulse width (full width at half maximum (FWHM)) and n is the refractive index of a FC liquid. For a 10 ns pulse and a refractive index $n = 1.28$, the interaction length L_{in} was taken as 117 cm. The optical path length of the Brillouin cell, $L = 150$ cm was chosen over 117 cm to satisfy the condition $L > L_{in}$.

The SBS compression reflectivity for several focal lengths in a FC-40 liquid is shown in Figure 25. A maximum intrinsic SBS reflectivity of over 90% was obtained at incident energy of over 100 mJ. The SBS threshold of about 5 mJ was observed. On the other hand, the Brillouin generator-amplifier system that consist of $L = 1500$ mm amplifier and $f = 750$ mm generator was obtained a maximum SBS reflectivity of 35% at an incident energy of about 200 mJ. This system controls the energy entering the Brillouin generator to prevent optical breakdown. A SBS reflectivity using $f =$ 1000 mm lens was slightly lower than that using $f =$ 500 mm lens. It confirms that the SBS process can be effective if the coherence length of the optical pulse is equal to or longer than the length of the Stokes field region. In practice, it denotes that the coherence length of the SBS pump pulse should be longer than the confocal length of the focused SBS pump beam divided by a refractive index. The bandwidth of the laser oscillator used here is 250 MHz and so that the coherence length L_c is about 120 cm. The interaction length L in the SBS material using $f = 500$ nm or $=$ 1000 mm was 64 cm and 128 cm, respectively. In the case of the 500-mm-focal-length lens, a condition $L_c > L$ was satisfied; however, in the case of the 1000-mm-focal-length lens, this condition was marginal.

The SBS compressed-pulse duration using several different focal lengths is shown in Figure 26. In the case of the

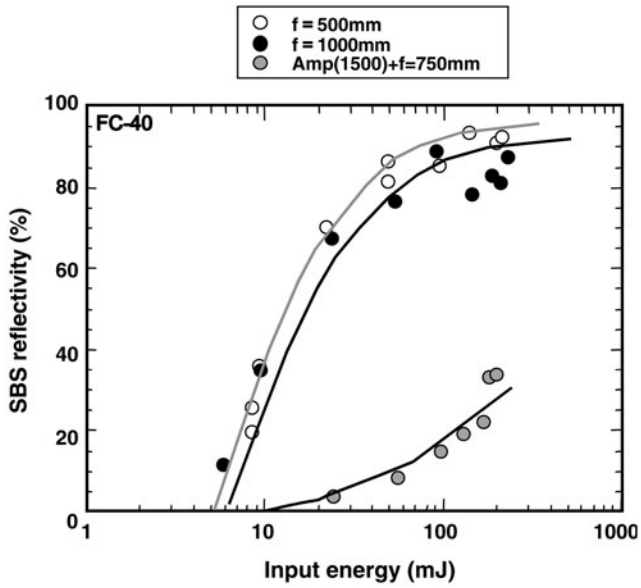

Fig. 25. SBS reflectivity measured at 532 nm pumping.

https://doi.org/10.1017/S0263034611000644 Published online by Cambridge University Press

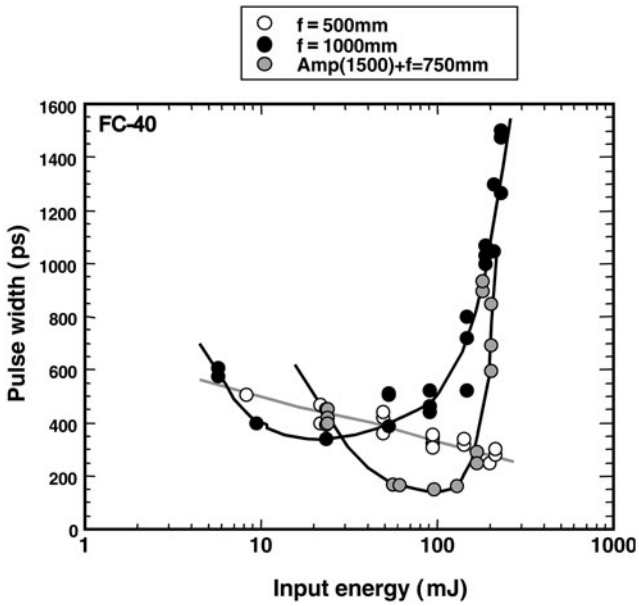

Fig. 26. The compressed pulse duration measured at 532 nm pumping.

500-mm focal length, the compressed pulse width was 250 ps at incident energy of 200 mJ. The maximum compression ratio is about 40-fold higher than that of the incident pulse of 10 ns. In the case of the 1000-mm focal length, the minimum pulse width of 350 ps was obtained at 30 mJ input energy, but the compressed pulse width slowly increased. The pulse width at incident energy of 200 mJ was increases in length of 1.5 ns. The Stokes pulse duration depends on the pumping energy, and the compressed minimum pulse width of the Brillouin generator-amplifier system at over 100 mJ reached 160 ps or less. However, the Stokes pulse showed substantially wider pulses as the incident energy increased to 200 mJ. This results from the leading edge of the amplifier Stocks incident pulse interacting with the low energy leading edge of the Gaussian pumping pulse.

The typical shapes of compressed pulses are shown in Figure 27. A slow falling time of the compressed pulse was observed owing to the reduced intensity in the peripheral part of the spatial profile. The pump beam was highly compressed at the center of the beam, while the compression effects were much less at the wings. The pulse shape of the reflected beam was a mixed pulse that combines a fast rising time at the center and a slow falling time at the wing of the pulse. The SBS compressed-pulse duration using a focal length of 500 mm observed the dumping waveform for falling edge because the interaction length of 63 cm is shorter than the necessary length of $L = 117$ cm. In a focal length of 1000 mm and two cell method, the compressed pulse shape consist of a steep leading edge and a sharp falling edge because the interaction length of the Brillouin cell was about 117 cm. The experimental observations of phase jumps and amplitude fluctuations in SBS were reported (Afshaavahid *et al.*, 1998) No special pulse compression geometric conditions such as short focal length have an affect on the length of the Stokes-pump interaction. The noise of SBS process results in the fluctuation in the Stokes pulse due to energy interchange between Stokes and pump pulses. The damping time corresponds to the SBS phonon lifetime.

The fluctuation of the pulse width greatly depends on the focusing condition of the SBS generator. Figure 28 shows the time fluctuation of input pulses and SBS compression pulses. The jitter timing of SBS compression pulses was about 500 ps and similar to that of the incident Q switched. The focusing condition depends on the input beam quality of shot to shot and the environmental condition of SBS amplifier. The focusing ability of SBS generator decreases with the vibration in the enclosed liquid and the convection flow by an environmental temperature. The SBS phase-conjugation ability corrected these perturbations, but it is necessary the SBS cell have good insulation for focusing condition of the SBS generator.

In this experiment on pulse compression in FC-40, there is a possibility that the process of stimulated Raman scattering (SRS) competes with SBS. At maximum input energy SRS is weak and does not influence SBS. The nonlinear effects, such as self-phase modulation and self-focusing, were not observed because the nonlinear refractive index (1×10^{-7} cm^{2}GW^{-1}) of Fluorinert liquid is too low and the beam quality of SBS compression pulse is similar to that of the incident pulse. It will be necessary to measure a nonlinear effect in the future.

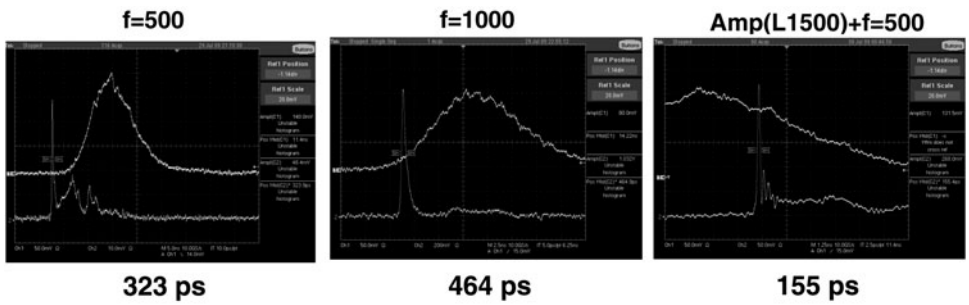

Fig. 27. The oscilloscope traces of the typical incident and reflected waveforms at several focal length.

https://doi.org/10.1017/S0263034611000644 Published online by Cambridge University Press

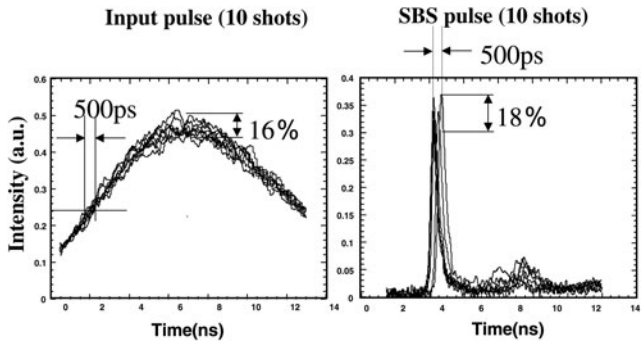

Fig. 28. The time fluctuation of input pulses and SBS compression pulses.

2.3. Conclusion

In summary, a heavy fluorocarbon liquid, such as FC-75 and FC-40, had been successfully demonstrated as a SBS compressor at a 532-nm wavelength. A 10 ns Nd:YAG laser pulse is temporally compressed to a 160 ps or less phase conjugated pulse and maximum SBS reflectivity of about 90% without any damage was observed. The brightness of the compressed pulse was about 56-fold higher than that of the incident pulse. Damage-free operation of a heavy fluorocarbon liquid as a better phase conjugate material could lead to the construction of laser-diode pumped, all-solid-state laser system. The generation of sub-ns pulse is useful for precise material processing and extreme ultraviolet lithography.

3. HIGH-INTENSITY LASER PULSE COMPRESSION AND AMPLIFICATION BY STIMULATED BRILLOUIN SCATTERING (Y. Wang, Z. Lu, Z. Zheng, and Y. Zhang)

3.1. Introduction

High-peak-power high energy pulse lasers of hundreds picoseconds play an important role in the fields of inertial confinement fusion (ICF) (Kong *et al.*, 2005, 2007*a*), diagnostics of plasma by means of Thompson scattering (Mao *et al.*, 2001) and produce of X-ray radiation for lithography (Endo, 2004). Especially in the field of ICF, shock ignition is a new concept for direct-drive laser ICF that was proposed by Betti *et al.* (2007). Compared with the standard direct drive central ignition and fast ignition, shock ignition presents overwhelming advantages (McCrory *et al.*, 2008). It does not require any complex cone-in-a-shell targets or high power chirp pulse amplifier lasers. However, it is a key difficulty to obtain the high-energy and high-power laser pulse with a hundred picoseconds width in the ICF laser driver to achieve shock ignition. Stimulated Brillouin scattering (SBS) is a particularly useful tool to compress a long pulse because of its power compatibility (Wang *et al.*, 2010), high energy reflectivity and high compression ratio (Yoshida *et al.*, 2009). Applied SBS pulse compressor and amplifiers to the high-energy laser system is an efficient way to obtain high intensity picosecond pulses. In this work, we have demonstrated high-energy laser pulse compression and amplification by SBS using a two-cell scheme. A higher energy experiment will be demonstrated in the one-hundred-joule Nd: phosphate glass laser system (Ostermeyer *et al.*, 2008) in the future.

3.2. Experimental Setup and Design

The experimental setup is shown in Figure 29. A short Stokes seed pulse is obtained by a two-cell SBS generator and then amplified in the Brillouin amplifier.

The laser used in the experiments was a linearly polarized single frequency Q-switched Nd:YAG oscillator (PRII9010, Continuum Inc.) with 8 ns pulse duration and 6 mm beam diameter. The pulse was split by the polarized plate P2. One pulse was seeded into the two-cell generator to produce the Stokes seed pulse. And the other pulse was used as the pump pulse. A compact SBS generator-amplifier setup was used as the picoseconds Stokes generator. In the generator, Lens 1 was a long focal lens (1000–1500 mm) and Lens 2 was a short focal lens (300–500 mm). The length of generating cell 1 and generating cell 2 were 800 mm and 1000 mm, respectively. In the amplifier, the pump pulse propagated through the amplifying cell before the Stokes seed was reflected by M3 and then encountered with the Stokes seed in the amplifying cell. The amplified Stokes pulse was exported by the polarized plate P3. To achieve optimal amplifying result, the encounter time was changed by moving the high reflected mirror M3. The pulse shapes were monitored using a Tektronix DPO7254 oscilloscope (bandwidth 2.5 GHz) and a fiber coupled ultrahigh speed photo detector (18.5 ps, New Focus).

3.3. Experimental Results and Discussion

FC-72 was chosen as the SBS medium in the experiment. The length of the cells and the focal length of Lens 1 were fixed. And the focal length of Lens 2 was set as 300 mm, 600 mm, and 750 mm, respectively. Figure 30 shows the compressed pulse duration changing as the input intensity increasing.

SBS is a nonlinear process and so the compressed pulse duration is not changing linearly as increasing the input intensity. For different focal length of Lens 2, the stability of

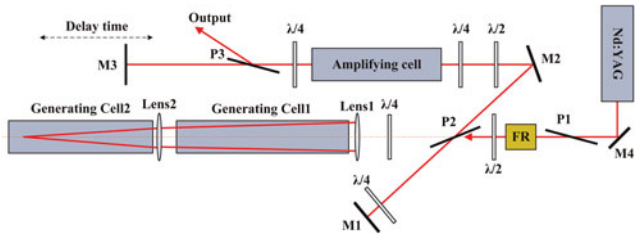

Fig. 29. (Color online) Optical layout of SBS temporal-pulse compressor and amplifier.

https://doi.org/10.1017/S0263034611000644 Published online by Cambridge University Press

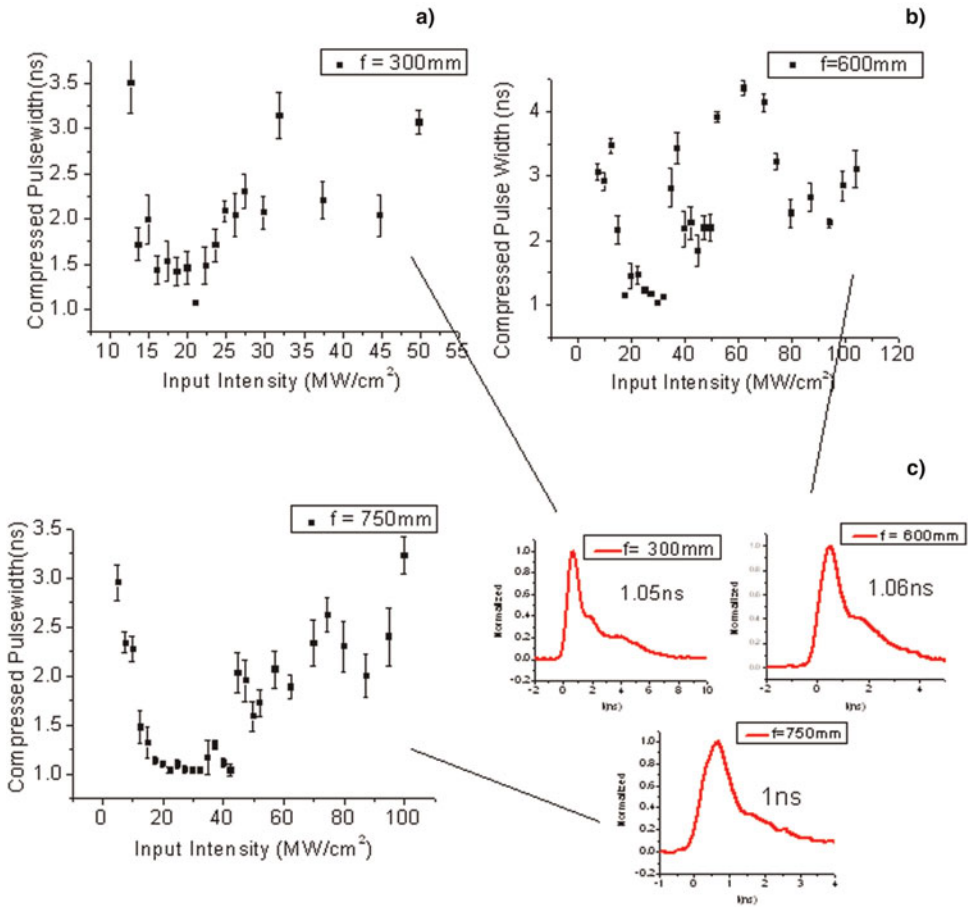

Fig. 30. (Color online) The results of compact SBS generator-amplifier pulse compression with different focal length of Lens 2: (**a**) $f2 = 300$ mm, (**b**) $f2 = 600$ mm, (**c**) $f2 = 750$ mm.

compressed pulse duration changes obviously. With shortening of the focal length of Lens 2, the compressed pulse width is becoming increasingly unstable. When the focal length of Lens 2 is 750 mm, the compressed pulse duration is stable at about 1ns with the input intensity 20–40 MW/cm^2. When the focal length of Lens 2 is 600 mm, the compressed pulse duration is stable with the input intensity 20–30 MW/cm^2. When the focal length of Lens 2 shortens to 300 mm, the compressed pulse duration is not stable at any input intensity in the experiment.

The energy reflectivity with different focal length of Lens 2 is shown in Figure 31. It is effective to improve the energy reflectivity by lengthening the focal length of Lens 2. The optimal pulse width of compressed pulse and the highest energy reflectivity occurs at different pump intensity. The highest energy reflectivity is nearly 80% in the experiment.

It is very difficult to achieve sub-nanosecond pulse by changing focal length of Lens 2 with FC-72 because the phonon lifetime of FC-72 is 1.2 ns. We choose several

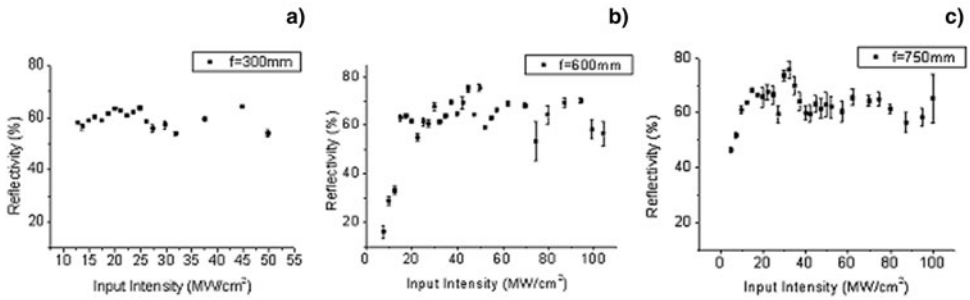

Fig. 31. The energy reflectivity of different focal length of Lens 2 in compact SBS generator-amplifier scheme: (**a**) $f2 = 300$ mm, (**b**) $f2 = 600$ mm, (**c**) $f2 = 750$ mm.

https://doi.org/10.1017/S0263034611000644 Published online by Cambridge University Press

media that have a shorter phonon time as the SBS medium in the generator cell 2. They are HS260 (phonon lifetime: 0.1 ns), FC-43 (phonon lifetime: 0.2 ns) and DET (phonon lifetime: 0.7 ns). The result was shown in Figure 32. In the experiment, the focal length of Lens 2 was fixed at 300 mm. The optimal compressed pulse duration is 760 ps with DET, 490 ps with FC-43 and 312 ps with HS260.

The energy reflectivity of our experiment is shown in Figure 33. The energy reflectivity is unstable and is not high with DET and HS260. The energy reflectivity with FC-43 is higher than the other two media and can achieve 80%. The reason is that the gain coefficient of FC-43 is higher and the Stokes shift of FC-43 is close to the Stokes shift of FC-42. In the generating cell 1, a Stokes seed with short duration is excitated by a shorter phonon lifetime medium and in the generating cell 2 the Stokes seed is amplified efficiently by another higher gain medium.

In a word, to achieve a Stokes pulse with 200 ps pulse duration, we should choose the appropriate media of the cell1 and cell 2. Meanwhile, a reasonable compressor structure is important so that the compressor will operate in an optimal condition.

The amplification of the Stokes seed with hundreds picoseconds pulse duration was investigated in the experiment. As a seed, the duration of the Stokes pulse is stabilized at 0.5 ns. FC-72 is selected as the amplifying medium. The length of the amplification cell is 800 mm and 1500 mm. The energy amplification ratio η is defined as

$$\eta = \frac{E_{amplified} - E_{seed}}{E_{pump}}$$

where $E_{amplified}$ is the energy of amplified Stokes seed in the amplifying cell, E_{seed} is the energy of Stokes that output from the generating cell and E_{pump} is the pump energy.

The result of the experiment is shown in Figure 34. The energy amplification ratio is decreasing with the pump intensity increasing. The reason is that the duration of the pump pulse is 8 ns much longer than the Stokes seed with duration of 0.5 ns and the encounter length of the two pulses is not optimal in the experiment. Meanwhile, it was observed that the pulse duration of the amplified Stokes seed was broadened significantly. The results indicated that the pump pulse was not depleted completely by the Stokes seed. In the future the ratio of

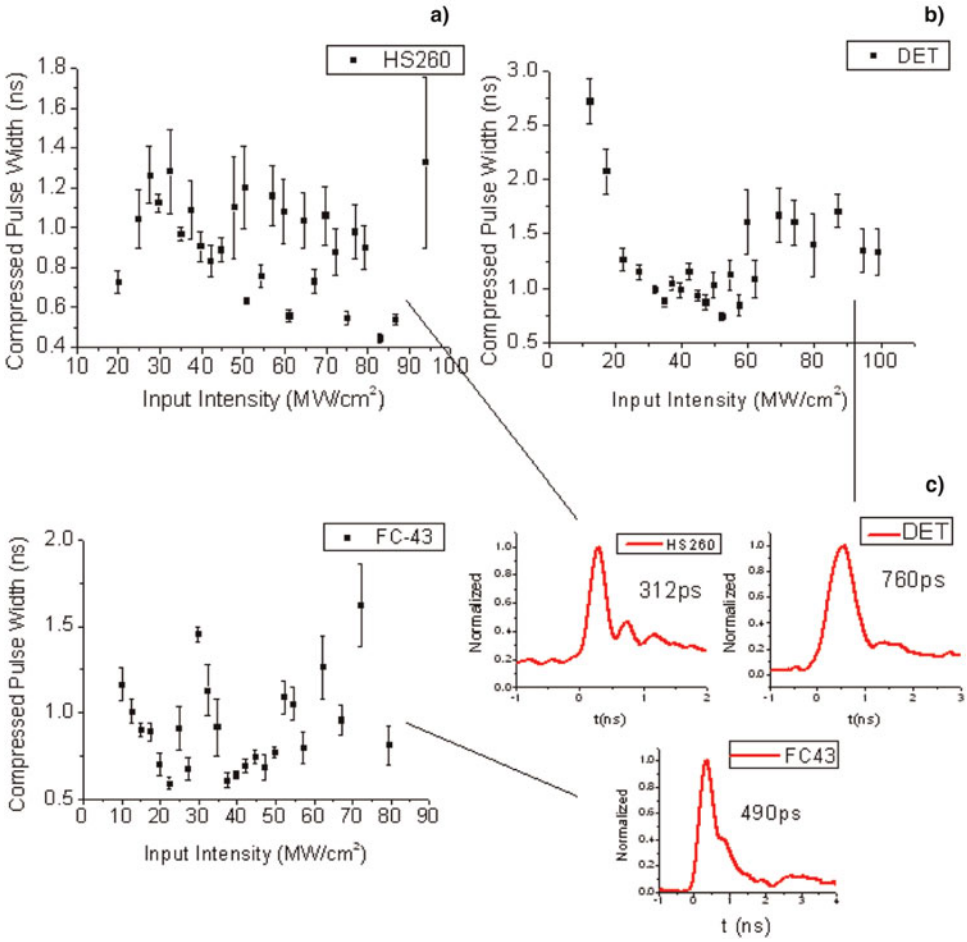

Fig. 32. (Color online) The pulse compression result with different medium: (**a**) HS260, (**b**) DET, (**c**) FC-43.

https://doi.org/10.1017/S0263034611000644 Published online by Cambridge University Press

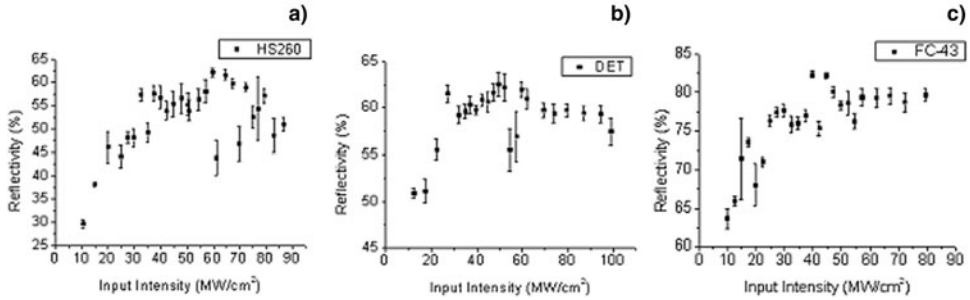

Fig. 33. The energy reflectivity of the compact SBS generator-amplifier with different medium: (**a**) HS260, (**b**) DET, (**c**) FC-43.

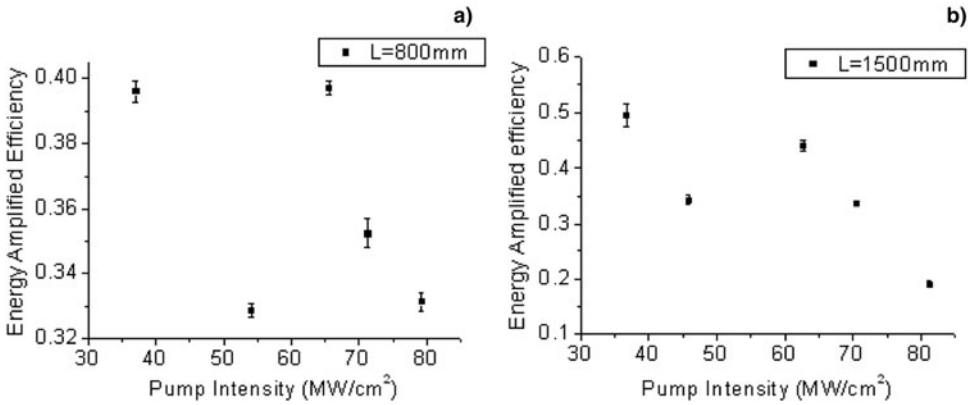

Fig. 34. The energy amplification ratio with different length of the amplification cell: (**a**) L = 800 mm, (**b**) L = 1500 mm.

the pump duration and the Stokes duration and the amplification scheme should be optimized to enhance the conversion efficiency.

3.4. Conclusion

The influence of input intensity on SBS compression and reflectivity is significant. By choosing the proper configuration and input intensity, the stable and efficient reflectivity with a high compress factor can be obtained. Using a compact SBS generator-amplifier scheme and choosing the medium with low phonon lifetime as generator medium and high gain coefficient medium as amplifier medium, the compressed pulse duration of 312 ps is obtained. It is indicated by the amplifying experiment that it is a way to obtain the pulse of hundreds picoseconds with high energy.

ACKNOWLEDGMENT

This work was supported by the National Natural Science Foundation of China (Grant No. 61008005), the China Postdoctoral Science Foundation (Grant No. 20090450966), Special Foundation (Grant No. 201003428), the Heilongjiang Postdoctoral Science Foundation (Grant No. LBH-Z09128), Natural Scientific Research Innovation Foundation in Harbin Institute of Technology (Grant No. HIT. NSRIF. 2009010), and the Fundamental Research Funds for the Central Universities (Grant No. HIT. KLOF. 2010037).

4. LATEST DEVELOPMENT IN THE SBS PCM BASED SELF-NAVIGATION OF LASER DRIVERS ON INJECTED PELLETS (M. Kalal, O. Slezak, and H.J. Kong)

One of the most difficult challenges to deal with in the direct drive inertial fusion energy (IFE) integrated approach is connected with the need of simultaneous irradiation of injected pellets with thermonuclear fuel inside the reactor chamber by many dozens (or even hundreds) of powerful laser beams. Sophisticated tracking of injected pellets' trajectories is necessary for prediction of the place most suitable for interaction with the driver beams in order to achieve necessary irradiation symmetry and subsequent fuel compression. For the direct drive scheme, the following set of parameters is being currently considered: pellets about 4 mm in diameter should be delivered into the virtual sphere of about 5 mm in diameter and located around the center of the reactor chamber about 10 m in diameter. Combined precision of tracking and aiming should be about 20 μm. Navigation technologies developed so far (despite their gradual progress) are still outside the required margin even in the case of fully evacuated reactor chambers — as some time consuming adjustment of

https://doi.org/10.1017/S0263034611000644 Published online by Cambridge University Press

heavy final optics for every shot and every laser beam is always necessary. This fact is also partially responsible for a rather tight margin (±500 μm) on the pellets successful delivery into the above mentioned virtual sphere.

In reality, there are even more serious obstacles further complicating this direct drive IFE scheme — even putting its practical feasibility in doubts. Among the most serious ones is the insufficient predictability of the injected pellets' trajectories resulting from their expected interaction with remnants of previous fusion explosions due to the considered 5–10 Hz repetition rate. This might be one of the reasons why the indirect drive scheme seems to be currently considered as a more serious IFE candidate — having the corresponding hohlraum targets by three orders of magnitude heavier compared to their direct drive counterparts, thus allowing for much more reliable prediction of their trajectories. In order to deal with these direct drives laser navigation difficulties, a new approach was recently proposed employing the stimulated Brillouin scattering-phase conjugate mirror (SBS-PCM) technique (Zel'dovich *et al.*, 1972; Brignon *et al.*, 2003). In the first presentation of this approach (Brington & Huignard, 2003), it was predicted that a fully automatic self-navigation of every individual laser beam on injected pellets with no need for any final optics adjustment could be developed. As a byproduct, a higher number of less energetic (thus easier to design) lasers could be employed. This idea was undergoing a gradual improvement in its theoretical design (Kalal *et al.*, 2007*b*, 2008*b*; Ostermeyer *et al.*, 2008*a*) and subsequently it started to be tested also experimentally — proving the principle (Kalal *et al.*, 2008, 2010*a*).

The current design of the SBS-PCM approach to the direct drive IFE is outlined in Figure 35 where one particular laser channel is displayed during the three distinct stages of its operation.

The SBS-PCM based IFE approach has one crucial advantage over the classical one: even if the pellets will inevitably reach for every injection slightly different (and difficult to predict with the accuracy required) position within the prescribed area (if missed the shot will be declared as unsuccessful), their subsequent *displacement* from the position in which they will be illuminated into the position in which they will be irradiated would always be the same (provided, that the injection speed will not vary substantially from shot to shot). For the pellet injection speeds, about 100 m/s (in practice they might be several times higher) and 1 μs delay times corresponding to 300 m distance traveled by each laser beam outside the reactor chamber (to reserve enough room for a large number of drivers), typical displacements between illumination and irradiation would be about 100 μm (or higher).

It should be noted that in comparison with the previous design presented in (Kalal *et al.*, 2007*b*) the seeding laser beam is now entering the reactor chamber through the same entrance window as used by the corresponding irradiation beam, thus improving the chamber robustness. In this new scheme, the custom-made mirror (CMM) design deserves to be discussed in more detail. In fact, all what will be written in this respect is also valid for the design of the final mirror from (Kalal *et al.*, 2007*b*), where no details were provided. Properties required from CMM are determined to a large degree by an issue connected with the non-converted higher harmonic which could penetrate the target chamber. This part of the returning beam will not be deflected by target displacement compensation system (TDC), thus potentially damaging the symmetry of the pellet irradiation. More details to this issue can be found elsewhere (Kalal *et al.*, 2010*b*).

It was already explained that the SBS-PCM approach exhibits the self-navigation properties. However, these nice features can become useful only under the expectation that the

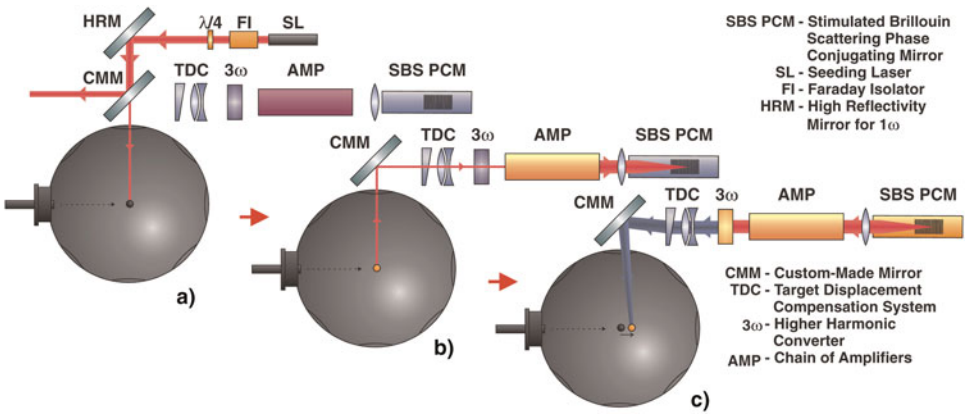

Fig. 35. (Color online) (**a**) at the right moment (determined by careful tracking) when the injected pellet is approaching its best interaction position, a low energy seeding laser pulse (glint = red line) is sent to illuminate the pellet; (**b**) reflected seeding laser pulse is collected by the focusing optics and amplified on its way to the SBS PCM cell; (**c**) amplified pulse is reflected by the SBS PCM cell, amplified once again, converted to higher harmonic (blue line), and automatically aimed at the moving pellet by the target displacement compensation system (TDC) for its final high power irradiation. TDC is a completely passive system having its optical components appropriately designed for every individual channel taking advantage of their index of refraction dependence on the wavelength. The custom-made mirror (CMM) design depends on the selected set-up and is discussed in detail in the main body of the work.

https://doi.org/10.1017/S0263034611000644 Published online by Cambridge University Press

low energy illumination of the pellet took place as required. Our approach to this issue is the following: when the high energy irradiation of the injected pellet is regarded as potentially realistic (sometimes in the future, whatever would be the actual technology employed), it should be much easier to achieve illumination only with very low energy laser beams. Therefore, we do not regard this as an issue we need to deal with. Instead, we are proposing for consideration another, even much simpler idea: to avoid any need for glint lasers different aiming from shot to shot at all. In this approach, two scenarios could come into consideration: (1) using the glint laser spot size sufficiently smaller than the pellet diameter (say about 2 mm) to make sure that in the case of acceptable delivery the whole laser spot will always fit on the pellet surface; (2) using the glint laser spot size sufficiently larger than the pellet diameter so the pellet would always fit inside of that beam as a whole. The collection angle of the low power first harmonic (illumination stage) and the high power higher harmonic focusing on the pellet (irradiation stage) can be designed as fully independent (see Fig. 2 in Kalal *et al.* (2007*a*) or Ostermeyer *et al.* (2008)).

The illumination schemes considered above deserve some comments to be made. It should be emphasized that for the purpose of the SBS-PCM approach, so far these schemes were verified experimentally only in case of a single laser beam (more details will be provided further in this work). And there are several issues worth mentioning that might come into consideration while evaluating these schemes suitability in case of high number of the beams (typically about 1000). For example, under this scenario, a massive overlapping would be taking place (issue of hot spots). However, it is assumed that such a high number of glints could provide more illumination symmetry to the target. In combination with the potential surface plasma effect, the whole target might look (in an ideal case) like a point source to the optics placed well outside of the chamber. Further investigation is thus needed to resolve these issues.

One of the main advantages of this self-navigating illumination/irradiation concept is the fact that the optical elements taking care of each particular laser beam shift can be especially designed once for all. Featuring no moving parts (at least on the high power side) this technique can significantly simplify design of lasers and the beam transport optics allowing for substantial increase in the number of laser beams employed. Every laser beam can operate as an independent driver with much lower energy per pulse, thus making the required repetition rate easier to achieve. With many laser beams available, any shape of the final irradiating pulse should be realizable by considering neighboring drivers as creating a required pulse shape when combined together on the pellet surface using different delays, and amplifications of individual drivers. More details concerning these issues can be found in Ostermeyer *et al.* (2008). However, the issue of the pulse shape might be also dealt with the more usual way as done e.g., on National Ignition Facility (NIF) (i.e., obtained directly from the sophisticated oscillator). Or it could be a combination of both ways.

In designing individual laser drivers, several key parameters need to be taken into consideration: (1) to keep the energy of initial illumination of the injected pellet low enough to ensure that no harm (e.g., preheating) would be done to the pellet itself, (2) amplification achieved by the chain of amplifiers would be sufficient to bring the energy of the pulse to the level about 1 J before entering the SBS-PCM cell (this particular value was selected to ensure that the actual SBS-PCM reflection will be performed for the energy values with low dependence of the reflection coefficient on the incident energy in order to minimize the energy fluctuation), (3) the final energy of the pulse for the pellet irradiation would be about 1 kJ (this effectively assumes about 1000 individual channels). As an important parameter to also be taken into consideration is the energy extraction efficiency from individual amplifiers.

In order to test this SBS-PCM approach to IFE, a new series of experiments was performed. Diagram of the experimental setup used for verification of the proposed design is shown in Figure 36.

Compared to the successful experiments realized earlier (Kalal *et al.*, 2008*a*, 2010*a*), which confirmed the self-navigation principle (the change of the trajectory achieved by the incorporated conversion to the second harmonic — green line), in these new experiments, a complete individual laser channel setup was assembled — including the pellets realized by the static steel balls 4 mm in diameter. This kind of pellets was deliberately chosen as capable to withstand much higher illumination energies compared to the real ones as the higher illumination energies became necessary due to the insufficient amplification available in the laser channel (with only two amplifiers employed). The laser was working in the Q-switched regime with the pulse length of 8.66 ns. It should be noted that during these tests the laser channel energies were much lower compared to the real ones (just below 1 J after amplification and frequency conversion). In the SBS cell, a heavy fluorocarbon liquid FC-75 was used for the SBS generation. It is a well-known

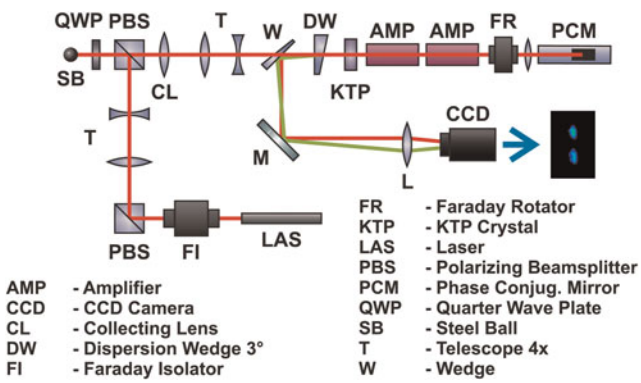

Fig. 36. (Color online) Schematics of the experimental setup used for verification of the SBS PCM approach to IFE. As the steel ball was stationary the amplified beam was on its way back to the target deflected in order to verify the displacement feature of the scheme.

https://doi.org/10.1017/S0263034611000644 Published online by Cambridge University Press

SBS material which gives high reflectivity and excellent fidelity (Yoshida, 1997).

In this context, the injected pellet survival conditions in the period between its low energy illumination and subsequent high energy irradiation were also studied. The upper limits on the acceptable amount of energy absorbed during the illumination stage for the direct drive pellets with parameters close to those currently considered (4 mm in diameter, 45 μm thick polystyrene shell, 200 μm thick fuel layers) were calculated. In these calculations, it was simply assumed that the target material absorbed some part of the laser energy (most likely only a very small part of that energy) at the boundary of the cryo-layer. The mechanism itself of this absorption was not considered. It was found that this absorbed energy, which leads to the cryogenic layer temperature increase by 1 K (from 17 K to 18 K) in the area of cryo-layer/shell wall contact during 1 μs, is about 6 mJ in the case of (deuterium-deuterium (DD) and 14 mJ in the case of deuterium tritium (DT) (see Kalal *et al.* (2010*b*)). Knowledge of these energies is crucial for a proper design of individual laser channels — in particular, their total amplification needed for high quality SBS-PCM reflection. The acceptable energies obtained are about ten times higher than those conservatively estimated in our very first laser channel design (see Slezak *et al*., 2008).

ACKNOWLEDGMENTS

This work was supported by the International Atomic Energy Agency (IAEA) as a part of the coordinated research project "Pathway to Energy from Inertial Fusion – An Integrated Approach" (Research Contracts No. 13781 and 13758); by the Ministry of Education, Youth, and Sports of the Czech Republic Research Project LC528 and by the grant KONTAKT No. ME933; by the Czech Technical University in Prague grant No.: CTU0916314; and by the Grant Agency of the Czech Republic grant No. 202/08/H057. It was also supported by the Nuclear Research and Development Program of the Korea Science and Engineering Foundation (KOSEF) grant funded by the Korean Government (MEST) — grant code: M20090078160 and by R&D Program through the National Fusion Research Institute of Korea (NFRI) funded by the Ministry of Education, Science and Technology.

5. 68 W PHASE CONJUGATE PICO-SECOND ND:YVO_4 LASER SYSTEM BASED ON A TANDEM BOUNCE AMPLIFIER (M. Ashihara, T. Yoshino, K. Hayashi, Y. Tokizane, M. Okida, K. Miyamoto, and T. Omatsu)

5.1. Introduction

High average power pico-second lasers have received much attention in several fields, such as nonlinear optics, laser ablation, and micro-fabrication. A side-pumped bounce amplifier based on a neodymium-doped vanadate (Nd:YVO_4 or Nd:$GdVO_4$) slab is a promising solution for developing high-average-power pico-second lasers, since it is capable of creating high single-pass gain (>1,000) without a regenerative amplifier geometry.

In particular, a phase conjugate master oscillator power amplifier (PC-MOPA) system formed by a bounce amplifier and a phase conjugate mirror, organizing self-aligned multi-pass amplifier geometry, can produce high output powers with less degradation of the beam quality. To date, we have demonstrated a high average power (>26 W) PC-MOPA system with peak powers in the range of 2.8–6.8 MW and high beam quality ($M^2 < 1.5$).

In this work, we address the power scaling of a pico-second PC-MOPA system by incorporating a second bounce amplifier inside the PC-MOPA. Using this system, 68 W pico-second output was demonstrated at a pulse repetition frequency (PRF) of 100 MHz and pulse duration of 11 ps.

5.2. Experiments

5.2.1. *Experimental Setup*

Figure 37 shows the experimental setup of the phase-conjugate amplifier system based on a tandem bounce amplifier. A commercial continuous-wave mode-locked Nd:YVO_4 laser, having pulse duration of 7.3 ps and a PRF of 100 MHz, was used as the master laser. The master laser power was 12 mW. The amplifier used was a transversely diode-pumped 1 at.% Nd:YVO_4 slab with dimensions of 20 mm × 5 mm × 2 mm. A continuous wave 808-nm laser diode array stack used as a pump source was line-focused by a cylindrical lens ($f = 20$ mm) on the pump face of the amplifiers. The maximum pump power was measured to be 130 W.

Polarizing beam splitters, a Faraday rotator, and a half-wave plate (HWP_1) formed an optical isolator to prevent feedback to the master laser. The master laser beam was focused by a spherical lens, L_1 ($f = 1000$ mm), and a cylindrical lens, VCL_1 ($f = 100$ mm), so that the master laser beam spatially matched the ellipsoidal gain volume. The amplified master laser beam was relayed to the second amplifier with 4*f* imaging optics formed by two spherical lenses L ($f = 100$ mm). The second amplifier was identical

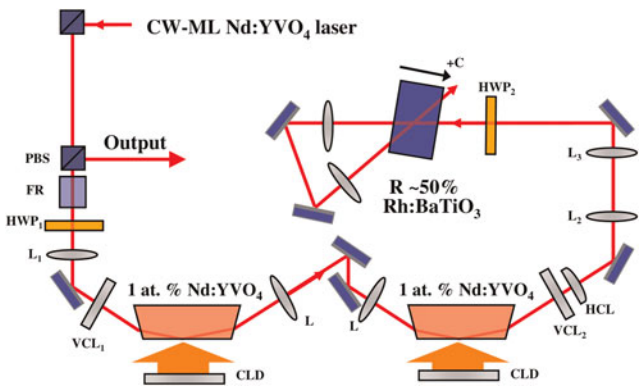

Fig. 37. (Color online) Experimental setup of a pico-second phase conjugate laser system formed by a tandem bounce amplifier and a photorefractive phase conjugate mirror.

https://doi.org/10.1017/S0263034611000644 Published online by Cambridge University Press

to the first amplifier. The external incident angles of the master laser beam and the amplified beam to the amplifiers were 18° with respect to the pump surface of the amplifiers.

After passing through two amplifiers, the amplified beam was collimated by two cylindrical lenses, VCL_2 ($f = 75$ mm) and HCL ($f = 100$ mm), and it was relayed to a phase-conjugate mirror based on an Rh:$BaTiO_3$ crystal by two spherical lenses L_2 ($f = 200$ mm) and L_3 ($f = 100$ mm). The polarization of the amplified beam was rotated using a half-wave plate HWP_2, so that it lay in the extraordinary plane of the Rh:$BaTiO_3$ crystal. The phase conjugation of the amplified beam was automatically feed back to the amplifiers. After that, it was ejected as an output by a PBS.

The $BaTiO_3$ crystal with 400-ppm Rh-ion doping and dimensions of 6 mm × 6 mm × 5 mm was cut at 0° relative to the normal to the *c*-axis, and its surfaces had an anti-reflection coating for 1 μm. Further crystal was also mounted on a copper block, and the block temperature was maintained at about 20°C by a water re-circulating chiller. A self-pumped phase conjugate mirror was formed by the $BaTiO_3$ crystal and an external loop cavity including 4*f* imaging optics ($f = 150$ mm). The angle of the external loop cavity was 15°, and its length was 600 mm. With this system, phase conjugation built up within a couple of minutes, and it typically exhibited 50% reflectivity. As related in previous publications, the loop cavity length was made much longer than the coherence length of the master laser (~3 mm) so as to prevent frequency-narrowing effects originated by the formation of reflection and 2*k* gratings.

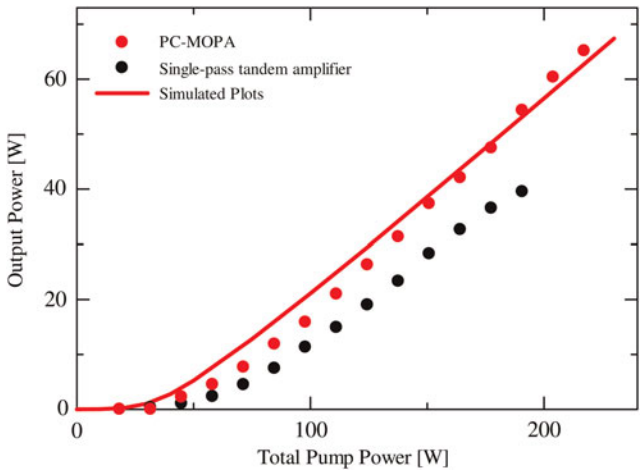

Fig. 38. (Color online) Experimental and simulated plots of the average output power as a function of the pump power.

5.2.2. *Experimental Results*

The average output power as a function of the pump power is shown in Figure 38. The pump power then was defined as the sum of the pump powers in two amplifiers, and the pump power ratio between the first and second amplifiers was unity. The output power was almost proportional to the pump power, and it reached up to 68 W at the maximum pump level (227 W). The corresponding energy extraction efficiency was about 30%, and the peak power was estimated to be >60 kW. In contrast, the output power in the single-pass tandem amplifier geometry without the phase conjugate mirror was limited up to 40 W at a pump power of 177 W.

The red curve in Figure 38 shows numerically simulated plots on the basis of the partitioned amplifier and continuous-wave gain saturation formula model (see Fig. 39) mentioned in our previous publication. The physical parameters used in the numerical simulation are listed in Table 1. There is good agreement between the experiments and the simulations.

Figure 40 shows the spatial form of the output from the system. The horizontal beam propagation factor, M_x^2, of the output was measured to be about 2.3 (Fig. 40c), while the incident beam onto the PCM had an M_x^2 of about 3.8 (Fig. 40b). And thus, the brightness of the output obtained by the PC-MOPA, defined as the output power divided by the M_x^2, was 3.2-times higher than that obtained merely by the tandem amplifier without the PCM. These results mean that the PCM can improve significantly the brightness of the output by compensating for the thermal aberration in the amplifier. Further improves of the beam quality will be

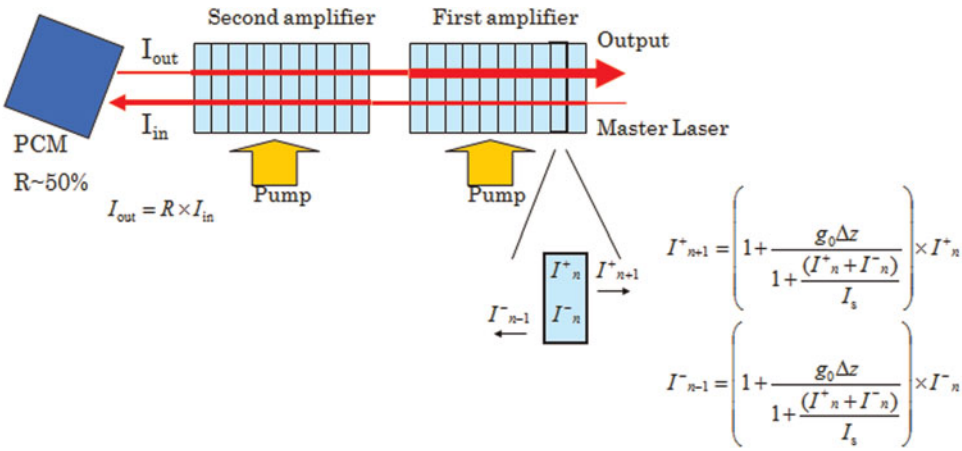

Fig. 39. (Color online) Numerical simulation model of the PC-MOPA output.

https://doi.org/10.1017/S0263034611000644 Published online by Cambridge University Press

Table 1. *Physical parameters in numerical simulations*

Saturation intensity I_s [W/cm^2]	1200	Phase conjugate reflectivity [%]	50
Beam spot size in amplifiers [cm^2]	3.3×10^{-3}	Δz [cm]	0.0002
Master laser power I_0^-[mW]	12	Small signal gain coefficient in the amplifier g_0/P_{pump} [cm^{-1}/W]	0.0475

possible by optimizing the relay optics to collect the amplifier beam onto the PCM and improving heat removal from the amplifiers.

Figure 41 shows the experimental auto-correlation trace of the output pulse. The output pulse width was broadened, and its pulse width was measured to be 10.8 ps, while the master laser had a pulse width of 5.8 ps. The pulse broadening effects were caused by spectrum narrowing effects due to a finite gain-band in the amplifier. The pulse width of the amplified output is written as follows:

$$\tau_p{}^2 = \tau_{p0}{}^2 + \frac{(16 \ln 2) \ln G_0}{\Delta\omega_a{}^2}, \quad (1)$$

where τ_{p0} is the initial width of pulse, G_0 is the small-signal gain of the amplifier, and $\Delta\omega_a$ is the frequency-bandwidth in Lorentzian atomic transition, respectively. Using the experimental parameters, the pulse width of the output was estimated to be 11.2 ps, which is consistent with the experimental value. By using the peak intensity ($\sim$700 kW/cm^2) of the output in the Nd:YVO_4 amplifier, the nonlinear refractive index ($\sim 10^{-18}$ m^2/W) of the Nd:YVO_4 crystal, and the crystal length ($\sim$2 cm), the B integral was estimated to be 8.5×10^{-4} rad, and thus, the pulse broadening effects originated by the third-order nonlinearity in this system is negligible.

5.3. Conclusions

We have demonstrated a phase conjugate laser system formed by a tandem diode-side-pumped Nd:YVO_4 bounce amplifier in combination with a photorefractive phase conjugate mirror. The maximum average power of 68 W was measured,

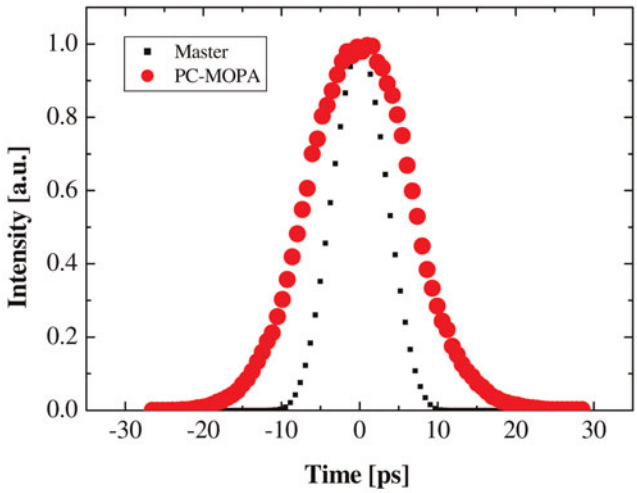

Fig. 41. (Color online) Intensity autocorrelation traces of the amplified output and master laser.

which is the highest value so far, to the best of our knowledge, previously obtained by PC-MOPA systems with a photorefractive phase conjugate mirror. A corresponding optical–optical efficiency of 30% was achieved.

Further improvement of the beam quality of the system will be possible by utilizing 880-nm pump diodes, which can reduce the heat loading in the tandem amplifier.

ACKNOWLEDGMENT

The authors acknowledge support from a Scientific Research Grant-in-Aid (19018007, 18360031) from the Ministry of Education, Science and Culture of Japan and the Japan Society for the Promotion of Science.

6. PHOTOREFRACTIVE TWO-WAVE MIXING AT 1.55 μM BASED ON TWO-PHOTON ABSORPTION IN A RH DOPED $BATIO_3$ AND TE DOPED $SN_2P_2S_6$ CRYSTALS (K. Toyoda, K. Miyamoto, T. Omatsu, and A.A. Grabar)

6.1. Introduction

Photorefractive nonlinear wave mixing at the telecommunication wavelength 1.55 μm has been intensely investigated,

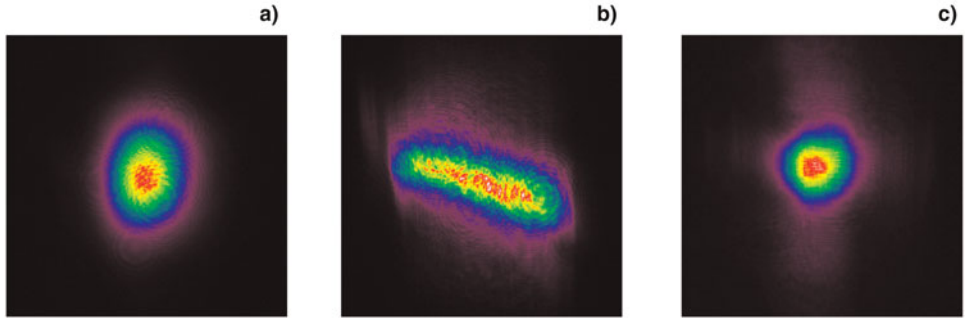

Fig. 40. (Color online) Spatial forms of the output. (**a**) Master laser output, (**b**) output from the MOPA without PCM, and (**c**) output from the PC-MOPA.

https://doi.org/10.1017/S0263034611000644 Published online by Cambridge University Press

because it enables us potentially to demonstrate beam combination, beam cleanup, and optical phase conjugation in combination with fiber optics. Photorefraction at this wavelength regime has been investigated mostly in semiconductors such as CdTe:V, since conventional ferroelectric materials, i.e., Rh doped $BaTiO_3$ has property of very poor photorefractive sensitivity at this wavelength. However, the CdTe:V requires an additional large alternating current (AC) electric field (~4 kV/cm) and 1.3 μm stimulating illumination to achieve an efficient photorefractive two wave mixing gain.

Horowitz and Fischer (1996) have reported 1.55 μm femtosecond laser pumped photo-refraction owing to two photon absorption in an un-doped $BaTiO_3$ crystal. However, they focused on an existence of photorefraction, and they did not mention about quantitative photorefractive performances including two wave mixing gain.

In this work, we investigate 1.55 μm photorefractive two-wave mixing gain by two photon absorption in the Rh:$BaTiO_3$ crystal. Two-wave mixing gain of about 4.5 cm^{-1} was observed at the pump power of 500 MW/cm^2 in the 1.55 μm wavelength regime. A ferroelectric semiconductor material, tin thiohypodiphosphate ($Sn_2P_2S_6$, SPS), showing a relatively narrow band gap (~2.3 eV), a high charge mobility, as well as a large dielectric constant, is alternative to achieve photorefractive wave mixing at 1.55 μm regime. We also address improvement of two-wave mixing gain at 1.55 μm in Te doped $Sn_2P_2S_6$ by two photon absorption.

6.2. Experiments

Figure 42 shows two photon absorption of Rh:$BaTiO_3$ crystal as a function of the pump intensity measured by z-scan method. A pump laser used was a 1.55 μm femtosecond fiber laser (IMRA co.) with a pulse width of 100 fs and a pulse repetition frequency of 50 MHz. Two-photon absorption was evidenced by that absorption of the crystal was almost proportional to pump intensity. And the absorption of the crystal reached up to the saturation level above the pump intensity of 30–40 MW/cm^2.

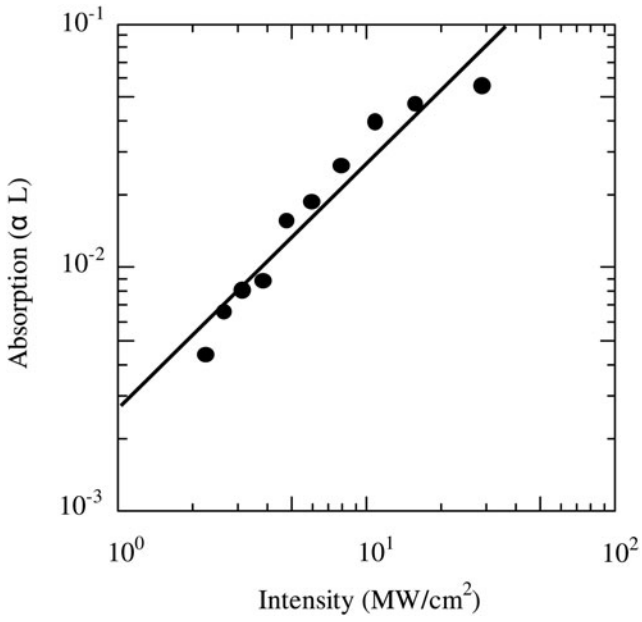

Fig. 42. Two photon absorption as a function of pump intensity in Rh:$BaTiO_3$.

Two-wave mixing gain due to two-photon absorption was also measured. Figure 43 shows a schematic diagram of an experimental setup. The laser used was a 1.55 μm femtosecond fiber laser (IMRA co.) with a pulse width of 100 fs and a pulse repetition frequency of 50 MHz, and its output was split into a *p*-polarized probe and strong pump beams with an intensity ratio of 1:9. The two beams were focused to be a ϕ50 μm spot onto a thin 45°-cut Rh:$BaTiO_3$ crystal (thickness 2 mm) and a Te doped SPS crystal, the angle between two beams was about 9°. With this setup, the effective interaction length between the probe and pump beams was estimated to be about 0.3 mm. We also optimized an optical delay of the pump beam to the probe beam, thereby yielding good temporal overlap between probe and pump beams. The power of the two beams was controlled by an attenuator.

Two-wave mixing gain exhibited the significant intensity dependence of the pump beam, and it reached up to about 4.5 cm^{-1} at the maximum pump level. The two-wave mixing gain in our experiment was less than that obtained by the continuous-wave laser pumping, and it was impacted by relatively large spectral bandwidth of 10–15 nm associated with the femto-second pulses. The crystal showed a faster temporal response (<100 s) than the un-doped $BaTiO_3$ (200–300 s), resulting from that the Rh ions formed shallow traps and they improved two photon absorption efficiency (Fig. 44).

Two-wave mixing gain in Te doped $Sn_2P_2S_6$ was also measured by using the same setup. A maximum two-wave mixing gain of 1.68 cm^{-1} was obtained at the pump intensity of 26 W/cm^2 (Fig. 45). To investigate contribution of two-photon absorption to photorefractive two-wave mixing, we also measured two-wave mixing gain based on one photon absorption by using the same setup. A 1.55 μm continuous-wave laser diode in combination with a fiber amplifier was used, and its output power was

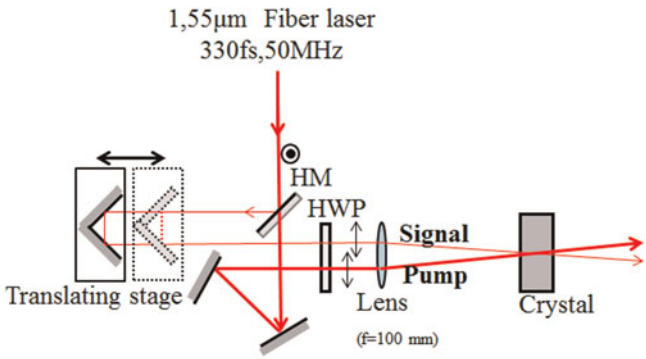

Fig. 43. (Color online) Experimental setup.

https://doi.org/10.1017/S0263034611000644 Published online by Cambridge University Press

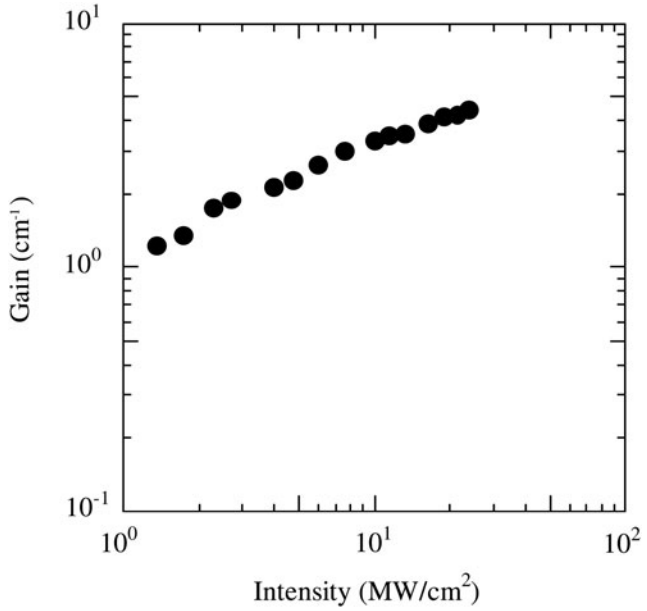

Fig. 44. Two-wave mixing gain as a function of pump intensity in Rh:$BaTiO_3$ based on two photon absorption.

about 200 mW. The effective two-wave mixing gain was impacted by too short interaction (~0.3 mm) between the probe and pump beams even at the maximum pump level, and it was measured to be 0.92 cm^{-1}. They evidenced that the two-photon absorption improved significantly the photorefractive activity at 1.55 μm in the SPS crystal. We also measured 1.55 μm two-wave mixing gain based on one-photon absorption by optimizing experimental parameters including the beam size and the incident angle of probe and pump beams onto the SPS crystal. Figure 46

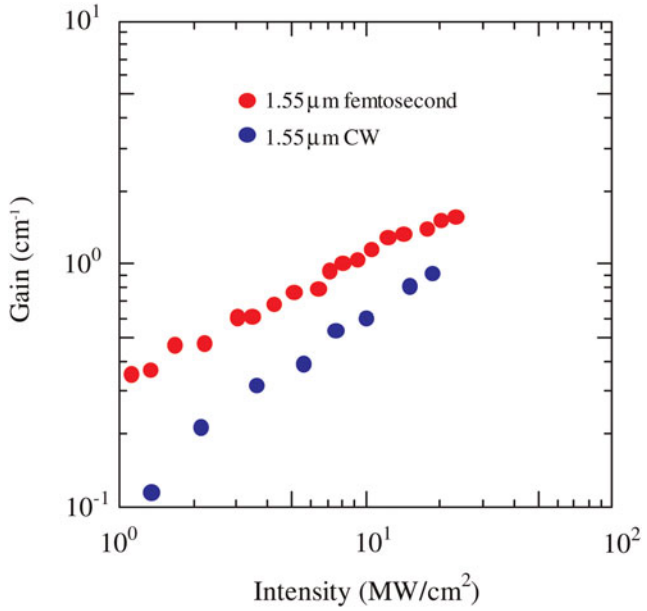

Fig. 45. (Color online) Two wave mixing gain as a function of pump intensity in Te: Sn2P2S6 using 1.55 μm CW and femtosecond laser.

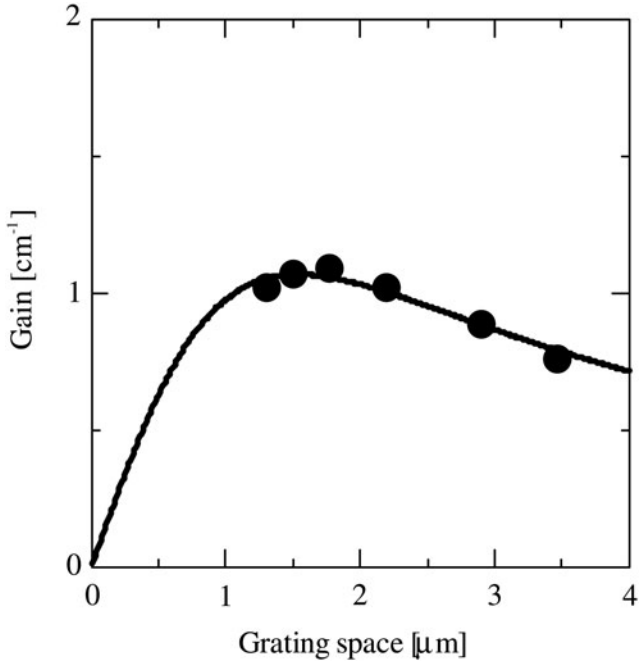

Fig. 46. Two-wave mixing gain as a function of the grating spacing in 1% Te-doped $Sn_2P_2S_6$ for the wavelengths 1.55 μm.

shows an experimental two-wave mixing gain as a function of the grating period formed by probe and pump beams. The pump beam intensity was then 28 W/cm^2, and a power ratio of the pump beam to the probe beam was 1:98. A maximum gain of 1.02 cm^{-1} at a grating period of 1.53 μm was measured, and it was still less than that observed by 1.55 μm femto-second laser. For the Rh:$BaTiO_3$ crystal, we could not observe any two-wave mixing gain based on one photon absorption at all.

6.3. Conclusion

We investigated the photorefractive two-wave mixing gain at 1.55 μm region based on two-photon absorption in an Rh doped $BaTiO_3$ and Te doped $Sn_2P_2S_6$ crystals. Two-photon absorption induced by high intense pulses provided by femto-second lasers improved significantly photorefractive activities. And thus, two-wave mixing gains of 4.5 cm^{-1} and 1.68 cm^{-1} in the Rh doped $BaTiO_3$ and Te doped $Sn_2P_2S_6$ crystals were obtained, respectively.

7. PHOTOREFRACTION IN AN FE:LINBO$_3$ CRYSTAL WITH FEMTOSECOND PULSES AT 800 NM (Md. M. Kabir, Y. Oishi, H. Suzuki, and F. Kannari)

7.1. Introduction

The formation of volume holographic grating in photorefractive (PR) crystals can be used for the dispersion compensation (Roblin *et al.*, 1987), storing (Acioli *et al.*,

https://doi.org/10.1017/S0263034611000644 Published online by Cambridge University Press

1991), shaping, and the amplification (Yao & Feinberg, 1993) of ultrashort laser pulses. PR volume gratings are also applicable as a self-pumped phase-conjugate mirror for short laser pulses (Jain & Stenersen, 1984). Yau *et al.* (1997) reported self-pumped phase conjugation (SPPC) in BaTiO3 with picosecond and femtosecond laser pulses at 800 nm. Joubert *et al.* (1989) first studied the temporal reversal of picosecond optical pulses by phase conjugation in Fe:LN.

In these early studies, the role of chirped volume grating for recording and amplifying broadband optical laser pulses was not explored. Nishioka *et al.* (2007) recently proposed that the chirped volume grating formed in a Fe:LN crystal can be utilized to amplify a few cycle femtosecond laser pulses. The PR effects in wide band gap (4 eV) LN (Beyer *et al.*, 2006) crystal with femtosecond laser pulses in the near-infrared regime can be governed by either linear one-photon or nonlinear two-photon absorption (TPA) using iron impurity centers, depending on the crystal doping concentration, and the intensity of the writing laser pulses. Although the proposal of femtosecond laser pulse amplification by chirped volume grating written in an Fe:LN crystal at 800 nm by Nishioka *et al.* (2007) was based on two-photon absorption and their experimental results were also interpreted with TPA, no research report shows direct evidence of TPA at 800 nm in Fe:LN crystals.

In this work, we demonstrate photorefractive two-wave mixing amplification of femtosecond laser pulses generated from a Ti:Al_2O_3 regenerative amplifier at 1 kHz in an Fe:LN crystal and confirm that one-photon absorption remains dominant in the Fe:LN crystal up to 100 GW/cm^2. A potential possibility of two-step holographic recording in a Fe:LN crystal using ultrashort laser pulses is also experimentally investigated.

7.2. Absorption of Fe:LN at 800 nm

The measurement of light absorption was performed using a balanced detection technique. The laser source was a mode-locked Ti:Al_2O_3 oscillator that generates 30-fs (full width at half maximum (full width at half maximum = FWHM)) femtosecond laser pulses at 800 nm and a repetition rate of 76 MHz. The spatial spot diameter (at $1/e^2$ intensity level) of the laser beam was about 2 mm. Absorption was measured up to about 5 GW/cm^2 for 76-MHz oscillator pulses. A 2-mm-thick Fe:LN (Fe concentration: 0.05 mol%) crystal was used to measure the light-absorption coefficient. The *c*-axis of the crystal was kept parallel to the light polarization. We also measured the light absorption of the same Fe:LN crystal using laser pulses amplified by the regenerative amplifier at 1 kHz at an incident laser intensity ranging from 10 to 388 GW/cm^2.

Figure 47 shows the experimental results of the absorbed laser power for ordinarily polarized light. The absorption power almost linearly increases as the incident laser power increases up to about 100 GW/cm^2. The corresponding linear absorption coefficient is about 0.11 cm. On the other hand, an abrupt increase in the absorption coefficient was observed above 100 GW/cm^2. This highly nonlinear absorption starting at about 100 GW/cm^2 could be a multi-photon process associated with second-harmonics light (Von der Linde *et al.*, 1974). In fact, we observed substantial 400-nm second-harmonic emission from the crystal. Significantly, the crystal failed to exhibit any damage even at 388 GW/cm^2. From the obtained results, the pulses are obviously not subject to nonlinear absorption up to nearly the 100-GW/cm^2 intensity, and the PR effects induced in the Fe:LN crystal with illumination of the femtosecond laser pulses at 800-nm wavelength reflects one-photon absorption by the impurity iron centers. It has also been reported (Pettazzi *et al.*, 2007) that the refractive-index changes in pure LN crystal by TPA are negligible for 800-nm femtosecond laser pulses below 100 GW/cm^2, although even pure LN contains a low but significant amount of iron impurity at concentrations of 0.001 to 0.01 wt% (Clark *et al.*, 1973).

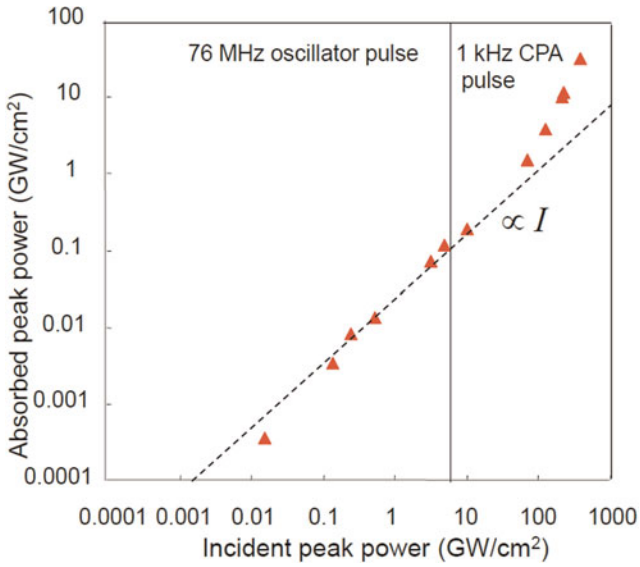

Fig. 47. (Color online) Absorption of 800-nm femtosecond laser pulses at peak intensity ranging from 15 MW/cm^2 to 388 GW/cm^2 in an Fe:LN.

7.3. Grating Formation with Chirped Laser Pulses

PR volume phase gratings were formed in the same crystal that was used to measure the absorption coefficient. Figure 48 shows the experimental setup for grating formation by low-energy 76-MHz pulses at 800 nm. 30 fs (FWHM) pulses were generated from a mode-locked Ti:Al_2O_3 laser oscillator with output energy of 5 nJ/pulse. The laser beam was split into two beams: a pump beam (I_p) and a signal beam (I_s) by a beam splitter (BS). A 40-mm-thick fused silica block was used to stretch the temporal width of the signal pulse to 210 fs. The writing half-angle of the incident beams was fixed in such a way that grating spacing of 5.22 μm was formed in the crystal. The pump and signal beams entered the crystal symmetrically in a plane containing

https://doi.org/10.1017/S0263034611000644 Published online by Cambridge University Press

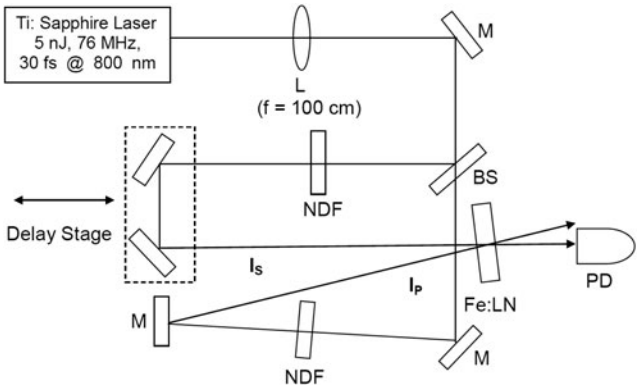

Fig. 48. Experimental setup for monitoring grating formation in TWM experiment. BS = Beam Splitter, M = Mirror, NDF = Neutral density filter, PD = Photo-detector, and L = Lens.

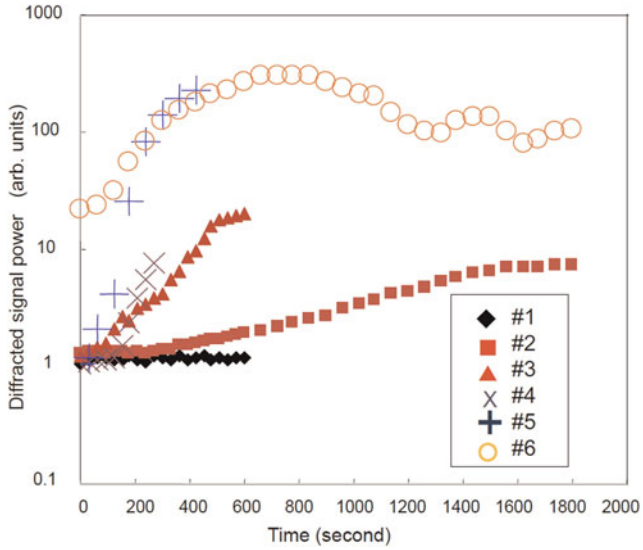

Fig. 49. (Color online) Temporal evolution of diffracted signals of pump beam of 800-nm cw and femtosecond pulse lasers generated from a mode-locked Ti:Al_2O_3 laser and a regenerative chirped pulse amplifier (CPA) in TWM experiments. Experimental conditions and highest diffraction efficiencies were summarized for each plot symbol in Table 2.

the crystal's *c*-axis so that the grating vector became parallel to the *c*-axis of the crystal. The polarization of the writing beams was also made parallel to the crystal's *c*-axis. The spatial spot diameter (at $1/e^2$ intensity level) of the two beams was 2 mm. A 100-cm focal length lens was used to adjust the beam diameter onto the front face of the crystal.

We performed grating generation using strong amplified laser pulses at 800 nm intensity level of the two beams was 2 mm. A 100-cm focal length lens was used to adjust the beam diameter onto the front face of the crystal. We performed grating generation using strong amplified laser pulses at 800 nm, produced by the regenerative chirp pulse amplifier (CPA). The output energy of the amplified laser pulses at a repetition rate of 1 kHz was 0.4 mJ/pulse after the pulse compression. The shortest pulse width (FWHM) of the output pulses after the compression was about 50 fs. The experimental setup including a pulse shaper was almost the same as that with the oscillator laser pulses (Fig. 48). The pump pulse width stretched by the 40-mm-thick fused silica block was 166 fs.

The experimental results for the evolution of the diffraction intensity from the PR grating written by laser pulses generated from the amplifier are shown in Figure 49. The summary is listed in Table 2. The diffracted signal from the recorded gratings written by unstretched pulses is extremely low. For the unfocused beam recording condition (2-mm beam diameter), a maximum diffraction efficiency of 0.8% was obtained for writing pulse peak intensities of $I_p = 2.63\ \mathrm{MW/cm^2}$ and $I_s = 0.11\ \mathrm{MW/cm^2}$. Here, we defined the diffraction efficiency as the fraction of the average power of the diffracted pump beam relative to the incident pump beam power. On the other hand, for a stretched signal pulse at $I_s = 0.012\ \mathrm{MW/cm^2}$ and an unstretched pump pulse at $I_p = 2.63\ \mathrm{MW/cm^2}$, a maximum diffraction efficiency of 4.8% was obtained after 1800 s. For the focused beam recording condition (0.46-mm beam diameter), when the signal pulses were not stretched ($I_p = 58.3\ \mathrm{MW/cm^2}$, $I_s = 2.44\ \mathrm{MW/cm^2}$), we observed extremely weak diffracted signal at a diffraction efficiency of about 0.8%. However, when the signal pulse was stretched ($I_p = 58.3\ \mathrm{MW/cm^2}$, $I_s = 0.27\ \mathrm{MW/cm^2}$) a maximum diffraction efficiency of 13% was obtained after 600 s.

Note that when we formed the PR grating with continuous wave (cw) laser beams at 800-nm wavelength, the diffraction efficiency was always higher than that of the pulse recording for both the unfocused and focused beam recording conditions for a particular recording time for the same average recording powers at ($I_s = 2.5\ \mathrm{W/cm^2}$ and $I_p = 5.5\ \mathrm{W/cm^2}$) and ($I_s = 59\ \mathrm{W/cm^2}$ and $I_p = 126\ \mathrm{W/cm^2}$) (Fig. 49). This higher diffraction efficiency attributes to better visibility of the photo induced gratings and perfect phase matching on the diffraction caused by monochromatic light.

With the amplified laser pulses operating at 1 kHz, we obtained maximum diffraction efficiency of 17% after 780 s when we applied peak pulse intensities $I_p = 15\ \mathrm{GW/cm^2}$ and $I_s = 31\ \mathrm{GW/cm^2}$ to the pump pulse (166 fs), and the signal pulse (50 fs), respectively. The main obstacle in generating high diffraction efficiency from the grating formed by the femtosecond laser pulses is its extremely short coherence length. Because of this extremely short coherence length (short pulse duration), the grating width formed by two interfering pulses is much smaller than that of the beam overlapping width. Therefore when two Fourier transform limit femtosecond pulses overlap in the crystal, they can only form a few high contrast interference fringes in the central region of the overlapping beams, whose width is on the order of micrometer and only the central portion of the interacting beams can diffract from this thin grating, resulting in low diffraction efficiency. On the other hand, when we stretch one of the writing pulses, because of its longer duration, the grating width increases, as a result, a relatively

https://doi.org/10.1017/S0263034611000644 Published online by Cambridge University Press

Table 2. *Sum mary of diffractive volume grating formation. Lines 1–6 correspond to plots in Figure 3*

Corresponding plots in Figure 3	Beam diameter [mm]	Intensity [W/cm^2]		Pulse width [fs]		Diffraction efficiency [%]
		Pump	Signal	Pump	Signal	
#1	2	2.63×10^6	0.11×10^6	30	30	0.8
#2	2	2.63×10^6	0.12×10^5	30	210	4.8
–	0.46	5.83×10^7	2.44×10^6	30	30	0.8
#3	0.46	5.83×10^7	0.27×10^6	30	210	13
#4	2	5.5	2.5	CW	CW	–
#5	0.46	5.9×10^1	1.26×10^2	CW	CW	>15
#6	2	1.5×10^{10}	3.1×10^{10}	166	50	17

large portion of the interacting beams diffracts from this wider grating and produces relatively high diffraction efficiency. However, the possibility of degradation exists in the phase matching of different frequency components when they diffract from the gratings formed by frequency components other than their own, even in chirped volume grating.

A two-wave mixing amplification experiment was also carried out with high-energy laser pulses operated at 1 kHz. The average power ratio of the signal to pump beam was kept to 1:17.4. The average power of the pump pulsed beam was 260 mW, and the pump pulse was stretched from 50 to 480 fs by a fused silica glass block. The average power of the signal beam was 15 mW. The amplification of the weak signal pulse by 34% was measured. By applying a proper amount of frequency chirp to the pump pulse and setting small grating spacing, higher amplification might be achieved. The amplified signal pulse shifted slightly toward the high-frequency components due to the phase-mismatched diffraction of different frequency components from the secondary gratings caused by the two wave mixing (TWM) of the different frequency components of the interacting beams.

7.4. Two-Step Holographic Recording

The most effective approach to record near infrared (NIR) or infrared (IR) femtosecond laser pulses within short times is a two-step recording technique using short-wavelength gating laser pulses. The principle of gated recording can be understood by a two-center charge transport model (Jermann *et al.*, 1995) (Fig. 50). Iron dopants lead to Fe^{2+}-centers that are "deep" levels, whereas the second Nb_{Li}^{+5} center is more "shallow." Electrons can be excited from Fe^{2+} by short-wavelength gating pulses, forming Fe^{3+}. Electrons are excited either to the conduction band or to the shallow traps, resulting in the formation of the Nb_{Li}^{+4} state. NIR/IR laser pulses have insufficient energy for the excitation of electrons from the deeper Fe^{2+} sites to the conduction band. By illuminating the crystal with short-wavelength gating (blue or green) light G, shallow traps are filled, and the crystal will therefore be sensitized for subsequent holographic recording with NIR/IR light from the Nb_{Li}^{+4} centers.

To verify the two-step recording scheme, we employed 1.06-μm recording laser pulses and 532-nm (SHG) gating pulses to form a volume hologram. The incident laser energy of the 1.06-μm recording pulses was 7.8 mJ/pulse and the laser pulse width was 15 ns, whereas the incident laser energy of the 532-nm gating pulse was varied at 0.3, 1, and 7 mJ/pulses. The pulse repetition rate was 20 Hz. Without the gating pulse no diffraction was observed by a HeNe reading laser. Figure 51 shows the temporal evolution of the gratings at various gating laser energies. The summary is listed in Table 3.

During the two-step recording experiment with femtosecond lasers, second harmonic generation femtosecond laser pulses uniformly irradiate the crystal at the same repetition rate as the 800-nm laser pulses. Since the gating pulses also act as an erasing pulse, the incident laser fluence and the delay time must be adjusted to obtain the highest diffraction efficiency.

We formed gratings in the same crystal by two-step excitation process using the recording setup that resembles the one in Figure 48. The recording pulse peak intensities and pulse widths for the pump and signal beams were identical as those used in the one-step excitation recording process. A 400-nm femtosecond laser pulse (230 fs) of peak intensity 84 MW/cm^2 was simultaneously allowed to sensitize the

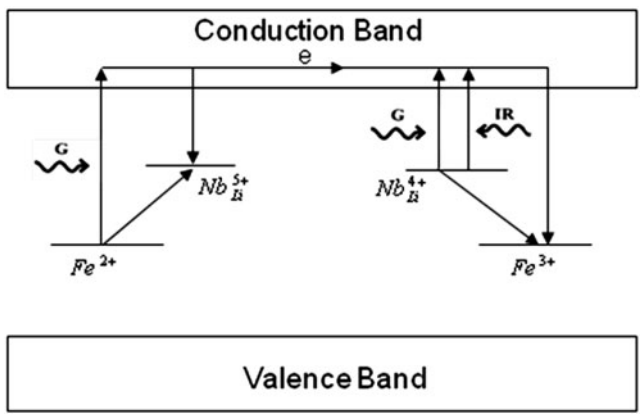

Fig. 50. Band diagram for two-center charge transport model in Fe:LN. The arrows indicate the excitation and recombination of electrons.

https://doi.org/10.1017/S0263034611000644 Published online by Cambridge University Press

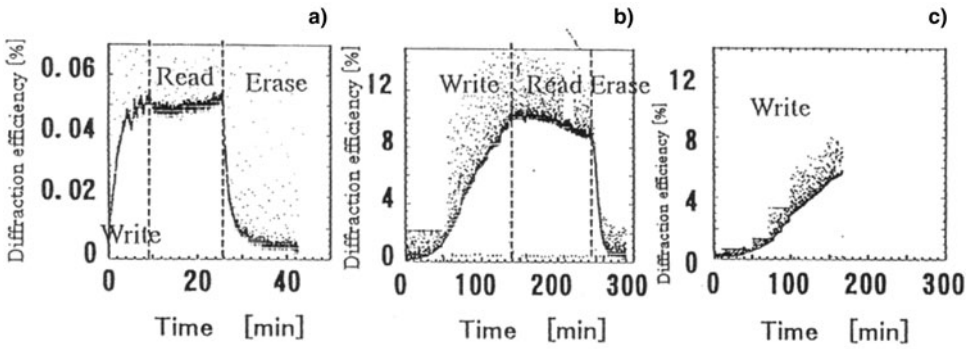

Fig. 51. Temporal evolution of volume holographic gratings in a scheme of two-step writing with 1.06-μm recording pulse and 532-nm gating pulse at incident energy of (**a**) 7 mJ, (**b**) 1 mJ, and (**c**) 0.3 mJ.

Table 3. *Summary of two-step holographic recording using ns-laser pulses*

Pulse energy of 1-μm writing beam [mJ]	Pulse energy of 532-nm assisting beam [mJ]	Different efficiency [%]
7.8	None	0
7.8	0.3	6
7.8	1	10
7.8	7	0.05

crystal during grating formation. A maximum diffraction efficiency of 9% was obtained after 540 s. The grating formation speed in the two-step excitation process is relatively faster than that of the one-step excitation process with high-energy CPA pulses, even in this case where second harmonic light was also generated. Therefore, the two-step excitation process can be an alternative recording scheme to efficiently form grating in Fe:LN crystal by high-energy and low repetition 800-m femtosecond laser pulses at 1 kHz.

7.5. Conclusions

We confirmed that one-photon absorption is dominant in Fe:LN crystal up to $100\,\mathrm{GW/cm^2}$ and demonstrated volume phase grating formation in Fe:LN crystal for the first time to the best of our knowledge by high-energy chirped intense 800-nm femtosecond laser pulses with a repetition rate of 1 kHz. Maximum diffraction efficiency of 17% was obtained at a total pulse peak intensity of $46\,\mathrm{GW/cm^2}$. We also found that the two-step excitation process with the assistance of short wavelength laser pulses effectively forms a volume grating in Fe:LN crystal by 800-nm femtosecond laser pulses.

ACKNOWLEDGMENTS

This research was supported by a Grant-in-aid from the Ministry of Education, Culture, Sports, Science, and Technology, Japan for the Photon Frontier Network Program.

8. DESIGN AND SPATIAL MODE ANALYSIS OF A SELF-ADAPTIVE LASER OSCILLATOR FOR WIRELESS TRANSMISSION OF ENERGY (C. Schaefer)

The wireless transmission of energy by using electromagnetic waves was already proposed more than hundred years ago (Tesla, 1904) and tested since then in numerous experiments. Beside near-field methods that are capable of transmitting energy over up to some m distance, far-field techniques using microwaves or lasers were found to be applicable mostly in space where vacuum facilitates beam propagation and a required direct line from the transmitter to the receiver is often available. Due to the fundamental law of diffraction, the latter is favored as a more compact solution to transmit energy to small-sized objects in space such as satellites, space probes, and planetary rovers, which presently still carry their own energy system onboard.

In such applications, the energy converting photovoltaic cell area usually measures about the laser beam diameter at the receiver. Hence, it is necessary to point the laser beam precisely onto the receiver to achieve high transmission efficiencies. In the past, closed-loop optoelectronic control systems could perform this task with a considerable amount of complexity and calculation power (Steinsiek *et al.*, 2003). In contrast, modern microwave transmission systems are using automatic retro-directive systems that apply phase conjugation to a received signal to track the receiver with its phased-array antenna (Miyamoto & Itoh, 2002). An optical method based on similar retro-directive techniques would simplify the system and increase its applicability.

This work examines the recently proposed method in Schäfer (2010) where the adaptive beam pointing concept is modified to continuous wave radiation. Since the resulting setup resembles a self-adaptive laser resonator (Udaiyan *et al.*, 1998), existing self-consistent spatial mode analysis was applied and extended using the ABCD-law (Siegman, 1986). In this method, Gaussian beams are described by the complex beam parameter q that is connected to the beam radius w and curvature R over the relation $q^{-1} = R^{-1} - i \cdot \lambda/(\pi \cdot w^2)$ (λ: wavelength) and traced to find the

https://doi.org/10.1017/S0263034611000644 Published online by Cambridge University Press

self-consistent mode in a given cavity. The here considered self-adaptive laser resonators are characterized by a ring cavity where a four-wave mixing process occurs inside an optical nonlinear medium (Udaiyan *et al.*, 1998). According to Eq. (2) in that publication, the calculation must be based on a material with third order optical nonlinearity.

At first, the output coupler mirror in the basic setup was replaced by a retro-reflector that keeps the original equations unchanged. An analytical expression was then found for $d > 0$ (d = distance nonlinear crystal — retro-reflector). Furthermore, the lens-in-loop oscillator was found to be analytically solvable over a third-order complex polynomial equation. But due to the enormous length of the final expressions, a numerical method was found to be more practical (Rosas *et al.*, 1998) and applied in further calculations. The existing formalism was extended to $d > 0$ by taking $d = \mathrm{N} \times \mathrm{L}$ where N is an integer and L the length of the ring-cavity. Transient solutions for resonators up to $N \approx 1000$ were computed but a strong increase of required iterations n for convergence set a practical limit to N. The obtained results were verified to the earlier achieved analytical results.

To meet the requirements for a realistic link with regard to required spot sizes and power transmission efficiency (fraction of light that falls onto the photovoltaic cells over the total amount of incident light on the receiver), a general resonator configuration was examined (Fig. 51). Here, the cat's eye retro-reflector with Gaussian aperture that represents the photovoltaic area, is supposed to be installed on the receiver while all other elements are part of the transmitter. Although a hard aperture as photovoltaic cells and telescope exit would be chosen in a real setup, a Gaussian aperture was considered here for compatibility to the applied formalism.

This setup allowed finding parameters that were applied in a power transmission scenario tested in the past (Steinsiek *et al.*, 2003) where a laser with $\lambda = 532$ nm and beam propagation factor of $M^2 = 5.5$ was used to transmit energy over $d = 100$ m onto a receiver of $r = 2.5$ cm radius.

Table 4 summarizes the input parameters of the numerical computation that leads to the aforementioned scenario. The desired power transmission efficiency was set to $\eta = 95\%$ so that the Gaussian aperture size on the receiver could be determined to $a_{RR} = 5.7$ mm. The transmitter aperture could be found over the diffraction law ($a_T = 5.4$ mm), assuming a plane wave at its exit (condition $R_{a1} \rightarrow \infty$). L was chosen to some practical value ($L = 50$ cm) leading to $N = 200$. To ensure a constant wave mixing position, x and f_3 were chosen close to a 4-f imaging configuration with $x = 0.55 \cdot L$ and $f_3 = L/4$. The small deviation from a true 4-f configuration was chosen for enhanced stability of the resonator. Due to the relatively small N and apertures sizes, transient solutions sufficiently converged already after $n = 1000$ iterations. By arbitrarily fixing one telescope parameter ($f_2 = 30$ cm), the remaining ones (defocus δ and magnification $M = f_2/f_1$) could be finally optimized successfully.

Table 5 summarizes the output of the calculation. The given result was calculated by a genetic algorithm that is supposed to find a global solution with rather rough precision than to optimize a solution to high precision. It is important that values of practical use could be achieved. At first, the desired beam radius of $w_0 = 2.5$ cm at the receiver could be obtained. Furthermore, radii for collinear beams at the wave-mixing center could be made equal ($w_1 \approx w_2$, $w_3 \approx w_4$). In particular, the radius of curvature of the outgoing beam R_{a1} could be maximized so that a M^2-times diffraction limited spot size w_0 was achieved at the receiver that makes expressions for the amplification requirements applicable that were derived elsewhere (Schäfer, 2010). These values thus demonstrate that the problem is in principal solvable. A subsequent optimization can lead to numerical solutions with high precision.

Although the parameters could successfully fit desired values, some problems were found. The final resonator setup is highly unstable with large half-trace parameters (HTP) for high power transmission efficiencies η (small a_{RR}/w_0). To stabilize the laser oscillation, the Gaussian aperture could be removed and the photovoltaic cells be placed behind the cat's eye mirror, which then becomes the output coupler. The drawback would be larger sized optics needed on the receiver to catch the entire laser beam. Finally, the free choice of f_2 indicates an abundance of one lens in the setup in Figure 52.

Table 4. *Input parameters to numerically compute the self-consistent mode*

N	L	x	f_3	δ	M	f_2	a_T	a_{RR}	M^2	n	λ
200	50 cm	27.5 cm	12.5 cm	−2.77 cm	8.33	30 cm	5.4 mm	5.7 mm	5.5	1000	532 nm

Table 5. *Computed parameters: w_x: Beam radii, R_x: Radii of curvature, HTP: Half-trace parameter, η: Power transmission efficiency*

$w_0 = 2.50$ cm	$w_1 = 637$ mm	$w_2 = 630$ mm	$w_3 = 255$ mm	$w_4 = 222$ mm	$w_{a1} = 3.77$ mm	$w_{b1} = 2.47$ cm	HTP	η
$R_0 = 102$ m	$R_1 = 4.55$ cm	$R_2 = -4.69$ cm	$R_3 = -4.75$ cm	$R_4 = 4.60$ cm	$R_{a_1} = -24.6$ km	$R_{b1} = 105$ m	44	0.95

https://doi.org/10.1017/S0263034611000644 Published online by Cambridge University Press

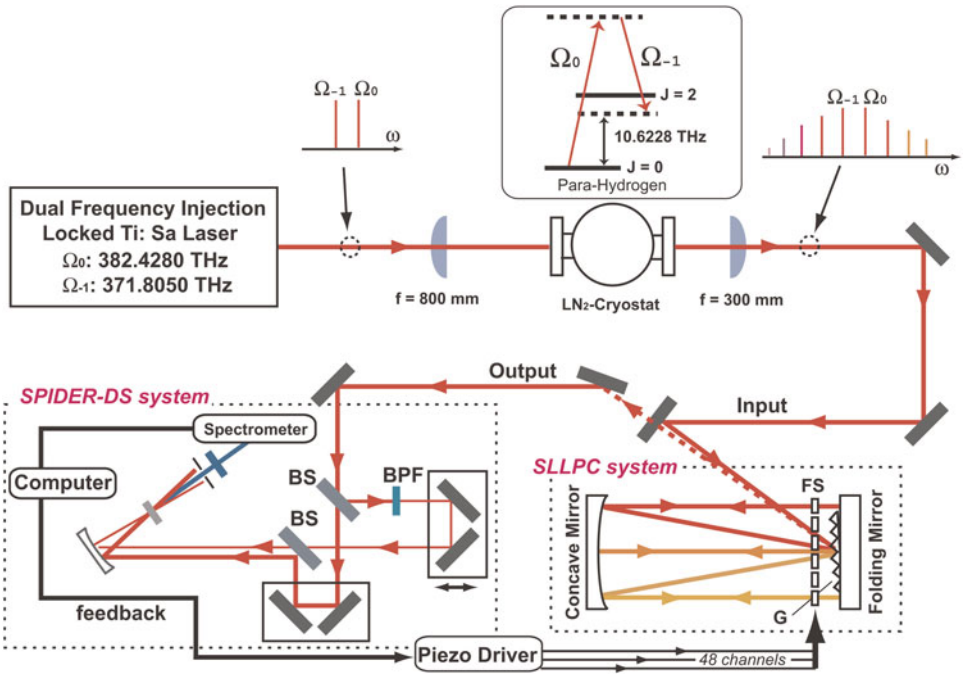

Fig. 52. (Color online) Schematic of experimental system for line-by-line manipulation of Raman sidebands. Here, SLLPC system = spectral line-by-line phase controller system, FS = Fused-silica plate, G = Grating, SPIDER-DS system = spectral phase interferometry for direct electric field reconstruction for discrete spectra, BPF = Band-pass filter, BS = beam splitter, BBO = Beta-barium borate crystal.

Furthermore, aperturing effects of the phase conjugating mirror were neglected in the above analysis. Such analysis can be tackled by the theory proposed by Jakeman and Ridely (1996). Since only a part of the retro-reflected light is incident onto the nonlinear medium, phase conjugation is, in general, incomplete. However, in case of no random aberrations ($m_0 = 0$ in Jakeman and Ridely (1996)), the aperturing effects should not affect the fidelity of the phase conjugation.

The proposed dynamic laser oscillator can be tested most conveniently by modifying a self-adaptive laser oscillator (Omatsu *et al.*, 2002). Since Rh:$BaTiO_3$ or $Sn_2P_2S_6$ crystals are usually used as nonlinear medium in such continuous wave type lasers, the derived theory must be modified from third order nonlinearity to photorefractive conditions. In this way, derived methods will be helpful to determine possible configurations and components for a successful experiment.

9. ADIABATIC MANIPULATION OF RAMAN COHERENCE AND ITS APPLICATION TO ARBITRARY OPTICAL WAVEFORM GENERATION (K.R. Pandiri and M. Katsuragawa)

Abstract

A highly stable, ultrahigh repetition rate train of user-specified, complex ultrashort pulses is synthesized by precise manipulation of spectral phases of adiabatically generated rotational Raman sidebands using a specially designed spatial phase controller and spectral interferometer.

9.1. Introduction

Recently, user-specified, complex waveform synthesis has gained significance in applications related quantum control, and optical communications (Levis *et al.*, 2001; Jiang *et al.*, 2007). Numerous attempts have been reported to generate such waveforms using Raman sidebands (Shverdin *et al.*, 2005; Katsuragawa *et al.*, 2005; Chen *et al.*, 2008). This work proposes a new method based on the combination of a suitable line-by-line phase controller with adiabatically generated discrete Raman sidebands for an efficient generation of arbitrary optical waveforms (AOWs). The advantage in this work over previous studies is adaptive, accurate measurement of the discrete spectral phase, and the line-by-line manipulation of spectral phases using a high damage threshold phase controller. The generated AOWs can be applicable to study pulse-shape dependence stimulated Brillouin scattering (Brent *et al.*, 1992) and selective enhancement of optical phonons (Hase, 1998).

9.2. Experimental Details

The experimental schematic is shown in Figure 53. The two pump laser radiations, Ω_0: 382.4280 THz (783.9186 nm) and Ω_{-1}: 371.8050 THz (806.3162 nm) are produced with a dual-frequency injection-locked nanosecond pulsed

https://doi.org/10.1017/S0263034611000644 Published online by Cambridge University Press

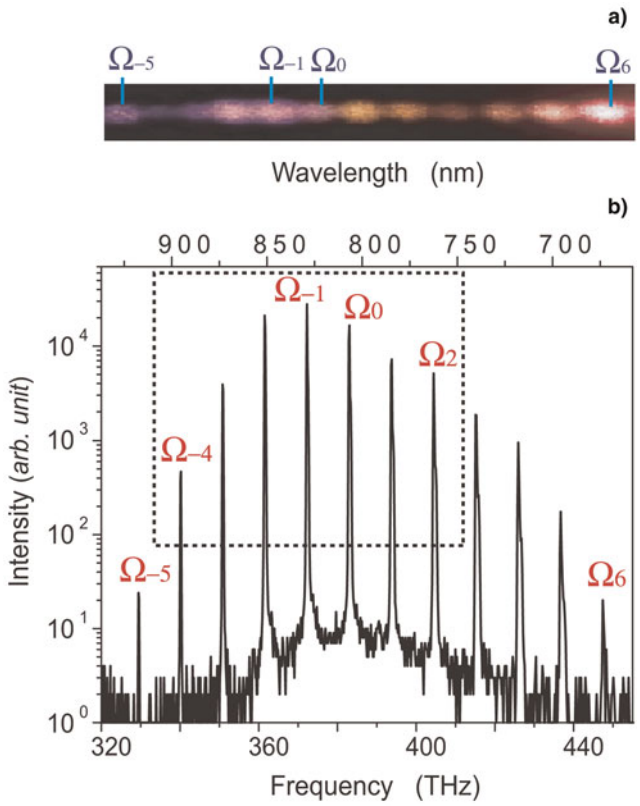

Fig. 53. (Color online) (**a**) Photographic image of Raman sidebands, (**b**) Raman sidebands spectrum from Ω_{-5} to Ω_6. Seven sidebands (Ω_{-4}: 339.936 THz to Ω_2: 403.674 THz) are chosen for line-by-line phase control to the target as highlighted by box.

Ti:Sapphire laser (Katsuragawa & Onose, 2005), which provide Fourier-transform limited 6-ns pulses (spectral width about 50 MHz) and completely overlap each other temporally and spatially. The differential frequency is slightly detuned by 990 MHz from the Raman resonance ($J = 2 \leftarrow 0$ transition of parahydrogen) to satisfy the adiabatic condition. The two pump laser beams are then loosely focused in the parahydrogen chamber (temperature: 77 K, density: 3×10^{20} cm^{-3}) with $f = 800$ mm lens to a peak intensity 4.5 GW/cm^2. Raman sidebands are generated in the forward direction (Sokolov *et al.*, 2000; Liang *et al.*, 2000; Suzuki *et al.*, 2008*a*) and then introduced into the spectral line-by-line phase controller (SLLPC) after being collimated with a $f = 300$ mm lens. The SLLPC is a spatial phase modulator consisting of 48 fused-silica plates and configured in a folded 4*f*-configuration (Suda *et al.*, 2001). The incident Raman sidebands are dispersed with a grating (600 grooves per mm) and each sideband is focused onto a single glass plate placed in the Fourier plane with the use of a concave mirror ($f = 0.5$ m). The change in the spectral phase of each sideband is accomplished by changing the angle of the corresponding fused-silica plate through a Piezo actuator (minimum resolution: ± 0.1 rad, which was limited by the minimum step voltage (1 V) applied to the Piezo in the spectral line-by-line phase controller system). The phase controlled Raman sidebands and the corresponding waveform in the time domain are characterized by using modified spectral-phase interferometry for a direct electric-field reconstruction system for discrete spectra (SPIDER-DS) (Suzuki, 2008*b*). The SPIDER-DS system operates rapidly and generates an error signal, which is fed back to the SLLPC system through a set of 48-channel digital-to-analog converters and amplifiers (Kanaka *et al.*, 2010).

9.3. Results and Discussions

The photographic image of generated Raman sideband and its spectrum are shown in Figure 54a and 54b, respectively. Twelve Raman sidebands, from Ω_{-5}: 329.3070 THz (910.3738 nm) to Ω_6: 446.1578 THz (671.9426 nm), are observed. The generated sidebands are collimated and guided to the SLLPC system. Among these sidebands, seven are chosen from Ω_{-4} to Ω_2 by partly blocking the others in space in the SLLPC (highlighted by box in Fig. 53b). This selection is done to restrict the Raman sidebands to those that could produce sufficient SPIDER-DS signals.

In this work, we precisely control the relative spectral phases of the Raman sidebands to a target "flat-relative spectral phase." This target implies Fourier-transform limited ultrashort pulse train with a pulse duration corresponding to the inverse of the frequency spacing of the Raman sidebands in the time domain. We reconstructed the intensity waveforms consisting of seven Raman sidebands in the time domain using spectral phase of Raman sidebands measured with SPIDER-DS and intensity of Raman sidebands. We can see that as a result of controlling the relative spectral phase to the target, a train of 17 fs ultrashort pulses (crimson line in Fig. 55) is formed with a 94-fs time interval (10.6-THz repetition rate), which precisely corresponds to the inverse

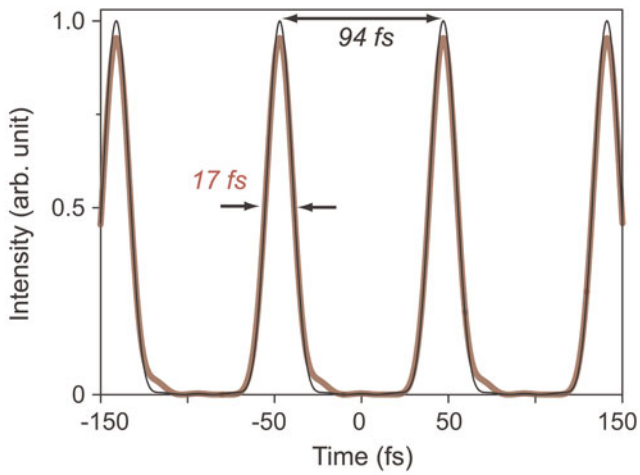

Fig. 54. (Color online) Reconstructed temporal intensity waveforms on the basis of the estimated spectral phases of the Raman sidebands. Crimson line is the waveform at the end of optimization process. Black line shows the Fourier-transform-limited waveform.

https://doi.org/10.1017/S0263034611000644 Published online by Cambridge University Press

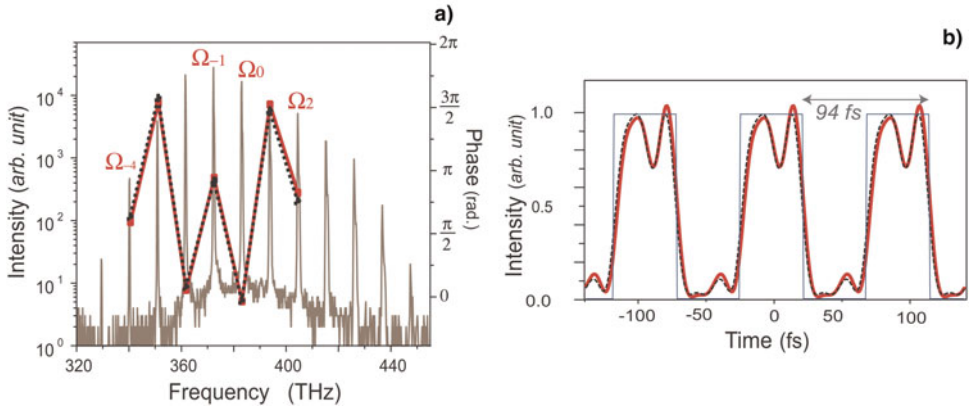

Fig. 55. (Color online) Generation of an ultrahigh repetition rate train of rectangular waveforms. (**a**) Spectral phases (Black dotted line = effective target, red line = achieved phase) and power spectrum (in gray) of the Raman sidebands. (**b**) A train of rectangular pulses = ideal waveform (blue line), effective target waveform (black line), and the achieved waveform (red line).

of the frequency spacing of the Raman sidebands. The pulse shape is in good agreement with the target Fourier-transform-limited ultrashort pulse (black line in Fig. 55).

We demonstrated AOW generation by line-by-line control on Raman sidebands. An example is shown for rectangular optical waveform generation. We performed numerical simulations to obtain effective target spectral phase and waveform (black line in Figs. 56a and 56b, respectively) using seven Raman sidebands in comparison with ideal target waveform (black line in Fig. 55b). To ensure that the spectral phases converge sufficiently with the effective target in the experiment, we followed an iterative phase manipulation process based on the precise phase measurement provided by the SPIDER-DS (error signal is produced from the SPIDER-DS measurement). The achieved spectral phase and waveform after iterative process is shown by red line in Figures 55a and 55b, respectively. A precise match with the effective target is found in both spectral phase and waveform shape except for small deviations due to the precision of the phase control (about ±0.1 rad).

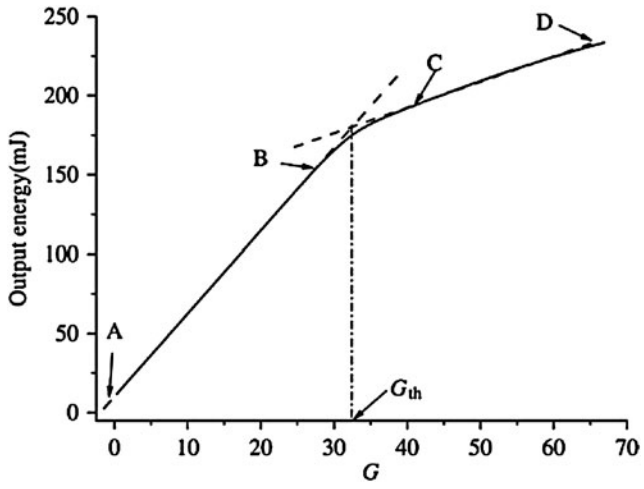

Fig. 56. Theoretical simulation of the dependence of the output energy on *G*. Line AB represents a linear increase of output energy below the SBS threshold. Line CD shows the optical limiting above the SBS threshold. Dashed lines, linear fit of lines AB and CD. The vertical dashed-dotted lines represent intersection points that correspond to the SBS threshold.

9.4. Conclusion

In conclusion, a highly coherent, discrete, wide-frequency spacing (10 THz) rotational Raman sidebands are phase manipulated to synthesize AOWs. Trains of Fourier-transform limited pulses and rectangular pulses are stably produced at an ultrahigh repetition rate of 10.6229 THz, analogous to an ultrafast function generator. The ultrahigh-repetition-rate, highly energetic AOW light source is demonstrated, and would be useful in high-energy laser physics.

10. MEASUREMENT OF STIMULATED BRILLOUIN SCATTERING THRESHOLD BY THE OPTICAL LIMITING OF PUMP OUTPUT ENERGY (W. Gao, Z.W. Lu, S.Y. Wang, W.M. He, and W.L.J. Hasi)

10.1. Introduction

Stimulated Brillouin scattering (SBS) has received general attention owing to its broad applications such as beam combination (Kong *et al.*, 2008, 2009*a*; Wang *et al.*, 2009*a*, 2009*b*; Ostermeyer *et al.*, 2008), Brillouin amplification of weak signals (Gao *et al.*, 2009; Lu *et al.*, 2009), optical limiting for laser protection in high-power laser (Hasi *et al.*, 2009*b*, 2009*c*), and slow light in optical fiber (Kovalev *et al.*, 2009; Lu *et al.*, 2007). Among the parameters that characterize SBS, the threshold value is of great importance. The definition of this parameter was first suggested to be pump intensity when the SBS amplification of the Stokes radiation overcomes its losses in a medium (Chiao *et al.*,

https://doi.org/10.1017/S0263034611000644 Published online by Cambridge University Press

1964). However, the amplification of the Stokes signal corresponding to the point of transition is too weak to detect for most SBS media because of the lower losses. Thus, the threshold is usually considered as the pump intensity when the SBS reflectivity reaches 1%, 2%, or 5% (Boyd *et al.*, 1990; Eichler *et al.*, 1995). As we know, this is a rather confusing experimental practice. Recently, Bai *et al.* (2008) presented a method to determine the threshold value of SBS by the point of the deviation of the value of the attenuation coefficients of wide- and narrow-line width lasers. We find it is feasible for some media (e.g., CS_2, water, etc.), but it is not for other media (e.g., FC-75, FC-72, etc.). Because the SBS still occurs in these media such as FC-75 and FC-72 when the wide-line width laser is used (Lee *et al.*, 2005*b*), the attenuation coefficients of the media will not be constants. Thus, the point of the deviation can not be determined.

Usually, it is more appropriate and convenient to characterize the steady-state or transient SBS by its threshold exponential gain, $G_{\text{th}} = gI_{\text{th}}L_{\text{eff}}$, where g is the SBS gain coefficient of the medium, I_{th} is the SBS threshold pump intensity, L_{eff} is the effective interaction length (Kovalev & Harrison, 2007; Bel'dyugin *et al.*, 2005). Moreover, the value of G_{th} can provide a practically important reference for the design of a Brillouin amplifier, since the optimum working point of the amplifier is usually near to G_{th} (Sternklar *et al.*, 1992). When the steady-state approximation is considered and 1% (SBS reflectivity) criterion for threshold is used, Boyd *et al.* (1990) predicted that the value of G_{th} in organic liquids is in the range 20–25, and Kovalev and Harrison (2007) found that the value of G_{th} decreases with increasing the interaction length in optical fiber. When a laser system with the nanosecond-order pulse width is used, for the most media (the phonon lifetime is usually between 0.1 ns and 10 ns (Erokhin *et al.*, 1986; Yoshida *et al.*, 1997)), the transient theory should be use to analyze the SBS process (Bel'dyugin *et al.*, 2005). Nevertheless, to our knowledge, the dependence of G_{th} on the pump wavelength and the interaction length in the transient regime has not been observed experimentally or treated theoretically.

In this work, we present a new method to measure the SBS threshold, which is simple, accurate, and is not confined by the medium characteristics. By this method, we theoretically and experimentally investigate the dependences of the values of G_{th} on the pump wavelength and the interaction length.

10.2. Measurement Principle and Threshold Characteristics for SBS

We assume a pump wave $\vec{E}_{\text{P}}(z, t)$, propagating in the $+z$ direction, a backward Stokes wave, $\vec{E}_{\text{S}}(z, t)$, and a forward acoustic wave, $\vec{\rho}\,(z, t)$, within the SBS medium. The three-wave coupled wave equations to describe transient SBS including its spontaneous initiation from noise are written as (Gaeta & Boyd, 1991)

$$\frac{\partial E_{\text{P}}}{\partial z} + \frac{n}{c}\frac{\partial E_{\text{P}}}{\partial t} = \mathrm{i}g_1\rho E_{\text{S}} - \frac{1}{2}\alpha E_{\text{P}}, \tag{1a}$$

$$\frac{\partial E_{\text{S}}}{\partial z} + \frac{n}{c}\frac{\partial E_{\text{S}}}{\partial t} = \mathrm{i}g_1\rho^* E_{\text{P}} + \frac{1}{2}\alpha E_{\text{S}}, \tag{1b}$$

$$\frac{\partial \rho}{\partial t} + \frac{1}{2}\Gamma\rho = \mathrm{i}g_2\rho E_{\text{P}}E_{\text{S}}^* + f, \tag{1c}$$

where E_{P}, E_{S}, and ρ are the amplitudes of the pump, the Stokes, and the acoustic waves, respectively; n is the refractive index of the medium; g_1 and g_2 are the coupling coefficients; α is the absorption coefficient; $\Gamma = 1/\tau_0$ denotes the phonon decay rate, where τ_0 is the phonon lifetime. Also, f represents the Langevin noise source that describes the thermal excitation of acoustic waves and leads to the initiation of the SBS process. It is spatially and temporally δ-correlated Gaussian random process with zero mean:

$$\langle f(z, t)f^*(z', t')\rangle = Q\delta(z - z')\delta(t - t'), \tag{2}$$

where

$$Q = \frac{2kT\rho_0\Gamma}{V^2A}, \tag{3}$$

characterizes the noise intensity. ρ and V are the density and sound speed of the medium, respectively; A is the cross-sectional area of the interaction region. Directly, integrating the ρ phonon from Eq. (1c), substituting it into Eqs. (1a) and (1b), and using the transforms $g = 4g_1\ g_2/\Gamma\cdot 8\pi/nc$, and $A_{P,S} = \sqrt{nc/8\pi}\,E_{P,S}$ we have

$$\left(\frac{\partial}{\partial z} + \frac{n}{c}\frac{\partial}{\partial t}\right)A_{\text{P}} = -\frac{g\Gamma}{4}A_{\text{S}}\int_0^t A_{\text{P}}A_{\text{S}}^*\exp\left[-\frac{\Gamma}{2}(t-\tau)\right]d\tau + \mathrm{i}g_1A_{\text{S}}\int_0^t f\exp\left[-\frac{\Gamma}{2}(t-\tau)\right]d\tau - \frac{1}{2}\alpha A_{\text{P}}, \tag{4a}$$

$$\left(\frac{\partial}{\partial z} - \frac{n}{c}\frac{\partial}{\partial t}\right)A_{\text{S}} = -\frac{g\Gamma}{4}A_{\text{P}}\int_0^t A_{\text{P}}^*A_{\text{S}}\exp\left[-\frac{\Gamma}{2}(t-\tau)\right]\mathrm{d}\tau - \mathrm{i}g_1A_P\int_0^t f^*\exp\left[-\frac{\Gamma}{2}(t-\tau)\right]\mathrm{d}\tau + \frac{1}{2}\alpha A_{\text{S}}, \tag{4b}$$

where g is the SBS gain coefficient. The beam intensity is defined as $I_{\text{P,S}} = |A_{\text{P,S}}|^2$. By implicit finite difference in time and backward difference in space, Eq. (4) can be numerically solved.

We consider an incident pump pulse of Gaussian temporal shape, which is input at $z = 0$, and output at $z = L$ (L is the cell length). The boundary conditions are given as: $A_P(0, t) = A_{\text{P0}}\ \exp\ \{-2\ \ln\ 2[(t - t_0)/t_{\text{P}}]^2\}$, $A_{\text{S}}(L,\ t) = 0$. The pump output energy can be expressed as $\int_0^\infty |A_{\text{P}}(L,\ t)|^2dt$. The system's exponential gain is defined as $G = gI_{\text{P0}}L_{\text{eff}}$, where $I_{\text{P0}} = |A_{\text{P0}}|^2$ is the peak intensity of the incident

https://doi.org/10.1017/S0263034611000644 Published online by Cambridge University Press

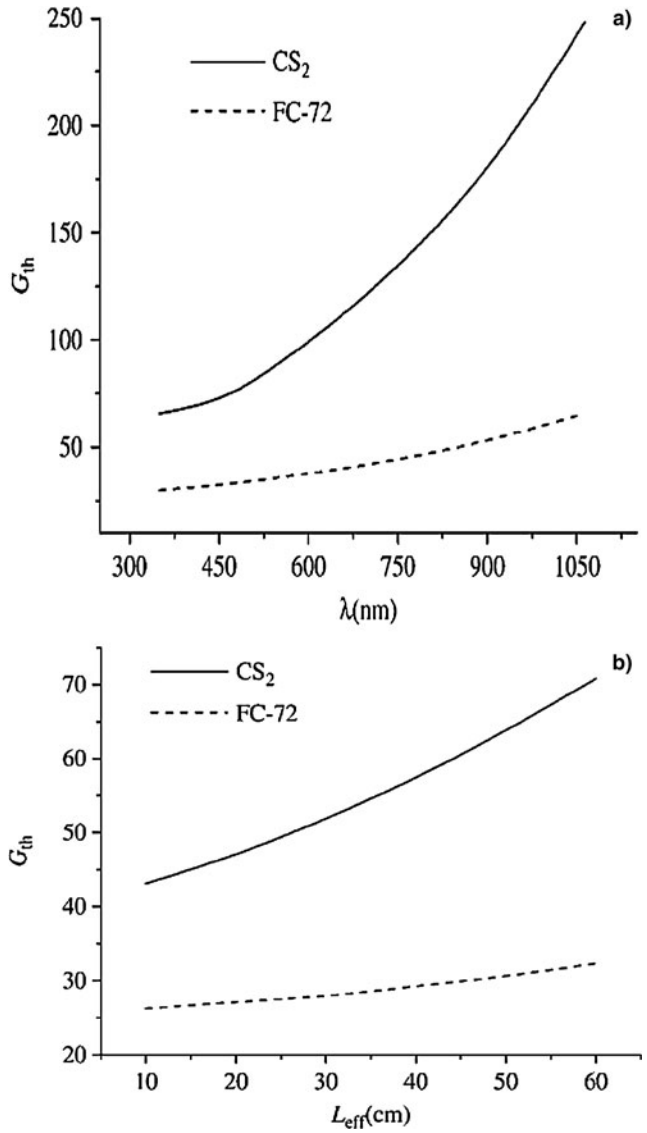

Fig. 57. Dependences of G_{th} in CS_2 and FC-72 on (**a**) λ for $L_{eff} = 60$ cm, (**b**) L_{eff} for λ = 532 nm.

pump pulse. Obviously, for given g and L_{eff}, the value of G is changed with I_{P0}. Figure 57 shows that the dependence of the output energy of the pump on the exponential gain G. In the calculation, the following parameters are used: the wavelength of the incident pump pulse is 532 nm with an 8 ns full width at half maximum, the interaction length is 60 cm. FC-72 is chosen as the SBS medium, its parameters are shown in Table 6. The simulation parameters are closely matched to those that are used for experiments.

We see that when the value of G is low, the SBS does not take place, and hence the line AB in Figure 56 shows a linear increase of output energy with G. After the pump intensity exceeds the SBS threshold, the energy quickly transfers from the pump to the Stokes. Consequently, the increase rate of output energy slows down (i.e., line CD), leading to an optical limiting effect. Line CD represents a nonlinear increase process. However, according to Figure 56, it can be considered as an approximately linear change before the gain saturation occurs. Thus, we perform linear fits for lines AB and CD. The value of G corresponding to the intersection point of two straight lines is defined as G_{th}. At this time, the SBS reflectivity is about 2.5%, which agrees with the criterion for threshold generally accepted.

By using the model and method mentioned above, we obtain the values of G_{th} for different wavelengths, λ, and interaction lengths, L_{eff}, using CS_2 and FC-72 as the SBS media. Their main medium parameters are listed in Table 6. Figure 58a shows the dependence of G_{th} on λ. According to the literature (Damzen, *et al.*, 1987), the phonon lifetime of the medium, τ_0, is proportional to λ^2. Therefore, with the increase of λ, the ratio of the pump pulse width to the phonon lifetime, t_P/τ_0, decreases, leading to the stronger transient behavior (Bel'dyugin *et al.*, 2005; Maier & Renner, 1971). This causes the increase of the values of I_{th} and G_{th}. On the other hand, we can see from Eq. (3) that the noise intensity, Q, is proportional to Γ, i.e., $Q \propto 1/\tau_0 \cdot G_{th}$ will be raised because of the reduced Q with increasing λ. Then, we choose λ as 532 nm and study the dependence of G_{th} on L_{eff}, as shown is in Figure 58b. At this time, t_P/τ_0 is 5 and 27 for CS_2 and FC-72, respectively. Strictly speaking, the transient SBS process will occur in these two media (Bel'dyugin *et al.*, 2005). In the transient regime, the longer L_{eff} for the same G means the smaller pump intensity, which results in a slower build up of the sound wave and hence a smaller Stokes signal intensity. Therefore, the larger G_{th} is needed to attain the SBS threshold. It can also be seen from Figure 58 that the values of G_{th} are very different for various media, and are larger than that of steady state (20–25 (Boyd *et al.*, 1990)). This also indicates that G_{th} increases as t_P/τ_0 decreases due to the transient effect.

Table 6. *The parameters of some SBS media*

Medium	n	ρ(g/cm^3)	g(cm/GW)	τ_0(ns) λ = 532 nm	τ_0(ns) λ = 1064 nm	α(cm^{-1})	V(m/s)
CS_2	1.63	1.26	68	1.59[a]	6.4	0.0038	1250
FC-72	1.25	1.68	6	0.29[a]	1.2	10^{-4}	512

[a]The parameters are calculated according to the equation given by Erokhin *et al.* (1986) and the results at 1064 nm (Erokhin *et al.*, 1986; Yoshida *et al.*, 1997); Others are quoted from Erokhin *et al.* (1986) and Yoshida *et al.* (1997).

https://doi.org/10.1017/S0263034611000644 Published online by Cambridge University Press

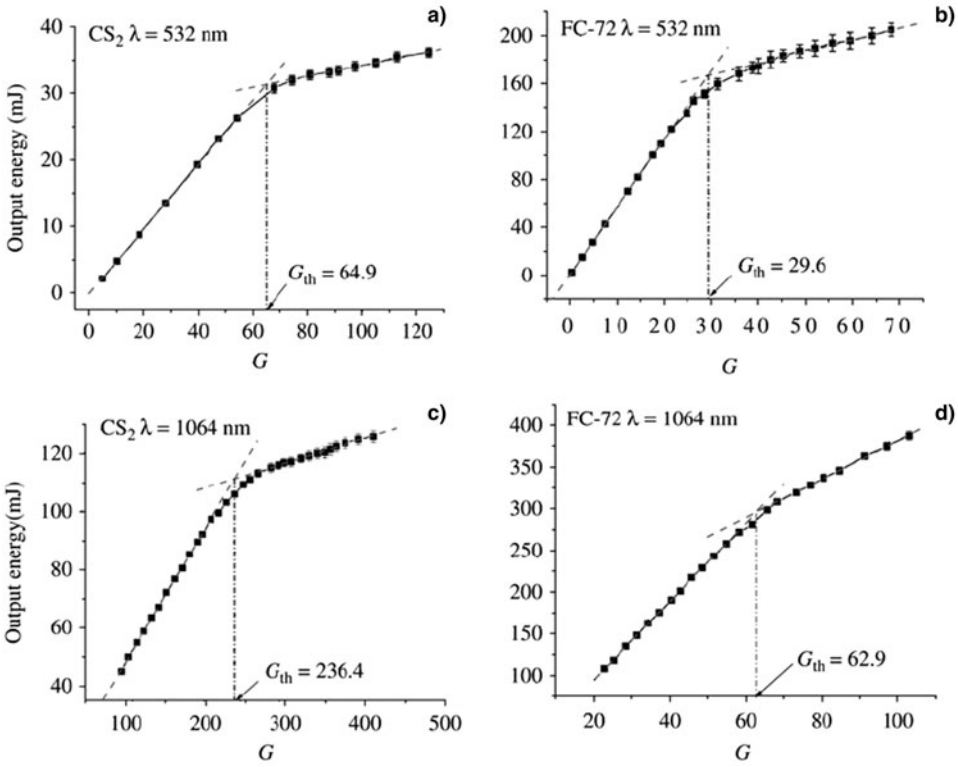

Fig. 58. Output energy versus G in (**a**) CS_2 at λ = 532 nm, (**b**) FC-72 at λ = 532 nm, (**c**) CS_2 at λ = 1064 nm, and (**d**) FC-72 at l.1064 nm.

10.3. Experimental Results and Discussions

Experimental setup is shown in Figure 59. The laser used is an injection-seeded, Q-switched, pulsed Nd:YAG laser (Continuum Powerlite Precision II 9010) with a line width of 90 MHz and repetition rate of 10 Hz. The output wavelength of the laser is 1064 nm and 532 nm (when the double frequency crystal is inserted), the pulse width is 7–8 ns, and the beam diameter is 8 mm. The pump energy is continuously varied by means of an attenuator, which consisted of a rotatable half-wave plate (λ/2) and a polarizer (P). A quarter-wave plate (λ/4), together with the polarizer P, forms a light isolator, preventing backward SBS light from entering YAG oscillator. A small fraction of the laser energy separated by the beam splitter (BS) and the output energy of the pump is measured by the PE50BB energy detectors (Ophir Optics), ED_1 and ED_2, respectively.

CS_2 and FC-72 are chosen as SBS media. It has been theoretically and experimentally validated that the scattering occurred in these media could only be SBS if the pulse energy of the laser is controlled in certain range. Other stimulated scatterings can be excluded (Bai *et al.*, 2008; Gao *et al.*, 2008; Daree & Kaiser, 1971; Sen & Sen, 1986). SBS generally takes place in the free gain length (FGL) determined by the pulse width of the pump beam (Bai *et al.*, 2008). In our experiments, the FGLs in CS_2 and FC-72 are about 75 cm and 95 cm, respectively. If the cell length, $L \geq$ FGL, L_{eff} = FGL, or else, $L_{eff} = L$. Figure 60 shows that the output energy versus G at 532 nm and 1064 nm. The cell lengths are all 60 cm, which are all less than the FGLs. Therefore, L_{eff} = 60 cm. To determine G_{th}, the measured results below and above the SBS threshold are fitted into two straight

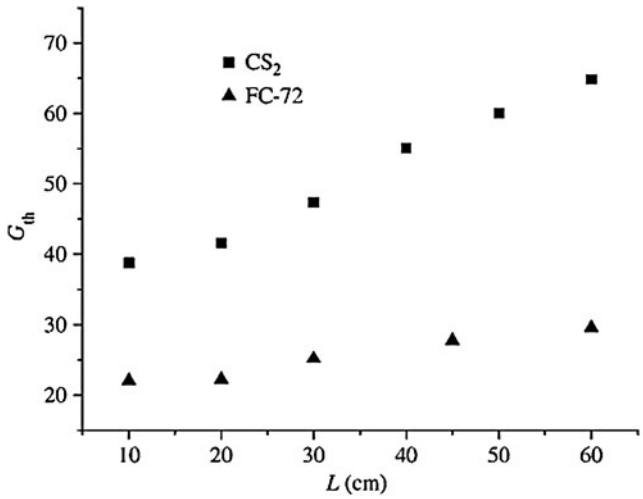

Fig. 59. G_{th} versus L.

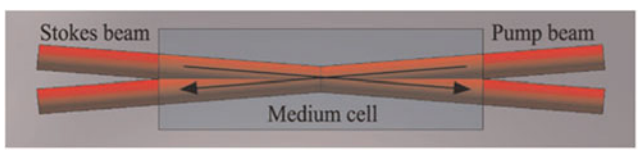

Fig. 60. (Color online) Model of non-collinear Brillouin amplification.

https://doi.org/10.1017/S0263034611000644 Published online by Cambridge University Press

dash lines. The vertical dash-dot lines denote intersection points that correspond to G_{th}. The measured and theoretical G_{th} and I_{th} are summarized in Table 7. It can be seen that the values of G_{th} and I_{th} increase as λ. The reasons for this trend are discussed in the theoretical analysis.

Figure 59 shows the dependence of G_{th} in CS_2 and FC-72 on the cell length, L. In the experiment, L are all less than FGLs, so $L_{eff} = L$. The pump wavelength is 532 nm. It can be seen that G_{th} increases as L. This result is different from that for steady-state SBS (Kovale & Harrison, 2007). The change tendencies of the experimental results are in agreement with those of the theoretical predictions in Figure 58b.

However, as seen from Table 7, there are the discrepancies between the experimental and theoretical values. The reasons for the errors may be summarized as follows. First, some main medium parameters such as g and τ_0 in the calculation are not completely consistent with those in the experiment, especially for the case of $\lambda = 532$ nm. Most of data in Table 6 quoted from the literatures are experimentally obtained at 1064 nm; whereas the parameters at 532 nm are calculated according to the equation given by Erokhin *et al.* (1986) and the results at 1064 nm. Therefore, the relative measurement errors at 532 nm (about 8%) are larger than those at 1064 nm (<5%). Second, we find that the absorption coefficient has greater influence on the calculated results. In the theoretical calculation, we introduce the linear absorption coefficients without considering the nonlinear absorption that may occur in the media. Finally, one-dimensional coupled wave equations as shown in Eq. (1) approximately describe the SBS characteristics. If more accurate, Gaussian spatial and spectral distribution of the pump beam should be taken into account.

10.4. Conclusion

Based on the output energy characteristic of SBS optical limiting, the SBS threshold or its exponential gain can be determined by the intersection point of linear-fitting lines of the output energy below and above the threshold. This method is suitable for various SBS media with the advantages of simple operation and high accuracy. We experimentally and theoretically investigate the dependences of the threshold value of exponential gain, G_{th}, on the pump wavelength and the interaction length. The results indicate that G_{th} increases with the pump wavelength and the interaction length. For Nd:YAG laser commonly used with a nanosecond-order pulse width, the values of G_{th} for various media are very different. Unlike the case of steady-state SBS, transient SBS has no similar criterion for estimating SBS threshold. Therefore, in some applications such as Brillouin amplification, SBS threshold should be estimated according to the medium properties, length, and the wavelength in order to determine the optimum working point of the amplifier.

ACKNOWLEDGMENTS

This work is supported by the National Natural Science Foundation of China (Grant No. 60878005, 60778019) and the Program of Excellent Team in Harbin Institute of Technology.

11. INVESTIGATION ON EFFICIENCY OF NON-COLLINEAR SERIAL LASER BEAM COMBINATION BASED ON BRILLOUIN AMPLIFICATION (Y.L. Wang, Z.W. Lu, S.Y. Wang, Z.X. Zheng, W.M. He, and D.Y. Lin)

11.1. Introduction

Solid state lasers of high repetition rate, high power, and large energy may be widely applied in the domains of military, scientific research, and industry, such as inertial confinement fusion (Hoffmann *et al.*, 2005; Miley *et al.*, 2005), space optical communication and material processing (Thareja & Sharma, 2006; Veiko *et al.*, 2006). However, because of the limitation of crystal growth technology, heat distortion, and damage threshold, the output of a single-laser apparatus is restricted.

The laser beam combination is a technology that combines several laser beams with low power and energy to produce a high energy and high power laser output (Kong *et al.*, 2005*c*). Existing methods usually use a nonlinear optics phase conjugation approach to combine solid-state pulse lasers. Stimulated Brillouin scattering (SBS) is a very important way in these methods (Kong *et al.*, 1997; Shuangyi *et al.*, 2007). The SBS parallel beam combination is composed of the overlap coupling beam combination (Basov *et al.*, 1980), the back-seeding beam combination (Loree *et al.*, 1987), and the self-phase control beam combination (Kong *et al.*, 2005*b*; Lee *et al.*, 2005*b*). The overlap coupling beam combination and the back-seeding beam combination are limited by the low load of the system and the poor backward reflectivity because several laser pulses are focused into one medium cell. In order to overcome these disadvantages, Kong *et al.* (2005*b*) proposed the self-phase control SBS parallel beam combination. In this new scheme, each laser pulse

Table 7. *Comparison of measured and theoretical threshold exponential gain* G_{th} *and the threshold value* I_{th} *for SBS*

Medium	Λ = 532 nm				Λ = 1064 nm			
	G_{th}^{exp}	G_{th}^{theor}	I_{th}^{exp}(MW/cm^2)	I_{th}^{theor}(MW/cm^2)	G_{th}^{exp}	G_{th}^{theor}	I_{th}^{exp}(MW/cm^2)	I_{th}^{theor}(MW/cm^2)
CS_2	64.9	70.8	15.9	17.3	236.4	248.2	57.9	60.8
FC-72	29.6	32.3	82.2	89.7	62.9	65.8	174.7	182.8

https://doi.org/10.1017/S0263034611000644 Published online by Cambridge University Press

has an independent medium cell to realize phase conjugation, so that the system load is separated into many cells and is a simple optical arrangement (Kong *et al.*, 2008). Their study indicated that the piston error between pump beams was the key factor of the beam combination (Kong *et al.*, 2007*b*).

The serial laser beam combination based on Brillouin amplification uses several pump beams to amplify one seed pulse so that the phase is matched during the amplifying process. In this beam combination technology, the pump pulses and the seed pulse must be collinear to achieve the highest Brillouin amplifying efficiency. However, with increasing the number of pump beams, the beam combination structure becomes more and more complex because of a great amount of usage of polarizer and wave plates that are necessary to beam input and output in this system. Thus, in this work, we propose a non-collinear scheme to simplify the structure of the beam combination setup. Unlike the collinear scheme, there is an angle between the Stokes beam and the pump beam for the non-collinear scheme in the SBS cell. The pump pulse and the Stokes pulse can be injected into the amplification cell directly, and the amplified Stokes pulse is also output from the cell directly. So the polarizer and wave plates are not needed in the non-collinear scheme. Removing the wave plates and polarizer has significantly simplified the non-collinear scheme. With the non-collinear scheme, the key problem to be solved is achievement of high efficiency of the beam combination. In this article, the amplifying efficiency of the non-collinear scheme is investigated and discussed.

11.2. Theoretical Simulation

The geometry of non-collinear Brillouin amplification is shown in Figure 60, the angle between the Stokes beam and the pump beam is β. In this experiment, the pulse is a cylindrical beam so the intersection volume of the two beams is defined as the overlap volume *V*. The effective interaction length L_{eff} is defined by the result of *V* divided by the cross section area *S*. The beam diameter is given by *d*. So the effective interaction length L_{eff} in the medium cell is defined as

$$L_{\text{eff}} = V/S = \begin{cases} \dfrac{4}{3\pi}\dfrac{d}{\cos\alpha\sin\alpha} & (L_m \le L), \\ (V1+V2+V3+V4)/S & (L_m > L) \end{cases} \tag{1}$$

where

$$S = \pi d^2/4,\ V1 = \frac{d^3}{3\sin\alpha\cos\alpha}$$

$$V2 = \left(\frac{\pi}{4\cos\alpha} - \frac{\arcsin(L\sin\alpha/d)}{2\cos\alpha}\right)d^2L$$

$$V3 = \frac{\sin^2\alpha}{6\cos\alpha}\sqrt{\left[\left(\frac{d}{\sin\alpha}\right)^2 - L^2\right]^3}$$

$$V4 = -\frac{d^2}{2\cos\alpha}\sqrt{\left(\frac{d}{\sin\alpha}\right)^2 - L^2},\quad \alpha = \beta/2$$

L is the length of the medium cell, and L_m is the length of the intersection domain. In the one-dimension transient condition, the non-collinear Brillouin amplification process is seen as a wave vector mismatch process. The wave vector direction is the pulse propagation direction. Thus, the mismatch angle is just the angle of the two beams. Finally, the numerical model of the non-collinear amplification is shown below (Shuangyi *et al.*, 2007).

$$\left(\frac{n}{c}\frac{\partial}{\partial t} - \frac{\partial}{\partial z}\right)E_P = \frac{g\Gamma}{2}E_S\int_0^t E_S^*E_P\exp(-\Gamma(t-\tau))d\tau + \frac{1}{2}\alpha E_P \tag{2a}$$

$$\left(\frac{\partial}{\partial z} + \frac{n}{c}\frac{\partial}{\partial t}\right)E_S = \frac{g\Gamma}{2}E_P\int_0^t E_P^*E_S\exp(-\Gamma(t-\tau))d\tau - \frac{1}{2}\alpha E_S \tag{2b}$$

$$g = g_{\max}\frac{(\Gamma/v_a)^2}{(\Gamma/v_a)^2 + 4[(4\pi/\lambda)(1-(\cos(\beta/2)))]^2} \tag{2c}$$

$$L_{\text{eff}} = V/S = \begin{cases} \dfrac{4}{3\pi}\dfrac{d}{\cos\alpha\sin\alpha} & (L_m \le L) \\ (V1+V2+V3+V4)/S & (L_m > L) \end{cases} \tag{2d}$$

Where $g_{\max}$ is the medium gain coefficient. E_P and E_S are the pump and Stokes fields, respectively.

Using this model, the non-collinear Brillouin amplification process is simulated. FC-72 is chosen as the SBS medium and its parameters are given by: gain coefficient $g_{\max} = 6.0$ cm/GW, absorption coefficient $\alpha = 10^{-5}\text{cm}^{-1}$, medium refractive index $n = 1.25$, the Gaussian laser pulse widths are both 10 ns (full width at half maximum). As shown by Figure 60, the change of the angle will change the intersection area in the medium cell greatly, and therefore the effective interaction length changes too. Assuming that the cell length is 20 cm, the result according to Eq. (2) is shown in Figure 61. The angle impacts greatly on the effective interaction length. When the angle is nearly 90 mrad, the

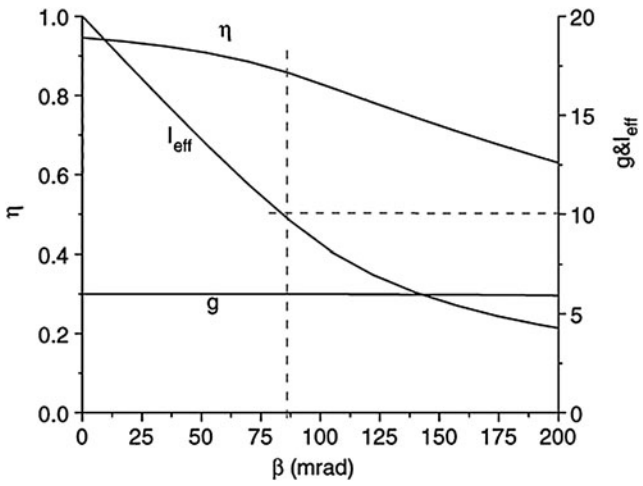

Fig. 61. Influence of cross-angle various on Brillouin amplification.

https://doi.org/10.1017/S0263034611000644 Published online by Cambridge University Press

effective length reduces to half of the cell length. In other words, the cell length becomes short. But the change of the gain coefficient can be ignored. In conclusion, it is the effective interaction length that impacts the energy amplifying efficiency, but not the gain coefficient for this scheme. Fortunately, short cell length is good in the strong signal Brillouin amplification process. So the scheme is efficient in achieving high efficiency of amplification when the angle is limited within 200 mrad.

11.3. Analysis and Discussion

According to the analysis above, the change of angle between the pump and the Stokes will directly influence the efficiency.

In the experiment, the energies of the Stokes pulse and the pump pulse are both 52 mJ, and the width of the pulse is 6 ns. Results of Brillouin amplification in different cross-angles can be obtained by adjusting the optical path gradually. The incident angle is defined as β_{air} and the refractive angle is defined as β_{medium}. Results from the experiment are shown in Figure 62. In the figure, the abscissa above represents the cross-angle between the pump beam and the Stokes beam outside the medium cell, while the abscissa below represents the cross-angle in medium cell. The influence of the two angles on the efficiencies is investigated by experiment, and the results are shown in Figure 62. As shown in the figure, on the condition of β_{air} varying from 3° to 10° energy extraction efficiency decreases along with the increasing of β_{air}. These experimental results are consistent with theoretical results.

As discussed above, non-collinear Brillouin amplification is efficient. With the simplest optical arrangement, two noncollinear laser beams are of great significance to the beam combination. On the one hand, the research can be helpful to seek the feasibility of Stokes beam amplification by multiple pump beams. On the other hand, it can also provide technical support on design of serial laser beam combination.

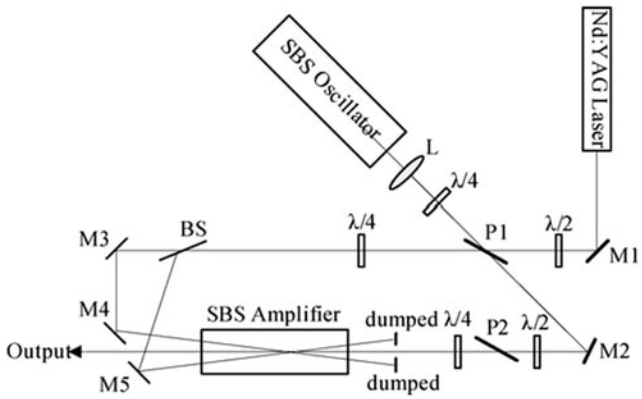

Fig. 63. Experimental setup of two-beam combination.

Based on research of signal pump beam amplification, experimental setup of the two-beam combination is shown in Figure 63. A Nd:YAGlaser with pulse duration of about10 ns is split into three lasers beams. One of them is used to the Stocks beam; the others are used as pump beams to combine into one.

The pump beam is divided by beam splitter into two beams: a reflected beam is reflected by mirror M5 and a transmitted beam is reflected by mirrors M3 and M4. The two pump beams are both reflected into the medium cell to amplify the Stokes beam together and the energies of the two beams are combined to one Stokes seed. The cross angles between pump beams and the Stokes beam are both 5° (approximately 87 mrad). Length of the medium cell is 20 cm and the medium material is FC-72. Experimental results are shown in Figure 64.

In order to characterize the efficiency of beam combination, two efficiencies are defined as (1) efficiency of beam combination $\eta_1 = E_{SA}/(E_S + E_P)$, and (2) depleted

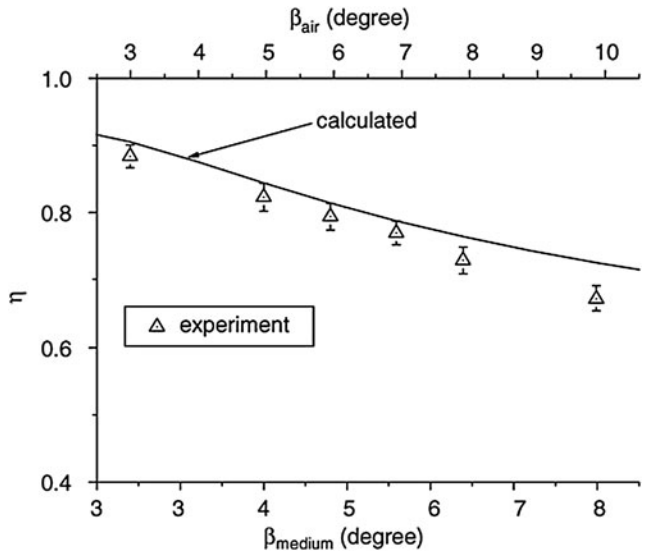

Fig. 62. Influence of various cross-angle on the Brillouin amplification.

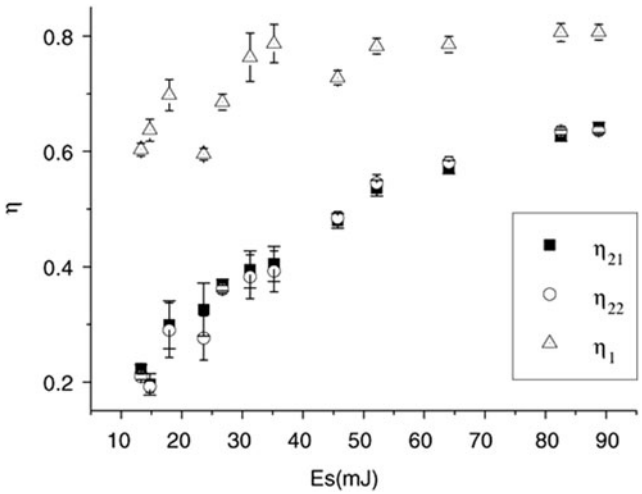

Fig. 64. Experimental results of two-beam combination based on noncollinear Brillouin amplification.

https://doi.org/10.1017/S0263034611000644 Published online by Cambridge University Press

ratio of pump energy $\eta_2 = (E_P - E_{PR})/E_P$. Where E_{SA} and E_{PR} are the energy of the amplified Stokes beam and the residual energy of the pump beam after amplifying, respectively. E_S and E_P are the energies of the Stokes and the pump, respectively.

In Figure 64, η_{21} and η_{22} represents the depleted ratio of the two pump beams, respectively. As is shown in this figure, total energy extraction efficiency increases with the increasing of Stokes energy, and the efficiency of beam combination also increases. When the two pump beams are 47.1 mJ and 41.5 mJ, respectively, and Stokes beam is up to 88.0 mJ, a beam combination efficiency of 80.7% is achieved. Furthermore, a higher efficiency of beam combination is achieved with a higher energy of the Stokes beam, which results in a stabilization of the efficiency. The result demonstrates the efficiency of a non-collinear beam combination and is useful to the multi-beam combination with a strong Stokes seed (Ostermeyer *et al.*, 2008).

11.4. Design and Discussion of Multi-Beam Combination

According to the discussion above, we know that the non-collinear beam combination has a higher efficiency compared with the linear beam combination. This provides a method for more effective and simpler laser beam combination scheme. In this work, a 20-beam combination is designed and the layout is shown in Figure 65. Here, the length of the medium cell is 10 cm, diameters of pump beam P1–P3, P4–P7, P8–P13, P14–P19 are 3 cm, 4 cm, 5 cm, and 6 cm, respectively. Using a non-collinear scheme, the 20-beam combination could be no larger than 150×150 cm^2. In order to get an effective combination, a regulation can be observed that the total gain of the system

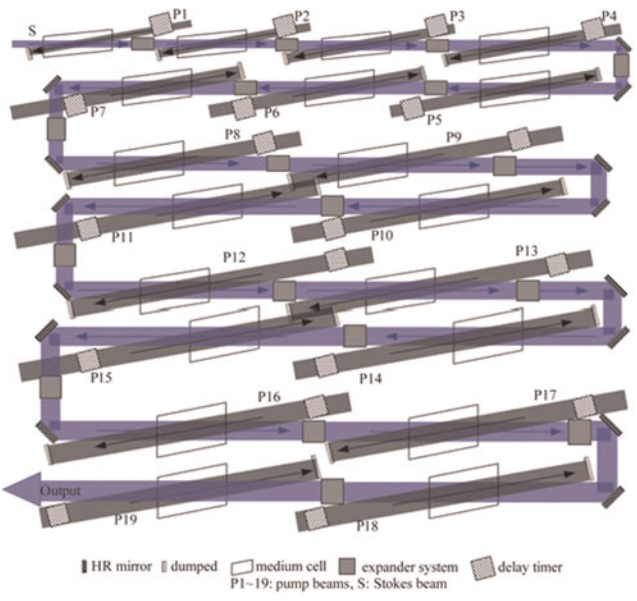

Fig. 65. (Color online) Layout of a 20-beam combination with 10-cm-cell-length.

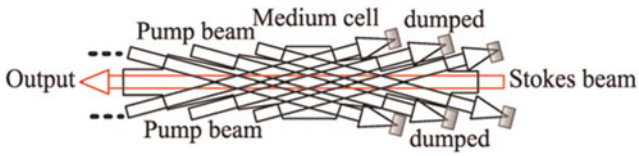

Fig. 66. (Color online) Scheme design of a serial beam combination based on multiple pump beams with non-collinear Brillouin amplification.

is near but not more than the Brillouin threshold. The output energy of 13.2 J will be expected by this 20-beam combination scheme with the energy of 818 mJ for every pump pulse. The efficiency of this beam combination is approximately 81%.

The layout shown in Figure 65 is still a complex application, even though the non-collinear scheme is simple. Therefore, to design such an application requires a special geometry. The following is a proposed design for a multi-beam combination based on the non-collinear scheme. The geometry is shown in Figure 66. In this scheme, multiple pump beams are injected into the same medium cell simultaneously, and the Stokes seed is amplified by all the pumps. Two aspects of this scheme are useful to the multiple beams combination: one is that higher pump energy is achieved by multiple pump beams and not a pump beam injected into single cell, thus higher Stokes energy is obtained. The other is that this layout is more compact and simple. What is more, multiple pump beams interacting with the Stokes beam at the same time also lessen time delay. To get a more effective combination, every stage of the non-collinear beam combination should satisfy the regulation that the total gain of the system is near but not more than the Brillouin threshold.

11.5. Conclusion

The non-collinear scheme of serial laser beam combination based on Brillouin amplification is presented. And the efficiency of beam combination is investigated. The results show that when the interaction length between the pump and the Stokes is long enough, a high efficiency can be achieved with the angle between the pump and the Stokes limited in 200 mrad.

The two-beam combination scheme is then studied. It is found that the energy extraction efficiency increased with the increasing of Stokes beam energy, and the combination efficiency increased too. A high beam combination efficiency of 80.7% was obtained in experiment with two pump energies of 47.1 mJ and 41.5 mJ and Stokes energy of 88.0 mJ. The experimental result is consistent with the theoretical analysis.

A 20-beam combination is designed with the parameters of a medium cell with length of 10 cm, laser beam cross angle of 10°, pulse duration of 10 ns and the beam diameter of 1 cm. An output energy of 13.2 J will be expected, with an efficiency as high as 81%. The results show that the scheme

https://doi.org/10.1017/S0263034611000644 Published online by Cambridge University Press

of beam combination based on non-collinear construction is suitable to apply when the energy of a single laser beam is larger, since the larger size beam is needed in a high energy laser system. In order to simplify the complex construction of the twenty-beam combination, a special geometry is designed which is suitable in all the cases of a multiple-beam combination.

ACKNOWLEDGMENTS

This work is supported by the National Natural Science Foundation of China (Grant No. 60878005), the National High Technology Development Program of China and the Program of Excellent Team in Harbin Institute of Technology, and the China Postdoctoral Science Foundation (Grant No. 20090450966).

12. INVESTIGATION ON EFFECT OF MEDIUM TEMPERATURE UPON SBS AND SBS OPTICAL LIMITING (W.L.J. Hasi, X.Y. Guo, H.H. Lu, M.L. Fu, S. Gong, X.Z. Geng, Z.W. Lu, D.Y. Lin, and W.M. He)

12.1. Introduction

Stimulated Brillouin scattering (SBS) has been regarded as an effective way to recover beam front and can be exploited to improve beam quality. The SBS phase conjugation exhibits several advantages in terms of small frequency shift, simple configuration, high fidelity, and high energy reflectivity. Therefore, it has been a focus of theoretical and experimental investigation during the past several decades (Kong *et al.*, 2007*b*; Yoshida *et al.*, 2007; Ostermeyer *et al.*, 2008; Bai *et al.*, 2008; Grofts *et al.*, 1991; Wang *et al.*, 2007, 2009*a*; Hasi *et al.*, 2007). A great deal of research has demonstrated medium is a crucial factor for improving the SBS performance (Yoshida *et al.*, 1997; Hasi *et al.*, 2008*a*; Park *et al.*, 2006; Chalus & Diels, 2007; Gong *et al.*, 2009). In the previous investigations, SBS phase conjugation experiments are usually carried out in room temperature and the effect induced by temperature change is seldom considered. In reality, the medium temperature may be changed due to the absorption of pump light with a high power and repetition rate. Therefore, investigation on the effect of medium temperature upon SBS and SBS optical limiting is a meaningful issue (Hasi *et al.*, 2008*b*, 2008*c*).

In this work, the effect of medium temperature upon characteristic of SBS and SBS optical limiting is investigated. The physical mechanism behind is analyzed theoretically and experimentally verified in Continuum's Nd:YAG Q-switched laser system using FC-72 as the SBS medium. The temperature affects the electro-strictive coefficient, refractive index, density and acoustic velocity of the medium weakly. In contrast, the kinematic viscosity, which is inversely proportional to the temperature, is related to gain coefficient and phonon lifetime, and thus greatly affects the SBS characteristics. Therefore, in the low temperature, the kinematic viscosity is usually high, which can lead to a small gain coefficient, and a short phonon lifetime. Therefore, the SBS characteristic can be changed by controlling the temperature to a great extent.

12.2. Theory

The gain coefficient of medium can be expressed by (Park *et al.*, 2006; Erokhin *et al.*, 1986; Pohl & Kaiser, 1970),

$$g = \frac{4\pi^2\gamma^2\tau}{ncv\rho\lambda^2}, \tag{1}$$

where g is the gain coefficient, n is the refractive index, γ is the electrostriction coefficient, which is related to n by $\gamma = (n^2-1)(n^2+2)/3$, τ is the phonon lifetime, c is the light velocity in the vacuum, v is the acoustic velocity, ρ is the density, and λ is the wavelength of incident light.

The phonon lifetime τ of medium can be expressed by (Park *et al.*, 2006; Erokhin *et al.*, 1986)

$$\tau = \frac{\lambda^2}{4\pi^2\eta}, \tag{2}$$

where η denotes the kinematic viscosity. Eq. (2) shows that when the phonon lifetime τ is inversely proportional to the kinematic viscosity η.

Substituting Eq. (2) into Eq. (1), the gain coefficient g can be related to kinematic viscosity η by:

$$g = \frac{\gamma^2}{ncv\rho\eta}. \tag{3}$$

Eq. (3) shows that the gain coefficient is also inversely proportional to kinematic viscosity.

The temperature change has a little effect on the refractive index, density, and acoustic velocity. However, for the kinematic viscosity, it varies greatly with the temperature (Weaver, 2009; Patent (IPC8 Class: AF21V2900FI); Lagemann *et al.*, 1948; Grassi & Testi, 2008), as shown in Figure 67.

Table 8 lists the density and kinematic viscosity of SBS medium perfluoro-compound at 25°C and −54°C, respectively. The density of FC-72 increases from 1.68 g/cm^3 at 25°C to 1.90 g/cm^3 at −54°C, and the relative change is only 13%; however, the kinematic viscosity increases from 0.4 cSt at 25°C to 1.9 cSt at −54°C.

Since the gain coefficient and phonon lifetime are both related to the kinematic viscosity, the temperature change will greatly affect the two parameters. In the low temperature, the gain coefficient and phonon lifetime are small. Increasing the temperature will lead to the increase in the gain coefficient and phonon lifetime.

12.3. Experiment

The experimental setup is shown in Figure 68. Continuum's Nd: YAG Q-switched laser outputs single mode *s*-polarized

https://doi.org/10.1017/S0263034611000644 Published online by Cambridge University Press

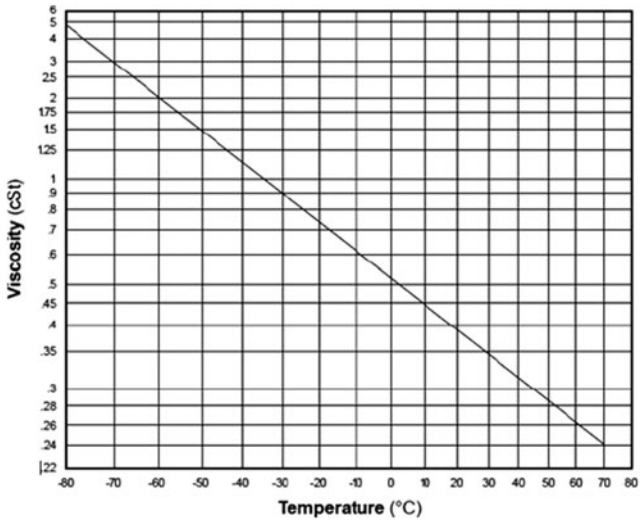

Fig. 67. The kinematic viscosity of FC-72 versus medium temperature.

Table 8. *The density and kinematic viscosity of SBS medium at different temperature*

Medium		FC-72	FC-87	FC-77	FC-84
Density (g/cm^3)	25°C	1.68	1.63	1.78	1.73
	−54°C	1.90	1.84	1.97	1.93
Kinematic viscosity (cSt)	25°C	0.4	0.4	0.8	0.55
	−54°C	1.9	1.1	6.9	4.0

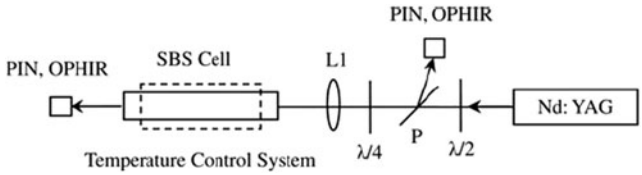

Fig. 68. Experimental setup.

light with line-width 90 MHz, which becomes *p*-polarized after passing the 1/2 wave plate, and then circular polarized after passing the 1/4 wave plate. The SBS system comprises a generator cell and a focus lens L1 ($f =$ 30 cm). The pump light is focused into a generator cell to produce Stokes light. Polarizer P together with a 1/4 wave plate forms a light isolator, preventing the backward SBS light from entering YAG oscillator. The Stokes light becomes *s*-polarized after passing the 1/4 wave plate, and is reflected by polarizer P. The pump energy can be adjusted through a 1/2 wave plate. The energy of pump pulse, Stokes pulse, and transmitted pulse are measured with energy meter OPHIR company. The pulse shape is detected with PIN photodiode, and recorded with digital oscilloscope TDS684A.

The output wavelength of Continuum's Nd: YAG Q-switched laser is 1064 nm, with a repetition rate of 1 Hz, pulse width 8 ns, and divergence angle 0.45 mrad. FC-72 is adopted as the SBS medium. The medium temperature is altered by resistance heating films and semiconductor refrigerating chips. Table 9 lists the parameters of some SBS media. In order to eliminate the water droplet formed on the cell window plate due to the temperature difference between air and medium at low temperature, SBS cell with double window plates is designed, as shown in Figure 69. The inter-space between the two window plates is vacuum pumped; therefore no water droplet can be formed while the light can propagate freely.

Figure 70 provides the dependence of SBS energy reflectivity on the medium temperature for fixed pump energy. The reflectivity scales is almost linearly with the temperature. This is because small kinematic viscosity due to a high temperature can lead to a large gain coefficient, thus enhancing the energy coupling efficiency between the pump and Stokes (Boyd & Rzazewski, 1990). Therefore, a proper choose of temperature increase can lead to improved SBS energy reflectivity. For the output energy of SBS optical limiting, it will turn high at a low temperature (Hasi *et al.*, 2009*a*).

Figure 71 shows the transmitted waveforms of SBS optical limiting at different temperatures. The top of the transmitted pulse is almost a platform at 8°C, while a peak appeared at 15°C. This can be explained as follows: at a high temperature, kinematic viscosity is small and leads to a long phonon lifetime; thus the energy transfer is incomplete and the peak appears. In contrast, at a low temperature, the phonon lifetime is comparatively short and the complete energy transfer can lead to the generation of flat-top waveform (Hasi *et al.*, 2008*d*). Therefore, a low temperature is preferred to be chosen for the generation of flat-top pulse in time domain.

12.4. Conclusions

The effect of medium temperature upon characteristic of SBS and SBS optical limiting is investigated. The physical mechanism behind is analyzed theoretically and experimentally

Table 9. *The SBS parameters of some media at room temperature*

Medium	Absorption coefficient (cm^{-1})	SBS gain coefficient (cm/GW)	Density (g/cm^3)	SBS threshold (mJ)	Phonon lifetime (ns)
FC-72	$<10^{-3}$	6.0	1.68	2.5	1.2
FC-87	$<10^{-3}$	6.6	1.65	2.2	1.1
FC-77	$<10^{-3}$	5.1	1.78	4.3	0.7
FC-84	$<10^{-3}$	6.0	1.73	4.0	0.9

https://doi.org/10.1017/S0263034611000644 Published online by Cambridge University Press

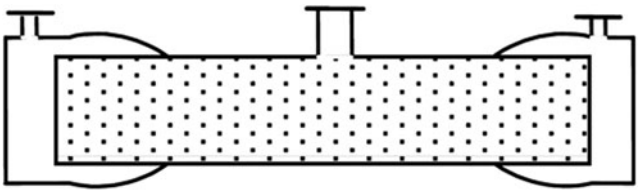

Fig. 69. SBS cell with double window plates, the cell length is 60 cm and inside diameter is 5 cm.

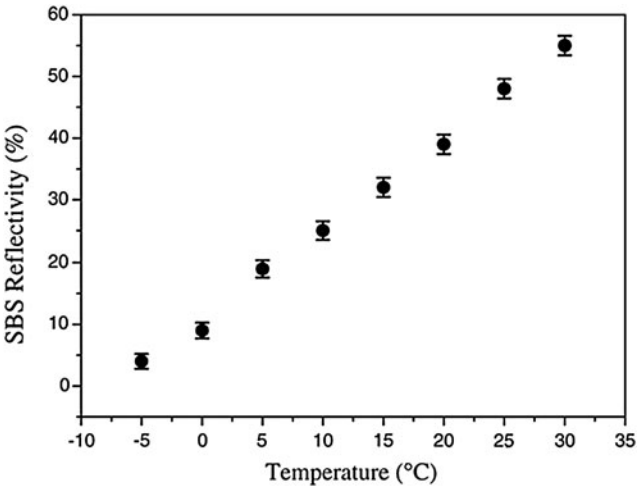

Fig. 70. The dependence of SBS reflectivity on medium temperature as pump energy fixed at 40 mJ.

verified in Continuum's Nd:YAG Q-switched laser system using FC-72 as the SBS medium. The temperature affects the electro-strictive coefficient, refractive index, density, and acoustic velocity of the medium weakly. In contrast, the kinematic viscosity, which is inversely proportional to the temperature, is related to gain coefficient and phonon lifetime, and thus greatly affects the SBS characteristics. Therefore, in the low temperature, the kinematic viscosity is usually high, which can lead to a small gain coefficient and a short phonon lifetime. Therefore, the SBS characteristic can be changed by controlling the temperature to a great extent.

ACKNOWLEDGMENTS

This work is supported by National Natural Science Foundation of China (Grant Nos. 60778019, 60878005), the Program for New Century Excellent Talents in University (Grant No. NCET-08-0173), and the Program of Excellent Team in Harbin Institute of Technology.

13. SUPPRESSION OF STIMULATED BRILLOUIN SCATTERING IN LASER BEAM HOT SPOTS (R.P. Sharma, Prerana Sharma, Shivani Rajput, and A.K. Bhardwaj)

13.1. Introduction

The nonlinear interaction of high power lasers with high density plasmas has been a subject of active research for decades

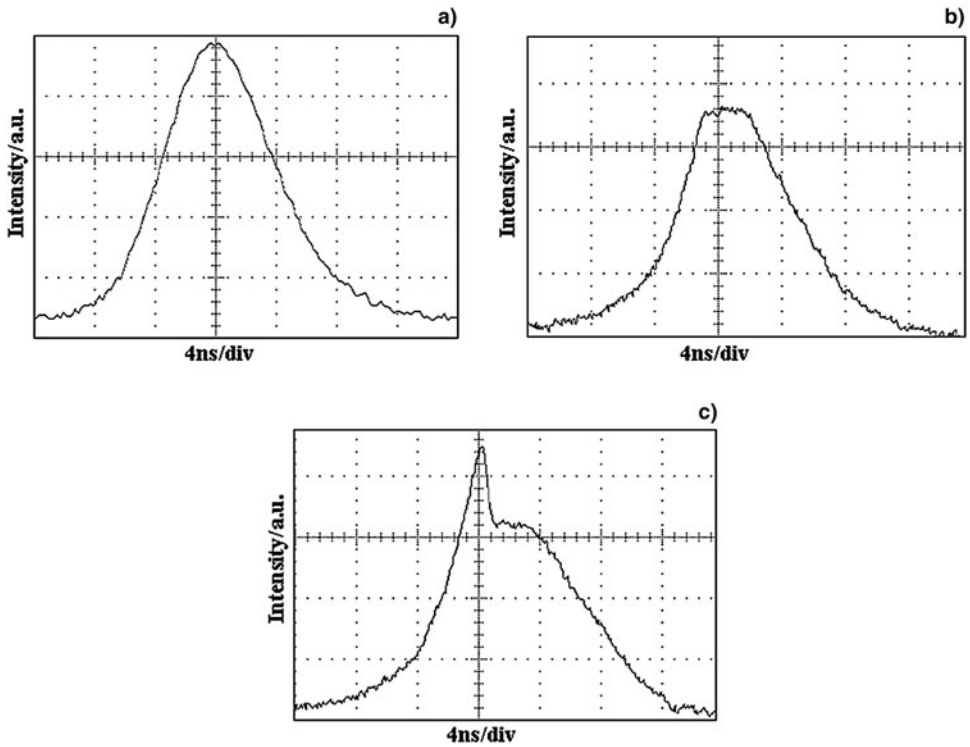

Fig. 71. (**a**) Pump waveform and transmitted waveforms of SBS at different temperature (**b**) 8°C, and (**c**) 15°C, respectively.

https://doi.org/10.1017/S0263034611000644 Published online by Cambridge University Press

due to its relevance to laser driven fusion (Kruer, 2000; Bruckner & Jorna, 1974). The increasing use of high power laser beams in various applications has worldwide interest in laser-plasma interaction (Borghesi *et al.*, 2007; Laska *et al.*, 2008; Dromey *et al.*, 2009) in the nonlinear regime. In collisionless plasmas, the nonlinearity arises through the ponderomotive force-induced redistribution of plasma. It is well known that various laser-plasma instabilities like, filamentation (Kaw *et al.*, 1973; Young *et al.*, 1988; Deutsch *et al.*, 2008), harmonic generation (Ozoki *et al.*, 2007; Baeva *et al.*, 2007; Dombi *et al.*, 2009), stimulated Raman scattering (SRS) (Kline *et al.*, 2009; Bers *et al.*, 2009), and stimulated Brillouin scattering (SBS) (Hüller *et al.*, 2008; Hasi *et al.*, 2007; Kappe *et al.*, 2007; Wang *et al.*, 2009*a*) might be generated from the interaction of laser pulses with plasmas. These instabilities affect the laser-plasma coupling efficiency and SRS can even produce energetic electrons (Estrabrook *et al.*, 1980), which can preheat the fusion fuel and change the compression ratio. Most of the theories of stimulated scattering and harmonic generation are based on the assumption of a uniform laser pump. This is contrary to almost all the experimental situations, where laser beams of finite transverse size, having non-uniform intensity distribution along their wavefront, are used. Such beams may modify the background plasma density and suffer filamentation (self-focusing). The non-uniformity in the intensity distribution of the laser also affects the scattering of a high power laser beam.

SBS is a parametric instability (Drake *et al.*, 1974; Hüller, 1991) in plasma in which an electromagnetic wave (ω_0, k_0) interacts with an ion acoustic wave (ω, k) to produce a scattered electromagnetic wave (ω_s, k_s). SBS has been a concern in inertial confinement fusion application because it occurs up to the critical density layer of the plasma and affects the laser plasma coupling efficiency. SBS produces a significant level of backscattered light; therefore, it is important to devise techniques to suppress SBS. In plasmas of heavy ions, this could be accomplished by introducing a small fraction of light ion species that could incur heavy Landau damping in the ion acoustic wave (IAW) and suppresses the SBS (Baldis *et al.*, 1998; Fernandez *et al.*, 1996).

Little agreement between theory (Baldis *et al.*, 1993; Baton *et al.*, 1994) and experiments (Chirokikh *et al.*, 1998) has been reported so far, in spite of intensive studies of SBS during the last two decades in both fields. Most of the earlier studies (on the discrepancy between theoretical expectations and experimental results) are focused with the saturation effects of SBS-driven IAW, such as kinetic effects, harmonic generation, and decay into sub-harmonic IAW components. But it has been shown recently (Myatt *et al.*, 2001; Fuchs *et al.*, 2001) that due to self-focusing, the laser pump beam looses coherence when propagating into the plasma. This incoherence could act as another potential saturation mechanism for the SBS instability. For such cases, when induced incoherence reduces SBS, the nonlinear saturation effects studied in the past may be of minor importance, because plasma waves stay at relatively low amplitudes. Recently, Hüller *et al.* (2008) did the numerical simulation in two dimensions to support this idea. The spatial incoherence in the pump laser beam due to filamentation instability (self-focusing) and non- monotonous flow, cause an inhomogeneity and the SBS decreases. In their simulation, IAW amplitudes were kept small (around 1%) so that the traditionally assumed nonlinear saturation mechanisms of SBS through nonlinear IAW can be neglected.

Giulietti *et al.* (1999) have measured the stimulated Brillouin back scattering from the interaction of a laser pulse with preformed, inhomogeneous plasma in conditions favorable to self-focusing. Spectral and temporal features of the reflectivity suggest a strong effect of self-focusing on back-SBS. Baton *et al.* (1998) have experimentally shown the dependence of the SBS reflectivity on both the focusing aperture and the incident laser intensity for millimeter size, homogeneous, stationary plasmas. Baldis *et al.* (1998) have given the experimental evidence of the transverse localization of SBS emission to the laser beam axis, demonstrating that only a few small regions of plasma contribute to the emission. As a consequence, SBS reflectivity of these regions is much higher than the average SBS reflectivity, by a factor of 50–100. Eliseev *et al.* (1996) have shown that the SBS reflectivity from a single laser hot spot is much lower than that predicted by a simple three wave coupling model because of the diffraction of the scattered light from the spatially localized IAW.

In this work, we have studied the effect of self-focusing and localization of IAW on SBS process (as a specific case, backscattering, for which $k = 2k_0$), using paraxial ray approximation. The nonlinear coupling between the filamented laser beam and ion acoustic wave results in the modification of the Eigen frequency of IAW; consequently, enhanced Landau damping of IAW and a modified mismatch factor in the SBS process occur. Due to enhanced Landau damping, there is a reduction in intensity of IAW, and the SBS process gets suppressed.

In the present work, the level of IAW amplitude (after nonlinear coupling between IAW and laser beam) is around 1%. Our work goes one step ahead from the Hüller *et al.* (2008) simulation, and highlights the underlying possible physical process of this SBS saturation. This physical process involves the localization of IAW due to nonlinear coupling between pump laser beam (filamented/self-focused) and IAW due to ponderomotive nonlinearity (Sodha *et al.*, 2009). As a consequence, the Landau damping of IAW increases and hence the SBS reflectivity is suppressed. Therefore, the present work takes into account the mechanism proposed by Hüller *et al.* (2008) in their simulation and IAW localization also for the saturation of SBS.

The work is organized as follows: In Section 13.2, we give the brief summary of the basic equations of the propagation of laser beam. The modified equations for the excitation of

https://doi.org/10.1017/S0263034611000644 Published online by Cambridge University Press

IAW are studied in the Section 13.3. The effect of localization of the IAW is also presented in the same section. In Section 13.4, we derive the basic equations that govern the dynamics of SBS process and SBS reflectivity. The important results and conclusions based on the present investigation are presented in the last section.

13.2. Equation of Laser Beam Propagation

A high power Gaussian laser (pump) beam of frequency ϖ_0 and the wave vector k_0 is considered to be propagating in hot collisionless and homogeneous plasma along the z axis. When a laser beam propagates through the plasma, the transverse intensity gradient generates a ponderomotive force, which modifies the plasma density profile in the transverse direction as (Sodha *et al.*, 1976)

$$N_{0e} = N_{00}\exp\left(-\frac{3}{4}\alpha\frac{m}{M}E\cdot E^*\right), \tag{1}$$

$$\alpha = \frac{e^2M}{6k_\beta T_0\gamma m^2\omega_0^2}.$$

Where λ, e and m are the electronic charge and mass, M and T_0 are, respectively, mass of ion and equilibrium temperature of the plasma. N_{0e} is the electron concentration in the presence of the laser beam, N_{00} is the electron density in the absence of the beam, k_β is the Boltzman's constant and γ is the ratio of the specific heats.

The wave equation for the pump laser beam has been solved using Wentzel-Kramers-Brillouin approximation and paraxial-ray approximation, and the electric field of the pump laser beam can be written as (Sodha *et al.*, 1976; Akhmanov *et al.*, 1968)

$$E = E_{00}\exp\{i[\omega_0 t - k_0(S_0 + z)]\}, \tag{2}$$

where wave number and Eikonal of the beam is given as

$$k_0^2 = \frac{\omega_0^2}{c^2}\left(1-\frac{\omega_p^2}{\omega_0^2}\right) = \frac{\omega_0^2}{c^2}\varepsilon_0, \tag{3a}$$

$$S_0 = \frac{r^2}{2}\frac{1}{f_0}\frac{df_0}{dz} + \Phi_0(z). \tag{3b}$$

The intensity distribution of the laser beam for $z > 0$ may be written as (Akhmanov *et al.*, 1968)

$$E\cdot E^* = \frac{E_{00}^2}{f_0^2}\exp\left(-\frac{r^2}{r_0^2}\right), \tag{4}$$

where E_{00} is the axial amplitude, r_0 is the initial beam width, r refers to the cylindrical coordinate system, and $\varepsilon_0 = (1 - \bar{\omega}_p^2/\bar{\omega}_0^2)$ is the linear part of the plasma dielectric constant. $\bar{\omega}_p$ is the electron plasma frequency, and f_0 is the dimensionless beam width parameter, satisfying the boundary conditions: $f_0|_{z=0} = 1$ and $df_0/dz|_{z=0} = 0$, governed by the equation (Sodha *et al.*, 1976)

$$\frac{\partial^2 f_0}{d\xi^2} = \frac{1}{f_0^3} - \left(\frac{3}{4}\alpha\frac{m}{M}E_{00}^2\right)\frac{\omega_p^2R_{d0}^2}{\varepsilon_0\omega_0^2f_0^3r_0^2}\exp\left\{-\frac{3}{4}\alpha\frac{m}{M}\frac{E_{00}^2}{f_0^2}\right\}, \tag{5}$$

where $R_{d0} = k_0r_0^2$ is the diffraction length and $\xi = z/R_{d0}$ is the dimensionless parameter. The density of the plasma varies through the channel due to the ponderomotive force. Therefore, the refractive index increases and the laser beam get focused in the plasma. Eq. (4) gives the intensity profile of the laser beam in the plasma, which is shown in Figure 72, using the following parameters in numerical calculation: the incident laser intensity equals $\alpha E_{00}^2 = 1.22$ (laser power flux $= 10^{16}$ W/cm^2), $r_0 = 12$ μm, $n/n_{cr} = 0.1$, and $(T_e/T_i) = 10$.

13.3. Localization of Ion Acoustic Wave

Nonlinear interaction of an ion acoustic wave with the laser beam filaments leads to its excitation. To analyze this excitation process of IAW in the presence of ponderomotive nonlinearity and filamented laser beam, we use the fluid model as

$$\frac{\partial n_{is}}{\partial t} + N_0(\nabla\cdot V_{is}) = 0, \tag{6}$$

$$\frac{\partial V_{is}}{\partial t} + \frac{\gamma_i v_{thi}^2}{N_0}\nabla n_{is} + 2\Gamma_i V_{is} - \frac{e}{M}E_{si} = 0. \tag{7}$$

The electric field E_{si} is associated with the IAW and satisfies the Poisson's equation,

$$\nabla\cdot E_{si} = -4\pi e(n_{es} - n_{is}) \tag{8}$$

where n_{es} is given by

$$n_{es} = n_{is}\left[1 + \frac{k^2\lambda_d^2}{(N_{0e}/N_{00})}\right]^{-1}. \tag{9}$$

The Landau damping coefficient for IAW is given by

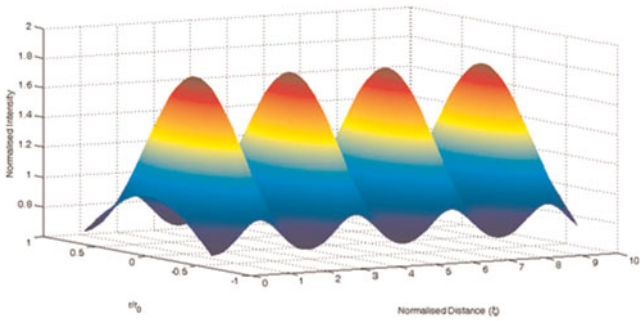

Fig. 72. (Color online) Variation in laser beam intensity with normalized distance ($\xi = z/R_{d0}$) and radial distance (r) for laser power $\alpha E_{00}^2 = 1.22$ and $r_0 = 11.5$ μm.

https://doi.org/10.1017/S0263034611000644 Published online by Cambridge University Press

(Krall & Trivelpiece, 1973)

$$2\Gamma_i = \frac{k}{(1+k^2\lambda_d^2)}\left(\frac{\pi k_\beta T_e}{8M}\right)^{1/2} \times\left[\left(\frac{m}{M}\right)^{1/2}+\left(\frac{T_e}{T_i}\right)^{3/2}\exp\left(-\frac{T_e/T_i}{(1+k^2\lambda_d^2)}\right)\right]. \tag{10}$$

where T_e and T_i are electron and ion temperatures, V_{is} is the ion fluid velocity, $\lambda_d = (k_b T_0/4\pi N_{00} e^2)^{1/2}$ is the Debye length, and $v_{thi} = (k_b T_i/M)^{1/2}$ is the thermal velocity of ions. Combining Eqs. (6), (7), and (9) and assuming that the plasma is cold i.e., $v_{thi}^2 \ll c_s^2$, one obtains the general equation governing the ion density variation

$$\frac{\partial^2 n_{is}}{\partial t^2} + 2\Gamma_i\frac{\partial n_{is}}{\partial t} - c_s^2\nabla^2 n_{is} + k^2 c_s^2 \times\left(-1+\frac{1}{1+k^2\lambda_d^2\left(N_{0e}/N_{00}\right)^{-1}}\right)n_{is} = 0, \tag{11}$$

where $c_s = (k_\beta T_e/M)^{1/2}$ is the speed of the IAW for $T_e \gg T_i$. The solution of the above equation can be written as

$$n_{is} = n(r,z)\exp\{i[\omega t - k(z+s(r,z))]\}, \tag{12}$$

here s is the Eikonal for IAW. The frequency and wave number of the IAW satisfy the following dispersion relation in the presence of laser beam

$$\omega^2 = \frac{k^2 c_s^2}{1+k^2\lambda_d^2(N_{0e}/N_{00})^{-1}}. \tag{13}$$

Substituting Eq. (12) into Eq. (11) and separating the real and imaginary parts, one obtains, the real part as

$$2\left(\frac{\partial s}{\partial z}\right)+\left(\frac{\partial s}{\partial r}\right)^2 = \frac{1}{nk^2}\left[\frac{\partial^2 n}{\partial r^2}+\frac{1}{r}\frac{\partial n}{\partial r}\right]+\frac{\omega^2}{k^2 c_s^2} +\left[1-\frac{1}{1+k^2\lambda_d^2(N_{0e}/N_{00})^{-1}}\right] \tag{14a}$$

and imaginary part as

$$\frac{\partial n^2}{\partial z}+\left(\frac{1}{r}\frac{\partial s}{\partial r}+\frac{\partial^2 s}{\partial r^2}\right)n^2+\frac{\partial n^2}{\partial r}\frac{\partial s}{\partial r}+\frac{2\Gamma_i}{c_s^2}\frac{\omega n^2}{k}=0. \tag{14b}$$

To solve the coupled Eqs. (14a) and (14b), we assume the initial radial variation of IAW density perturbation to be Gaussian, and the solution at finite z may be written as

$$n^2 = \frac{n_0^2}{f^2}\exp\left(-\frac{r^2}{a^2 f^2}-2k_i z\right) \tag{15a}$$

and

$$s = \frac{r^2}{2}\frac{1}{f}\frac{df}{dz}+\Phi(z), \tag{15b}$$

where $k_i = \Gamma_i\bar{\omega}/kc_s^2$, is the damping factor, f is a dimensionless beam width parameter and a is the initial beam width of the acoustic wave. We have used the following boundary conditions: $df/dz = 0$, f 1 at $z = 0$. Using Eq. (15) in Eq. (14a) and equating the coefficients of r^2 on both sides, we obtain the following equation governing f

$$\frac{\partial^2 f}{\partial\xi^2} = \frac{R_{d0}^2}{R_d^2 f^3}-\left(\frac{3}{4}\alpha\frac{m}{M}\frac{E_{00}^2}{r_0^2}\frac{f}{f_0^4}\right)\frac{R_{d0}^2 k^2\lambda_d^2}{(1+k^2\lambda_d^2)^2} \times\exp\left(\frac{3}{4}\alpha\frac{m}{M}\frac{E_{00}}{f_0^2}\right), \tag{16}$$

where $R_d = ka^2$ is the diffraction length of the IAW. Eq. (16) represents the density profile of IAW in the plasma when the coupling between self-focused (filamented) laser beam and IAW is taken into account. It is interesting to compare Eq. (16) with Eq. (5), i.e., self-focusing of laser pump wave. In the absence of the coupling between the laser beam and acoustic wave, the second term in Eq. (16) is zero and the solution of Eq. (16) is given by

$$f = 1+\frac{z^2}{R_d^2}.$$

Thus, propagating a distance R_d, the width a is $\sqrt{2}$ enlarged by and the axial amplitude of density perturbation in IAW is decreased by the same factor even in the absence of Landau damping.

We can, however, obtain an analytical solution of Eq. (16) in special case. When the laser beam has the critical power for self-focusing, the diffraction term (the first term on the right-hand-side of Eq. (5)) balances the nonlinear term in Eq. (5). Under such conditions ($f_0 = 1$), the main beam propagates without convergence and divergence and is generally known as the uniform waveguide mode. Therefore, the solution for f is given by

$$f^2 = \frac{A+B}{2B}-\frac{A-B}{2B}\cos\left(2\sqrt{B}z\right),$$

where

$$A = \frac{1}{R_d^2}\text{ and}$$

$$B = \left(\frac{3}{4}\alpha\frac{m}{M}\frac{E_{00}^2}{r_0^2}\right)\frac{k^2\lambda_d^2}{(1+k^2\lambda_d^2)^2}\times\exp\left(\frac{3}{4}\alpha\frac{m}{M}E_{00}^2\right).$$

Therefore, the amplitude of IAW (given by Eq. (15a)), which depends on f will be oscillating with z due to this nonlinear coupling, hence the IAW gets localized.

When the power of laser beam is greater than the critical power for self-focusing, we have solved Eq. (15a) numerically with the help of Eq. (16) to obtain the density perturbation at finite z. The result is shown in Figure 73a, for typical laser parameters as we have used in previous section.

https://doi.org/10.1017/S0263034611000644 Published online by Cambridge University Press

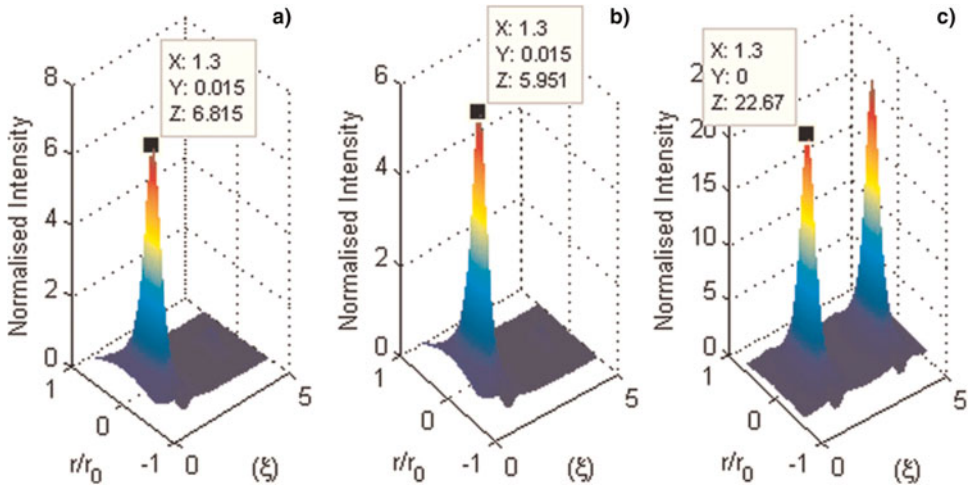

Fig. 73. (Color online) Variation in IAW intensity with normalized distance ($\xi = z/R_{d0}$) and radial distance (r), for a =19 μm, (**a**) with Initial Landau damping ($\Gamma_i/\bar{\omega}$) = 0.0142 (**b**) with modified Landau damping ($\Gamma_i/\bar{\omega}$) = 0.0155, (**c**) with zero Landau damping.

It is evident from the figure that the IAW gets excited due to nonlinear coupling with the high power laser beam because of the ponderomotive nonlinearity. If we take the zero Landau damping of IAW, we get the structure having the amplitude varying periodically with the z coordinate as shown in Figure 73c.

The localization may be understood as follows: Because of the ponderomotive force exerted by the pump laser beam, the electrons are redistributed from the axial region. According to the dispersion relation $\omega^2 = k^2c_s^2/(1 + k^2\lambda_d^2(N_{0e}/N_{00})^{-1})$, the phase velocity $\bar{\omega}/k$ of the acoustic wave has a minimum on the axis and is increasing away from the axis. If we consider the initial wavefront of the electrostatic wave, the secondary wavelets travel with minimum velocity along the axis and with higher velocity away from the axis. As the wavefront advances in the plasma, focusing occurs, and the amplitude of the density perturbation increases. When the size of the wave front reduces considerably, diffraction effects also become important and hence the amplitude of the density perturbation starts to decrease.

We can calculate the periodicity length L of localized structures by putting $r = 0$ in Eq. (15a), as shown in Figure 74. According to Figure 74, value of L comes out to be $2.62R_{d0}$. If we take the fast Fourier transform of the structure as shown in Figure 74, we get the spectral lines in one structure at a separation of $k_A = 2\pi/L$, and the value of k_A is coming out to be 2.4 $R_{d0}{}^{-1}$. We have shown these structures in Figure 75a. These periodic localized structures are similar to the structures in a periodic potential well. This situation can be modeled by representing Eq. (11) in the form of Mathew's equation in a periodic potential well. Therefore, taking the density variation as $e^{i\bar{\omega}t}$ in Eq. (11), one can write

$$i\left(\frac{\partial}{\partial T} + \Gamma_L\right)n_{is} + \frac{\partial^2 n_{is}}{\partial Z^2} - Nn_s = 0, \tag{17}$$

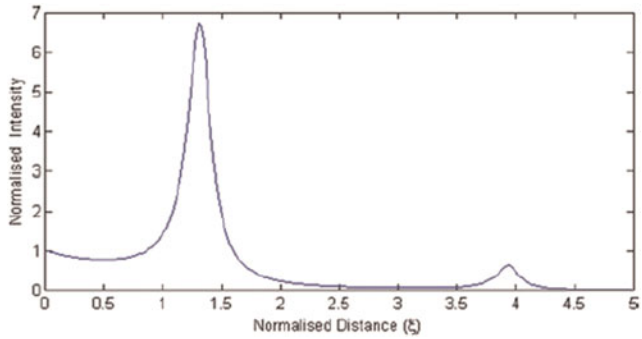

Fig. 74. (Color online) Variation in IAW intensity with normalized distance (ξ) in real space at $r = 0$ corresponding to Figure 73.

here,

$$T = \frac{t}{(1/2\omega)}, \quad \Gamma_L = \Gamma_i/2\omega), \quad Z = \frac{z}{(c_s/2\omega)}, \text{ and}$$
$$N = \mu \exp(ik_A z) \tag{18}$$

where μ represents the dimensionless amplitude of the density perturbation in k-space. The normalized density of the first spectral component in Figure 75a is 5.801, which is at a distance of k_A from the central component. The value of μ^2 comes out to be $\mu^2 = (N_k{}^2/N_{00}{}^2) = 0.0058$, in which we have used the seed value of IAW $(N_0{}^2/N_{00}{}^2) = 10^{-3}$. If n_{is} is of the form, $n_{is} = \psi\exp(-i\int_0^T d\tau\Lambda)$, then we may write Eq. (17) in the form of Eigen value equation (Rozmus *et al.*, 1987)

$$(\Lambda + i\Gamma_L)\psi + \frac{\partial^2}{\partial Z^2}\psi - N\psi = 0. \tag{19}$$

We assume the solution of Eq. (19) in the form of Bloch

https://doi.org/10.1017/S0263034611000644 Published online by Cambridge University Press

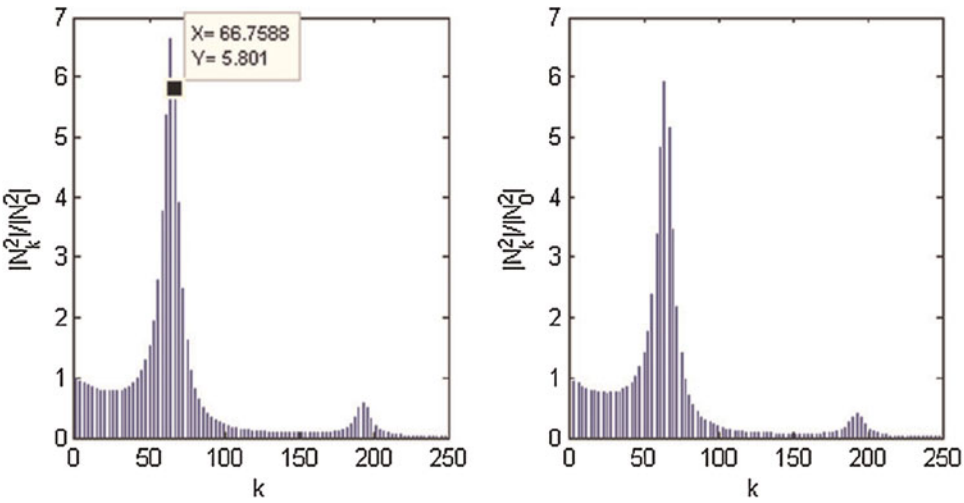

Fig. 75. (Color online) Comparison of Power spectrum of IAW, for a $E_{00}^2 = 1.6$ (**a**) with Initial Landau damping $(\Gamma_i/\omega) = 0.0142$ (**b**) with modified Landau damping $(\Gamma_i/\omega) = 0.0155$.

wave function as

$$\psi = \sum_n \exp\left[i(k + nk_A)Z\right]\psi_n. \tag{20}$$

Substituting this solution in Eigen value Eq. (19), we obtain the equation

$$(\Lambda + i\Gamma_L^0)\psi_0 - K^2\psi_0 = \mu(\psi_{+1} + \psi_{-1}), \tag{21a}$$

and

$$(\Lambda + i\Gamma_L^n)\psi_n - (K + nK_A)^2\psi_n = \mu(\psi_{n-1} + \psi_{n+1}), \tag{21b}$$

where

$$\Gamma_L^n \equiv \Gamma_L(k + nk_A).$$

Keeping only $\psi_0, \psi_{\pm 1}$ components, we obtain (Rozmus *et al.*, 1987) for $\Lambda = \Lambda_1 + i\Lambda_2$,

$$\begin{aligned}\Lambda_1 &= K^2\left(1 + \sqrt{(1 + 4\mu^2/k^4)}\right)/2 \text{ and } \Lambda_2 \\ &= -\bar{\Gamma}_L/(1 + \Delta/\Lambda_1),\end{aligned} \tag{22}$$

where the effective dampin $\bar{\Gamma}_L$ is

$$\bar{\Gamma}_L = \Gamma_L(k) + \mu^2\frac{\Gamma_L(k + k_A)}{(k + k_A)^4}, \tag{23}$$

and mismatch factor has the form

$$\Delta = \Lambda_1 - k^2 \tag{24}$$

Eqs. (22) and (23) give the expression for modified frequency and enhanced Landau damping of the IAW, respectively. The value of the enhanced Landau damping is 0.0155, whereas the initial damping value was 0.0142. Therefore, we have approximately 10% increment in Landau damping of IAW, and the mismatch factor in Eigen frequency is coming out to be 0.0338. It is obvious that Landau damping governs the intensity of the IAW, and due to localization of IAW, the effective damping of the acoustic wave increases, therefore, as a result, the intensity of IAW reduces accordingly, as shown in Figure 73b. The enhanced Landau damping effect is also observable in the modified spectra of the IAW, as shown in Figure 75b.

13.4. Stimulated Brillouin Scattering

The high frequency electric field E_T, satisfies the wave equation

$$\nabla^2 E_T - \nabla(\nabla \cdot E_T) = \frac{1}{c^2}\frac{\partial^2 E_T}{\partial t^2} + \frac{4\pi}{c^2}\frac{\partial J_T}{\partial t}, \tag{25}$$

where J_T is the total current density vector in the presence of the high frequency electric field E_T and it is given by

$$J_T = -e\left(N_0 v_t + \frac{1}{2}n_{es}v_{t'}\right) - e\left(N_0 v_t + \frac{1}{2}n_{es}^* v_t\right). \tag{26}$$

E_T may be written as the sum of the electric field E of the pump laser beam and of the electric field E_S of the scattered wave, i.e.,

$$E_T = E\exp(i\omega_0 t) + E_S\exp(i\omega_S t). \tag{27}$$

Substituting Eqs. (26) and (27) into Eq. (25), and separating the equation for pump and scattered field.,

$$\nabla^2 E + \frac{\omega_0^2}{c^2}\left(1 - \frac{\omega_p^2}{\omega_0^2}\frac{N_{0e}}{N_{00}}\right)E = \frac{4\pi e}{c^2}\frac{1}{2}\frac{\partial}{\partial t}(n_{es}v_{t'}), \tag{28a}$$

$$\nabla^2 E_S + \frac{\omega_S^2}{c^2}\left(1 - \frac{\omega_p^2}{\omega_S^2}\frac{N_{0e}}{N_{00}}\right)E_S = \frac{4\pi e}{c^2}\frac{1}{2}\frac{\partial}{\partial t}(n_{es}^* v_t). \tag{28b}$$

In solving Eq. (28b), the term $\nabla(\nabla \times E_T)$ may be neglected in

https://doi.org/10.1017/S0263034611000644 Published online by Cambridge University Press

the comparison to the $\nabla^2 E_S$ term, assuming that the scale length of variation of the dielectric constant in the radial distance is much larger than the wavelength of the pump wave. Substituting $v_t = (ieE/m\omega_0)$ in Eq. (28b), one obtains

$$\nabla^2 E_S + \frac{\omega_S^2}{c^2}\left(1 - \frac{\omega_p^2}{\omega_S^2}\frac{N_{0e}}{N_{00}}\right)E_S = \frac{1}{2}\frac{\omega_p^2}{c^2}\frac{\omega_S}{\omega_0}\frac{n_{es}^*}{N_{00}}E, \tag{29}$$

let the solution of Eq. (29) be

$$E_S = E_{S0}(r, z)e^{+ik_{S0}z} + E_{S1}(r.z)e^{-ik_{S1}z}, \tag{30}$$

where $k_{S0}^2 = (\omega_S^2/c^2)(1 - (\omega_p^2/\omega_S^2)) = (\omega_s^2/c^2)\varepsilon_{S0}$ and k_{s1} and $\bar{\omega}_s$ satisfy the matching conditions

$$\omega_S = \omega_0 - \omega, \quad K_{S1} = k_0 - k.$$

Using Eq. (30) in Eq. (29), one gets

$$\begin{aligned} &-k_{S0}^2 E_{S0} + 2ik_{S0}\frac{\partial E_{S0}}{\partial z} + \left(\frac{\partial}{\partial r^2} + \frac{1}{r}\frac{\partial}{\partial r}\right)E_{S0} \\ &\quad + \frac{\omega_S^2}{c^2}\left[\varepsilon_{S0} + \frac{\omega_p^2}{\omega_S^2}\left(1 - \frac{N_{0e}}{N_{00}}\right)\right]E_{S0} = 0. \end{aligned} \tag{31}$$

$$\begin{aligned} &-k_{S1}^2 E_{S1} + (-2ik_{S1})\frac{\partial E_{S1}}{\partial z} + \left(\frac{\partial}{\partial r^2} + \frac{1}{r}\frac{\partial}{\partial r}\right)E_{S1} \\ &\quad + \frac{\omega_S^2}{c^2}\left[\varepsilon_{S0} + \frac{\omega_p^2}{\omega_S^2}\left(1 - \frac{N_{0e}}{N_{00}}\right)\right]E_{S1} \\ &\quad = \frac{1}{2}\frac{\omega_p^2}{c^2}\frac{\omega_S}{\omega_0}\frac{n_{es}^*}{N_{00}}E_0\exp(-ik_0 s_0). \end{aligned} \tag{32}$$

to a good approximation, the solution of Eq. (32) may be written as

$$E_{S1} = E'_{S1}(r, z)e^{-ik_0 S_0}, \tag{33}$$

substituting this into Eq. (32), one obtains

$$E'_{S1} = -\frac{1}{2}\frac{\omega_p^2}{c^2}\frac{n^*}{N_0}\frac{\omega_S}{\omega_0}\frac{E_0}{\left[k_{S1}^2 - k_{S0}^2 - \frac{\omega_p^2}{c^2}\left(1 - \frac{N_{0e}}{N_0}\right)\right]}. \tag{34}$$

Simplifying Eq. (31) and substituting $E_{S0} = E_{S00}e^{iksOSc}$, one obtains after separating the real and imaginary parts

$$\begin{aligned} 2\left(\frac{\partial S_c}{\partial z}\right) + \left(\frac{\partial S_c}{\partial r}\right)^2 &= \frac{1}{k_{S0}^2 E_{S00}}\left(\frac{\partial}{\partial r^2}\frac{1}{r}\frac{\partial}{\partial r}\right)E_{S00} \\ &\quad + \frac{\omega_p^2}{\omega_S^2\varepsilon_{S0}}\left(1 - \frac{N_{0e}}{N_{00}}\right), \end{aligned} \tag{35a}$$

$$\frac{\partial E_{S00}^2}{\partial z} + E_{S00}^2\left(\frac{\partial^2 S_c}{\partial r^2} + \frac{1}{r}\frac{\partial S_c}{\partial r}\right) + \frac{\partial S_c}{\partial r}\frac{\partial E_{S00}^2}{\partial r} = 0. \tag{35b}$$

The solution of these equations may again be written as

$$E_{S00}^2 = \frac{B'^2}{f_S^2}\exp\left(-\frac{r^2}{b^2 f_S^2}\right), \tag{36a}$$

$$S_c = \frac{r^2}{2}\frac{1}{f_S}\frac{\partial f_S}{\partial z} + \Phi(z), \tag{36b}$$

where b is the initial beam width of the scattered wave. Substituting the above solution in Eq. (35a) and equating the coefficients of r^2 on both sides, we get the equation of the spot size of scattered wave as

$$\begin{aligned} \frac{d^2 f_s}{d\xi^2} &= \frac{R_{d0}^2}{R_{ds}^2 f_s^3} - \frac{\omega_p^2}{\omega_s^2\varepsilon_{S0}}\left(\frac{3}{4}\alpha\frac{m_e}{m_i}E_{00}^2\right)\frac{f_s}{f_0^4}\frac{R_{d0}^2}{r_0^2} \\ &\quad \times\exp\left(-\frac{3}{4}\alpha\frac{m_e}{m_i}\frac{E_{00}^2}{f_0^2}\right), \end{aligned} \tag{37}$$

where $R_{dS} = k_{S0}b^2$ is the diffraction length of the scattered radiation.

It is easy to see from Eq. (15) that the IAW is damped as it propagates along the z-axis. Consequently, the scattered wave amplitude should also decrease with increasing z. Therefore, expressions for B' and b may be obtained on applying suitable boundary conditions $E_S = E_{S0}\exp(ik_{S0}z) + E_{S1}\exp(-ik_{S1}z) = 0$ at $z = z_c$; here z_c is the point at which the amplitude of the scattered wave is zero. This immediately yields

$$\begin{aligned} B' = &-\frac{1}{2}\frac{\omega_p^2}{c^2}\frac{\omega_S}{\omega_0}\frac{n_0}{N_{00}}\frac{E_{00}f_S(z_c)}{f(z_c)f_0(z_c)} \\ &\times\frac{\exp(-k_i z_c)}{\left[k_{S1}^2 - k_{S0}^2 - \frac{\omega_p^2}{c^2}\left(1 - \frac{N_{0e}}{N_{00}}\right)\right]} \\ &\times\frac{\exp[-i(k_{S1}z_c + k_0 S_0)]}{\exp[i(k_{S0}S_c + k_{S0}z_c)]}, \end{aligned}$$

with condition

$$\frac{1}{b^2 f_s^2(z_c)} = \frac{1}{r_0^2 f_0^2(z_c)} + \frac{1}{a^2 f^2(z_c)}. \tag{38}$$

The reflectivity is defined as the ratio of scattered flux and incident flux, $R = (|E_S|^2/|E_{00}|^2)$. By using Eqs. (30), (33), (34), (36), and (38), we get $E_S E^*_S = E_{S0}E^*_{S0} + E_{S0}E^*_{S1}\exp[i(k_{S0}+k_{S1})z] + E_{S1}E^*_{S0}\exp[-i(k_{S0}+k_{S1})z] + E_{S1}E^*_{S1}$ and

$$\begin{aligned} R = &\frac{1}{4}\left(\frac{\omega_p^2}{c^2}\right)^2\left(\frac{\omega_s}{\omega_0}\right)^2\left(\frac{n_0}{N_{00}}\right)^2 \\ &\times\frac{1}{\left[k_{s1}^2 - k_{s0}^2 - \frac{\omega_p^2}{c^2}\left(1 - \frac{N_{0e}}{N_{00}}\right)\right]^2} \\ &\times\left[\begin{array}{l} \frac{f_S^2(z_c)}{f^2(z_c)f_0^2(z_c)}\frac{1}{f_S^2}\exp\left(-2k_i z_c - \frac{r^2}{b^2 f_s^2}\right) \\ +\frac{1}{f^2 f_0^2}\exp\left(-\frac{r^2}{a^2 f^2} - \frac{r^2}{b^2 f_0^2} - 2k_i z\right) \\ +\frac{1}{2}\frac{1}{ff_0 f_s}\frac{f_s(z_c)}{f(z_c)f_0(z_c)} \\ \times\exp\left(-\frac{r^2}{2b^2 f_s^2} - \frac{r^2}{2a^2 f^2} - \frac{r^2}{2b^2 f_0^2}\right) \\ \cdot\exp\{-k_i(z + z_c)\}\cos\{(k_{S0} + k_{S1})(z - z_c)\} \end{array}\right]. \end{aligned} \tag{39}$$

It is apparent from the above equation that the reflectivity is dependant on the intensity of IAW and damping factor. To observe the effect of localization of IAW on SBS reflectivity, we have included the expression of modified Eigen frequency, (Eq. (22)) and effective damping, (Eq. (23)) in the

https://doi.org/10.1017/S0263034611000644 Published online by Cambridge University Press

above equation. It is clearly evident from Figure 76 that the SBS reflectivity gets reduced in the presence of the new Eigen frequency and damping values by almost the same factor as the intensity of the IAW decreases. In Figure 76, the solid red line (online only) shows the reflectivity with initial damping value and the dashed blue line (online only) shows the reflectivity including the effective enhanced Landau damping. If we calculate the integrated SBS reflectivity in two cases: namely (1) with initial damping of IAW and (2) with modified enhanced damping of IAW, we find that the reduction in SBS reflectivity comes out to be approximately 10%.

13.5. Conclusion

In the present work, we studied the filamentation of the laser beam in paraxial regime considering ponderomotive nonlinearity in hot collisionless plasma. It is evident from the results that the IAW gets excited due to nonlinear coupling with the high power filamented laser beam, and due to Landau damping, it gets damped as it propagates. The coupling is so strong that the IAW becomes highly localized and produces periodic structures. Further we discussed the effect of localization of IAW, this resulted in the modification of the Eigen frequency of IAW; consequently, an enhanced Landau damping of the IAW and a modified mismatch factor in the SBS process occurred. Solving the Eigen value problem we obtained an enhanced Landau damping, which resulted in a reduction in the intensity of the IAW. As a consequence, the back-reflectivity of the SBS process is suppressed by a factor of approximately 10%. These results should find applications in the laser induced fusion scheme where a reduction in SBS will improve the laser plasma coupling efficiency.

ACKNOWLEDGMENTS

This work was partially supported by DST, Government of India. One of the authors (Prerana Sharma) is grateful to AICTE India for providing financial assistance. One of the authors (Shivani) is grateful to Dr. R. Uma for useful discussions.

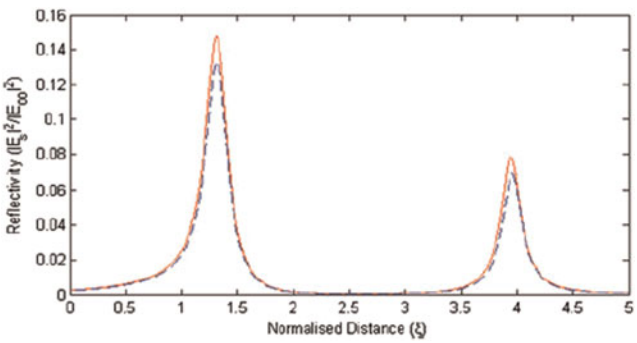

Fig. 76. (Color online) Variation in normalized back scattered reflectivity of SBS, $|Es|^2/|E_{00}|^2$ with normalized distance, (**a**) when $(\Gamma_i/\omega) = 0.0142$ (solid red line) and (**b**) when $(\Gamma_i/\omega) = 0.0155$ (blue dashed line).

14. A COMPOSITE PHASE CONJUGATOR BASED ON BRILLOUIN ENHANCED FOUR-WAVE MIXING COMBINING WITH STIMULATED BRILLOUIN AMPLIFICATION (C.Y. Zhu, Z.W. Lu, and W.M. He)

14.1. Introduction

Stimulated Brillouin scattering (SBS) optical phase conjugation (OPC), a technique with profound significance to high-power laser science, has been studied and made great efforts to application practically by researchers all over the world for decades (Zel'dovich *et al.*, 1972; Basov & Zubarev, 1979; Meister *et al.*, 2007; Ostermeyer *et al.*, 2008). In demand for large laser engineering such as inertial confinement fusion and inertial fusion energy, works on SBS phase conjugator, SBS beam combiner, and so on, are being carried out by more and more research teams (Kong *et al.*, 2005*c*, 2006, 2007*b*, 2008, 2009*a*; Kappe *et al.*, 2007; Hasi *et al.*, 2007, 2008*d*; Wang *et al.*, 2007, 2009*a*; Yoshida *et al.*, 2007). As well known, advantages of the SBS phase conjugator are high energy-conversion efficiency and simple structure. However, the acoustic wave, which plays a crucial role in SBS process, is developed from the noise in Brillouin medium (Boyd *et al.*, 1990), which makes the phase conjugate wave instable in many situations. For instance, phase jumps or intensity modulations are frequently observed in experiments (Shahraam *et al.*, 1998; Yang *et al.*, 2001), and when the leading-edge of the laser pulse is shorter than or comparable with the phonon lifetime of the Brillouin medium, SBS phase-conjugate fidelity and its stability will deteriorate severely (Dane *et al.*, 1992), which keeps this technique far away from applications of short pulse such as fast ignition laser pulse. Besides, the Stokes wave competes with optical noise modes throughout its generation and amplification processes, leading to the existence of non-conjugate components of the output wave, that is to say, and the phase-conjugate fidelity can never really achieve 100% (Zel'dovich *et al.*, 1982). So far as it goes, problems mentioned above, whose root is the noise-origin characteristic of the acoustic wave, have severe limiting factors for practical application of SBS phase conjugator.

There is another OPC technique, called Brillouin enhanced four-wave mixing (BEFWM), which is also based on acousto-optic interaction, but different from SBS in acoustic origin mechanism in nature (Scott & Ridley, 1989). In BEFWM process, acoustic wave is driven by optical coherent beating patterns and built up instantaneously without acoustic-relaxation-time restriction of the medium. This non-noise process not only keeps OPC stable and transient-state-adaptable but also exhibits advantages as non-threshold and a 100% conjugate fidelity. In the past decades, researches on BEFWM mainly focused on the conjugate-amplification of weak optical signals, and have gain many achievements (Andreev *et al.*, 1989; Lanzerotti *et al.*, 1996; Zhu *et al.*, 2007). However, when BEFWM

https://doi.org/10.1017/S0263034611000644 Published online by Cambridge University Press

operates with large incident signals as a high-power phase conjugator, its efficiency, i.e., total reflectivity, will be low because the energy of the conjugate wave comes from the reference wave instead of the signal wave itself (Zhu *et al.*, 2008).

In this work, a composite phase conjugator scheme, in which mechanism of BEFWM and SBS are combined in a compact structure is reported. The BEFWM provides phase conjugate wave seed with fast response, high quality and stability, which is then magnified by stimulated Brillouin amplification (SBA) with high energy-conversion efficiency. As a result, advantages of BEFWM and SBS can be realized at the same time. In the following sections, the theoretical model is set up, as well as numerical simulations, and demo experiments are carried out. Feasibility of the BEFWM-SBA phase conjugator is verified sufficiently.

14.2. Theory

14.2.1. Physical Model

Physical model of the BEFWM-SBA composite phase conjugator is shown in Figure 77. E_1 and E_2, in Figure 77a, are counter-propagating reference waves, while E_2 has a relative Stokes-shift in frequency. The laser signal wave E_3, as the main laser wave whose power is much greater than the reference waves, intersects E_1 at a small angle, and its conjugate wave generated by the phase conjugator is termed as E_4. All the input waves should be linearly polarized, among which E_1 is in p-polarized-state, E_2 is in s-state, and let the polarized direction of E_3 be slanted slightly, so as to share its power in s-state for a little and most of them be contained in p-state.

In order to describe these polarization states more explicit, we add letters p and s to the wave notations in Figure 77b, and term the two polarized components of E_3 as E_{3p} and E_{3s} separately. The physical picture of interaction among these waves can be depicted as follows: when encountering in the Brillouin medium, s-state E_{3s} and E_{2s} interfere with each other and drive the periodic density variations in the medium that travels from left to right at a velocity close to the velocity of sound in the medium, thus an acoustic wave ρ_{FWM} with frequency Ω is produced as a result. ρ_{FWM} acts as a moving Bragg-phase grating, once founded, it will scatter E_{1p} and generate the p-state Stokes-shifted wave E_{4p}, which is phase conjugated with the laser signal E_3. Then, as E_{4p} propagates opposite to the way of E_3, it will be Brillouin-amplified by E_{3p} that is also in the p polarized direction, and high efficiency power growth can be realized.

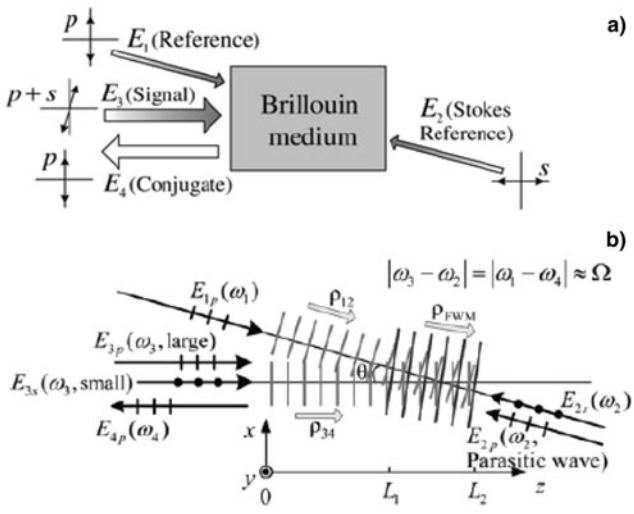

Fig. 77. Physical model of the composite-mechanism phase conjugator scheme.

There are two procedures existing in this scheme. At first, a phase conjugate wave seed is generated through Stokes-type polarization-decoupled BEFWM. Then, growth of the conjugate wave mainly depends on the SBA process. The former process provides characteristics for E_4 as high stability and fidelity, the later one ensures high conversion efficiency. In this way, advantages of BEFWM and SBS can be realized in the composite phase conjugator at the same time.

However, when ρ_{FWM} is built, waves in all polarized states will be scattered by it immediately. According to the propagating direction of ρ_{FWM}, the signal component E_{3p} might be Stokes-scattered by ρ_{FWM} and generate a Stokes-shifted wave E_{2p}, which is conjugated with E_{1p}.We call E_{2p} a parasitic wave. Here come two harmful effects from the parasitic wave. First, power in E_{3p} will be lost partly, resulting in decrease of the Brillouin amplification gain of E_{4p}. Second, E_{2p} will be Brillouin amplified by E_{1p} and therefore reduce the E_{1p} power that should be transported into E_{4p} through BEFWM process. So, how to ensure that E_{4p} have the dominance over E_{2p} during all the processes of generation and amplification is an important issue for this conjugator scheme.

14.2.2. Mathematical Model

In the following mathematical model, the acoustic waves of SBA in two different directions, i.e., E_{3p} versus E_{4p} and E_{1p} versus E_{2p}, are denoted as ρ_{34} and ρ_{12}, respectively, which propagate from left to right too. All of the six optical waves can be described by Maxwell's wave equations, and the three acoustic waves can be depicted by Navier-Stokes's energy transmission equation. Taking the interaction geometry into account as shown in Figure 77b and based on the assumption of neglecting in the second derivations, the nonlinear coupled-equations describing all the processes mentioned above along the z direction can be written as

$$\left(\cos\theta\frac{\partial}{\partial z}+\frac{n}{c}\frac{\partial}{\partial t}\right)E_{1p}=ig_o\rho_{12}E_{2p}+ig_o\rho_{FWM}E_{4p}-\frac{\alpha}{2}E_{1p}, \quad (1)$$

$$\left(-\cos\theta\frac{\partial}{\partial z}+\frac{n}{c}\frac{\partial}{\partial t}\right)E_{2s}=ig_o\rho^*_{FWM}E_{3s}\exp(i\Delta kz) \quad -\frac{\alpha}{2}E_{2s}, \quad (2)$$

https://doi.org/10.1017/S0263034611000644 Published online by Cambridge University Press

$$\left(-\cos\theta\frac{\partial}{\partial z}+\frac{n}{c}\frac{\partial}{\partial t}\right)E_{2p}=ig_o\rho_{12}^{*}E_{1p}+ig_o\rho_{FWM}^{*}E_{3p}\times\exp(i\Delta kz)-\frac{\alpha}{2}E_{2p},\quad(3)$$

$$\left(\frac{\partial}{\partial z}+\frac{n}{c}\frac{\partial}{\partial t}\right)E_{3s}=ig_o\rho_{FWM}E_{2s}\exp(-i\Delta kz)-\frac{\alpha}{2}E_{3s},\quad(4)$$

$$\left(\frac{\partial}{\partial z}+\frac{n}{c}\frac{\partial}{\partial t}\right)E_{3p}=ig_o\rho_{34}E_{4p}+ig_o\rho_{FWM}E_{2p}\times\exp(-i\Delta kz)-\frac{\alpha}{2}E_{3p},\quad(5)$$

$$\left(-\frac{\partial}{\partial z}+\frac{n}{c}\frac{\partial}{\partial t}\right)E_{4p}=ig_o\rho_{34}^{*}E_{3p}+ig_o\rho_{FWM}^{*}E_{1p}-\frac{\alpha}{2}E_{4p},\quad(6)$$

$$\left(-\frac{\partial}{\partial t}+\frac{\Gamma_B}{2}+i\Delta\Omega\right)\rho_{FWM}=ig_a(\theta)[E_{3s}E_{2s}^{*}\exp(i\Delta kz)+E_{1p}E_{4p}^{*}\cos\theta+E_{3p}E_{2p}^{*}\cos\theta\exp(i\Delta kz)],\quad(7)$$

$$\left(\frac{\partial}{\partial t}+\frac{\Gamma_B}{2}\right)\rho_{12}=ig_aE_{1p}E_{2p}^{*},\quad(8)$$

and

$$\left(\frac{\partial}{\partial t}+\frac{\Gamma_B}{2}\right)\rho_{34}=ig_aE_{3p}E_{4p}^{*},\quad(9)$$

where E and ρ are amplitudes of optical and acoustic wave, respectively; c is light velocity in the vacuum; n denotes the refractive index; $g_a(\theta)$ is the acoustic coupling coefficient with the angle θ between the optical waves, and numerically equals to $g_a\cos^2(\theta/2)$ (Aschroeder *et al.*, 1989), in which g_a is the value for $\theta=0$; Γ_B is the Brillouin line width of the medium; $\Delta\Omega=\Omega\ (\cos(\theta/2)-1)$ and $\Delta k=n\Omega(\cos\theta-1)/c$ represent, respectively, the frequency detuning and the phase mismatch of acoustic waves in BEFWM; α is the optical absorption coefficient. Compared with the light velocity, the sound velocity is so small that the propagation terms have been neglected in the three acoustic waves, Eqs. (7–9).

According to Figure 77b, E_{1p}, E_{3p}, and E_{3s} are injected at $z=0$ while E_{2s} at $z=L_2$. E_{4p} and E_{2p} equal to zero at $z=L_2$ or when $t=0$. Intensities of other optical waves will be specified as demand. Interaction length of BEFWM is limited between L_1 and L_2, and where out of this range, the gain of BEFWM equals to zero. Brillouin amplifications exist in the entire space $0\sim L_2$ along the propagation directions of E_1 and E_3. So far, all the boundary and initial conditions of the equations are defined, and the numerical simulation can be carried out.

14.2.3. Simulation and Analysis

In the numerical simulation, the laser signal is chosen as 1.06-μm wavelength and 20-ns full width at half maximum Gaussian pulses. CS_2 is chosen as the Brillouin medium (Hasi *et al.*, 2005), whose $n=1.59$, SBS gain coefficient is 68 cm/GW, the phonon lifetime is 6.4 ns, and $\alpha=4\times10^{-3}\text{cm}^{-1}$. Besides, we set the parameters as: $L_1=35$ cm, $L_2=50$ cm, $\theta=10$ mrad, the peak intensity ratio of the reference waves is $|E_{1p}|^2:|E_{2s}|^2=I_{1p}:I_{2s}=2$, and the peak intensity ratio of the two polarization components in the signal E_3 is $|E_{3p}|^2:|E_{3s}|^2=I_{3p}:I_{3s}=$ 20:1.

As mentioned above, suppression of the parasitic wave E_{2p} is important. An effective method to realize it is to decrease I_{1p} comparing with I_{3p}, i.e., to decrease the pumping intensity in the SBA process of the parasitic wave E_{2p}, so as to decrease the energy extraction ratio for E_{2p} from E_{1p}. To do this, although the initial intensity of E_{4p} generated in BEFWM will be weaker, it can be amplified to become a considerable magnitude by the high-intensity pump wave E_{3p} in the following SBA process. In Figure 78a, the simulating input pulse waveforms of E_{1p}, E_{3p}, and the output waveforms of E_{4p} and E_{2p} are shown in the same intensity scale when the injected peak intensities $I_{3p}=50\text{ MW/cm}^2$ and $I_{1p}=5\text{ MW/cm}^2$. It is easy to demonstrate that the output E_{2p} is rather weak.

Another method helping to suppress the E_{2p} pulse is to set injecting temporal delay for E_3 relative to E_1 pulse, through which, when E_3 arrives in the BEFWM region and E_{2p} is generated, there is only a tail part of the E_{1p} pulse to provide energy transferring to E_{2p} in the SBA process, which is very limited in energy and actuation duration. Nevertheless, if only the conjugate wave seed E_{4p} is generated, even though its duration of generation is short and intensity is weak, it can be amplified

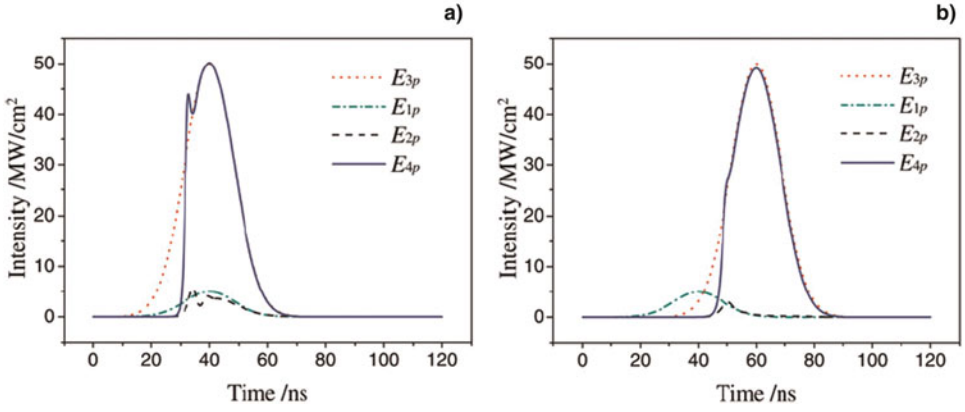

Fig. 78. (Color online) Numerical simulation on the input and output waveforms of the conjugator when the incident peak power $I_{3P}=50\text{MW/cm}^2$, $I_{1P}=5\text{ MW/cm}^2$, without signal delay (**a**), and with 20-ns signal delay (**b**).

https://doi.org/10.1017/S0263034611000644 Published online by Cambridge University Press

during the whole subsequent signal pulse span with a high gain. In Figure 78b, it is set as $I_{1p} = 5\ \mathrm{MW/cm^2}$, $I_{1p} = 50\ \mathrm{MW/cm^2}$, and E_3 is delayed by 20 ns relative to E_1. It can be seen that peak intensity of the conjugate pulse E_{4p} is close to 50 $\mathrm{MW/cm^2}$, while E_{2p} can almost be neglected.

Other parameter-contributions to the composite PC have been calculated numerically in our theoretical simulation work, and feasibility of this composite-mechanism scheme is verified in the theory. Performance of the PC, such as reflectivity will be discussed in the next section.

14.3. Experiments

14.3.1. Experimental Setup

The experimental setup is shown in Figure 79. The Nd:YLF single frequency $\mathrm{TEM_{00}}$ Q-switched laser, operating at 1-Hz repetition rate, can deliver about 120 mJ *p*-polarized-state pulses at 1053 nm in a 20-ns full width at half maximum quasi-Gaussian pulse shape. The beam diameter is about 4 mm. A $\lambda/2$ plate and polarizer P_1 are used to split the laser beam into E_1 wave, i.e., E_{1p}, and E_3 wave. After passing through the 4% sampling plate $\mathrm{SP_1}$ and the polarizer P_4, E_{1p} enters the 80-cm-length composite cell filled with $\mathrm{CS_2}$, i.e., Cell-1, and the forepart of E_{1p} pulse that transmitted throughout of Cell-1 generates backward Stokes wave in a short-focused-type SBS $\mathrm{CS_2}$ cell, i.e., Cell-2, whose lens focus equals to 10 cm and distance from Cell-1 is about 70 cm. When passing backward through the $\lambda/4$ plate, the Stokes wave is changed into *s*-polarized state, then enters into the back window of Cell-1, and acts as E_{2s}. The E_3 wave, which is reflected by the polarizer P_1 and then by P_2 turns into *p*-polarized state by a 45° rotor and a 45° Farady rotator, and penetrates through the polarizer P_3 entirely. Then it is adjusted by a $\lambda/2$ plate to contain a small *s*-state component with ratio of $I_{3p}/I_{3s} = 20$, and coupled by 20-ns delay mirrors $\mathrm{M_1}$–$\mathrm{M_6}$ into Cell-1 where BEFWM-SBA process is built up. The angle between E_1 and E_3 is about 10 mrad. The penetrated part of E_3 is obstructed by a diaphragm set behind Cell-1. The conjugate wave E_{4p} generated in Cell-1 propagates backward along the way of E_3, and finally penetrates P_2 to become the output wave. The residual E_{2s} and the parasite wave E_{2p} will propagate backward along the way of E_1. E_{2s} will be reflected off by the polarizer P_4, and E_{2p} can be blocked by the isolator.

In the experiments, we recorded the injection E_{1p} and the output of E_{2p} on the two sides of $\mathrm{SP_1}$, and recorded E_3 and E_{4p} on $\mathrm{SP_2}$ simultaneously. In order to simulate high-flux laser system, a long focus lens with $f = 300$ cm is inserted in the path of E_3 to increase the signal intensity to a certain extent in the BEFWM-SBA region, while the focus of the 300-cm lens is located out of the Cell-1 in order to avoid self excitational SBS of *E3*.

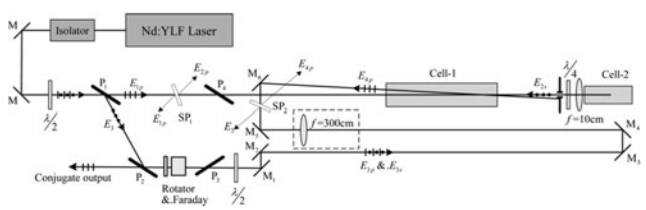

Fig. 79. Experimental setup of the BEFWM-SBA phase conjugator in demo-version.

14.3.2. Results and Discussion

Pulsed waveforms and near-field intensity patterns of the input signal E_3 and the output conjugate wave E_4 measured in experiments are shown in Figure 80. A little step, which is usually observed in the Brillouin amplification process, is shown at the root of E_4 waveform. Consistency of the in and out beam cross-sectional patterns is achieved well.

In order to research the performance of the composite phase conjugator with different laser signal power, in the experiments, we fixed the incident E_1 at 8 mJ/pulse, and varied E_3 from 6 mJ/pulse to about 82 mJ/pulse gradually by changing the applied voltages charged on the Xe-lamps of the Nd:YLF laser. It is shown that the output E_4 increases from about 3 mJ/pulse to about 61 mJ/pulse, while the parasitic E_{2p} is kept in a range between about 3 mJ/pulse and 6 mJ/pulse, as shown in Figure 81.

Reflectivity R of the composite phase conjugator is defined as energy ratio of E_4 and E_3 pulses, i.e., $R = E_4/E_3$, which have been measured synchronously using the two same calorimeters at both sides of the sampling plate $\mathrm{SP_2}$. For each measuring point, we recorded pulse energies continuously for 60 shots, and analyzed the mean value of R and its shot-to-shot fluctuations. In the discussion about, the stability of the conjugator, fluctuations of the laser itself should be taken into account, because variations in the signal can induce the change of R correspondingly. We note the relative instability of R with the symbol β, and calculate it by

$$\beta = \frac{\Delta R}{\bar{R}} = \frac{1}{\bar{R}}\left(\frac{\bar{E}_4}{\bar{E}_3}\Delta E_4 - \frac{\bar{E}_4}{\bar{E}_3^2}\Delta E_3\right)$$

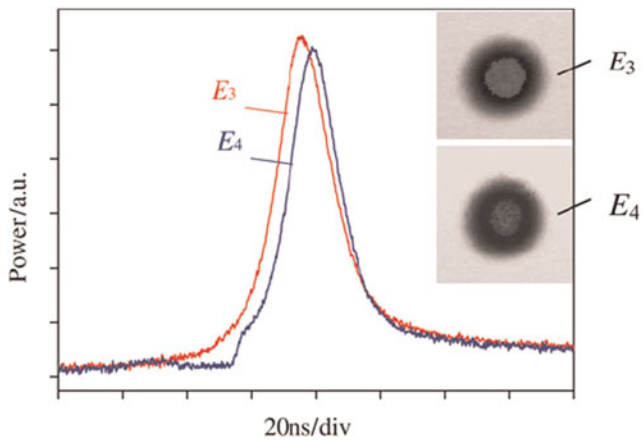

Fig. 80. (Color online) Pulsed waveforms and near-field intensity patterns of the input signal wave E_3 and the output conjugate wave E_4.

https://doi.org/10.1017/S0263034611000644 Published online by Cambridge University Press

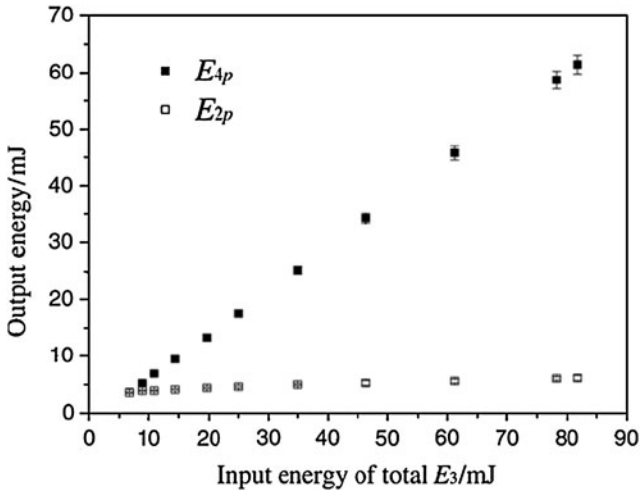

Fig. 81. Output pulse energies of E_4 and E_{2P} with different incident laser signal E_3.

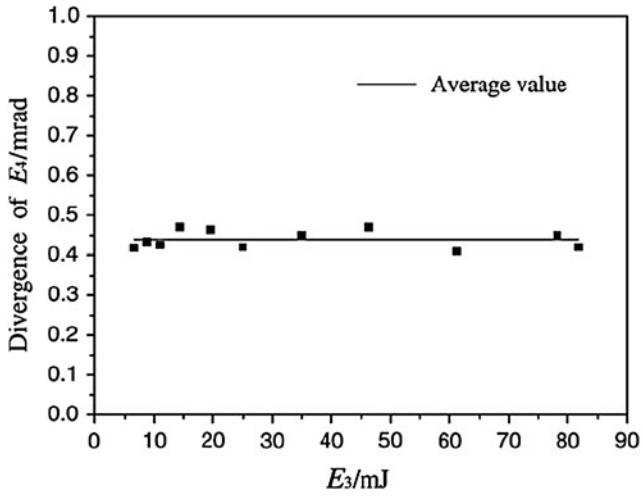

Fig. 83. Far-field divergence angles of the output conjugate wave E_4 with different incident laser signal E_3.

where the symbol with bar on the head is the mean value at a certain measuring point, and Δ denotes the standard deviation, i.e., root mean square. Figure 82a shows the experimental results of R which is as a function of E_3. The increase of E_3 induced the growth of R from 55% to a saturation value about 75%. β is shown in Figure 82b. It is seen that β is almost fixed within the range close to or below 1% during the whole variation of E_3 and at any R values, which demonstrates a very good stability.

In Figure 82a, the theoretical result is shown as a solid line. Although the tendency of which is in accordance with the experiments, it is seen obviously that the deviation occurs when E_3 is larger. In our analysis, it is attributed to incomplete polarization control for the injecting optical waves.

Far-field divergence angles of the output conjugate wave E_4 is recorded by an array camera, the result is shown in Figure 83. When the signal increases, the mean value of the divergence angles of E_4 is about 0.451 mrad, which is close to the signal divergence 0.434 mrad. In addition, the fluctuation of the output divergence angles is below 5% in the whole experimental signal range.

14.4. Conclusions

A novel BEFWM-SBA composite phase conjugator can be realized by polarization control in a compact interaction region, in which generation and amplification of the phase conjugate wave operates in BEFWM and SBA process, respectively. In this way, the advantages coming from non-noise origin of the acoustic wave and high-efficiency coupling can be achieved simultaneously very well, such as rapid response, high conjugate fidelity, high stability, and high efficiency.

Feasibility of this BEFWM-SBA mechanism is verified by the theoretical simulations and the experiments. Because almost all of the parameters are required adjustable in the demoversion experimental layout, it is seen rather complex in the structure, and a simplified version should be employed in the practical applications. For the experimental results in this work, it is estimated that the incomplete control of the polarization states is the prime reason resulting in deviations of the experimental results from that of the theory. Besides, the output performance, such as a conjugation fidelity, which can be indicated by the far-field divergence angle,

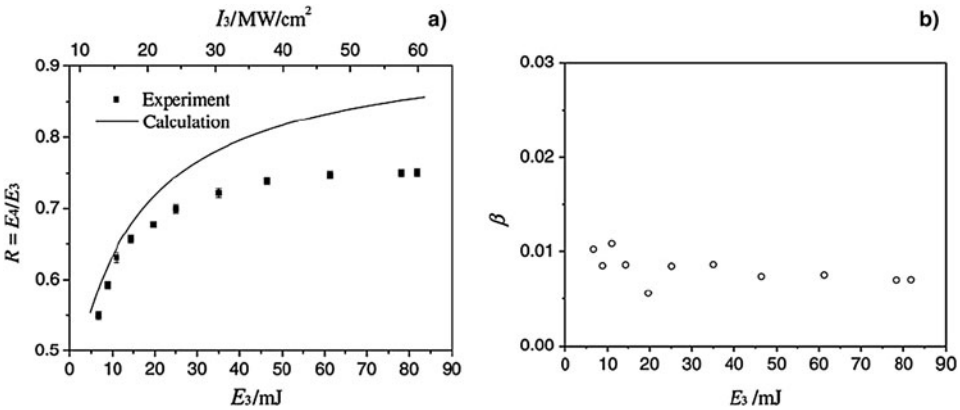

Fig. 82. Reflectivity R **(a)** and its relative instability β **(b)** with different incident laser signal E_3.

https://doi.org/10.1017/S0263034611000644 Published online by Cambridge University Press

could be influenced by so many optical elements in the experimental setup.

Significant potential performance characteristics of the composite conjugator which will be very interesting are worth to be verified and studied in the following work. For instance, the transient-state adaptabitility supported by non-noise origin of the acoustic wave, the high repeat rate laser pulses, and the high-power laser-load adaptabitility because of the non-focus structure of the composite interaction region, and so on.

ACKNOWLEDGMENT

This work was supported by the National Natural Science Foundation of China (Grant No. 61008005), the China Postdoctoral Science Foundation (Grant No. 20090450966), Special Foundation (Grant No. 201003428), the Heilongjiang Postdoctoral Science Foundation (Grant No. LBH-Z09128), Natural Scientific Research Innovation Foundation in Harbin Institute of Technology (Grant No. HIT. NSRIF. 2009010), and the Fundamental Research Funds for the Central Universities (Grant No. HIT. KLOF. 2010037).

REFERENCES

Acioli, L.H., Ulman, M., Ippen, E.P., Fujimoto, J.G., Kong, H., Chen, B.S. & Cronin-Golomb, M. (1991). Femtosecond temporal encoding in barium titanate. *Opt. Lett*. **16**, 1984.

Afshaavahid, S., Devrelis, V. & Munch, J. (1998). Nature of intensity and phase modulations in stimulated Brillouin scattering. *Phy. Rev. A*. **57**, 3961.

Akhmanov, A.S., Sukhorukov, A.P. & Khokhlov, R.V. (1968). Self-focusing and diffraction of light in a nonlinear medium. *Soviet. Phys. Usp*. **10**, 609–636.

Albach, D., Arzakantsyan, M., Bourdet, G., Chanteloup, J.-C., Hollander, Ph. & Vincent, B. (2008). Current status of the LUCIA laser system. *Phys*. **244**, 032015.

Andreev, N.F., Bespalov, V.I. & Dvoretsky, M.A. (1989). Phase conjugation of single photons. *IEEE J. Q.E*. **25**, 346–350.

Aschroeder, W., Damzen, M.J. & Hutchinson, M.H.R. (1989). Polarization-decoupled brillouin-enhanced four-wave mixing. *IEEE J. Q. E*. **25**, 460–469.

Baeva, T., Gordienko, S. & Pukhov, A. (2007). Relativistic plasma control for single attosecond pulse generation: Theory, simulations and structure of the pulse. *Laser Part. Beams* **25**, 339–346.

Bai, J.H., Shi, J.W., Ouyang, M., Chen, X.D., Gong, W.P., Jing, H.M., Liu, J. & Liu, D.H. (2008). Method for measuring the threshold value of stimulated Brillouin scattering in water. *Opt. Lett*. **33**, 1539–1541.

Baldis, H.A., Labaune, C., Moody, J.D., Jalinaud, T. & Tikhonchuk, V.T. (1998). Localization of stimulated Brillouin scattering in random phase plate speckles. *Phys. Rev. Lett*. **80**, 1900–1903.

Baldis, H.A., Villeneuve, D.M., Fontaine, B.L., Enright, G.D., Labaune, C., Baton, S., Mounaix, Ph., Pesme, D., Casanova, M. & Rozmus, W. (1993). Stimulated Brillouin scattering in picoseconds time scale: Experiments and modeling. *Phys. Fluids B* **5**, 3319–3327.

Barnes, N.P., Storm, M.E., Cross, P.L., Skolaut Jr., M.W. (1990). Efficiency of Nd laser materials with laser diode pumping. *IEEE J. Quan. Electr*. **26**, 558–569.

Basov, N. & Zubarev, I. (1979). Powerful laser systems with phase conjugation by SMBS mirror. *Appl. Phys*. **20**, 261–264.

Basov, N.G., Zubarev, L.G., Mironov, A.B., Mikhailov, S.I. & Okulov, A.Yu. (1980). Laser interferometer with wave front reversing mirrors. *Sov. Phys. JETP* **52**, 847–851.

Batanov, V.A., Goncharov, V.K. & Min'ko, L.Ya. (1972). A high-power laser plasma source. *J. Appl. Spectrosc*. **16**, 695–697.

Baton, S.D., Amiranoff, F., Malka, V., Modena, A., Salvati, M. & Coulaud, C. (1998). Measurement of the stimulated Brillouin scattering from a spatially smoothed laser beam in a homogeneous large scale plasma. *Phys. Rev. E* **57**, R4895–R4898.

Baton, S.D., Rousseaux, C., Mounaix, Ph., Labaune, C., Fontaine, B.La., Pesme, D., Renard, N., Gary, S., Jacquet, M.L. & Baldis, H.A. (1994). Stimulated Brillouin scattering with a 1 ps laser pulse in a performed underdense plasma. *Phys. Rev. E* **49**, 3602–3605.

Beak, D.H., Yoon, J.W., Shin, J.S. & Kong, H.J. (2008). Restoration of high spatial frequency at the image formed by stimulated Brillouin scattering with a prepulse. *Appl. Phys. Lett*. **93**, 231113.

Bel'dyugin, I.M., Efimkov, V.F., Mikhailov, S.I. & Zubarev, I.G. (2005). Amplification of weak stokes signals in the transient regime of stimulated Brillouin scattering. *J. Russian Laser Res*. **26**, 1–12.

Bers, A., Shkarofsky, I.P. & Shoucri, M. (2009). Relativistic Landau damping of electron plasma waves in stimulated Raman scattering. *Phys. Plasma* **16**, 022104.

Betti, R., Zhou, C., Anderson, D.K.S., Perkins, L.J., Theobald, W. & Solodov, A.A. (2007). Shock ignition of thermonuclear fuel with high areal density. *Phys. Rev. Lett*. **98**, 155001.

Beyer, O., Breunig, I., Kalkum, F. & Buse, K. (2006). Photorefractive effect in iron-doped lithium niobate crystals induced by femtosecond pulses of 1.5 μm wavelength. *Appl. Phys. Lett*. **88**, 051120.

Borghesi, M., Kar, S., Romagnani, L., Toncian, T., Antici, P., Audebert, P., Brambrink, E., Ceccherini, F., Cecchetti, C.A., Futchs, J., Galimberti, M., Gizzi, L.A., Grismayer, T., Lyseikina, T., Jung, R., Macchi, A., Mora, P., Osterholtz, J., Schiavi, A. & Willi, O. (2007). Impulsive electric fields driven by high intensity laser matter interactions. *Laser Part. Beams* **25**, 161–167.

Boyd, R.W., Rzazewski, K. & Narum, P. (1990), Noise initiation of stimulated brillouin scattering. *Phy. Rev. A* **42**, 5514–5521.

Brent, D.C., Neuman, W.A. & Hackel, L.A. (1992). Pulse-shape dependence of stimulated-Brillouin-scattering phase-conjugation fidelity for high input energies. *Opt. Lett*. **17**, 1271.

Brignon, A. & Huignard, J.P. (2003). *Phase Conjugate Laser Optics*. New York: Wiley-Interscience.

Bruckner, K.A. & Jorna, S. (1974). Laser driven fusion. *Rev. Modern Phys*. **46**, 325–367.

Chalus, O. & Diels, J.C. (2007). Lifetime of fluorocarbon for high energy f stimulated Brillouin scattering. J. *Opt. Soc. Am. B* **24**, 606–608.

Chanteloup, J.-C., Albach, D., Lucianetti, A., Ertel, K., Banerjee, S., Mason, P.D., Hernandez-Gomez, C., Collier, J.L., Hein, J., Wolf, M., Körner, J. & Le Garrec, B.J. (2010). Multi kJ level laser concepts for HiPER facility. *J. Phys*. **244**, 012010.

Chen, W.J., Hsieh, Z.M., Huang, S.W., Su, H.Y., Lai, C.J., Tang, T.T., Lin, C.H., Lee, C.K., Pan, R.P., Pan, C.L. & Kung, A.H. (2008). Sub-single-cycle optical pulse train with constant carrier envelope phase. *Phys. Rev. Lett*. **100**, 163906.

Chiao, R.Y., Townes, C.H. & Stoicheff, B.P. (1964). Stimulated Brillouin scattering and coherent generation of intense hypersonic waves. *Phys. Rev. Lett*. **12**, 592–595.

Chirokikh, A., Seka, W., Simon, A., Craxton, R.S. & Tikhonchuk, V.T. (1998). Stimulated Brillouin scattering in long-scale-length laser plasmas. *Phys. Plasmas* **5**, 1104–1109.

Clark, M.G., Disalvo, F.J., Glass, A. M. & Peterson, G.E. (1973). Electronic structure and optical index damage of iron-doped lithium niobate. *J. Chem. Phys*. **59**, 6209.

Damzen, M., Hutchinson, M. & Schroeder, W. (1987). Direct measurement of the acoustic decay times of hypersonic waves generated by SBS. *IEEE J. Quan. Electron*. **23**, 328–334.

Dane, C.B., Neuman, W.A. & Hackel, L.A. (1992). Pulse-shape dependence of stimulated-Brillouin-scattering phaseconjugation fidelity for high input energies. *Opt. Lett*. **17**, 1271–1273.

Dane, C.B., Neuman, W.A. & Hackel, L.A. (1994*a*). High-energy SBS compression. *IEEE Quan. Electron*. **QE-30**, 1907–1915.

Dane, C.B., Zapata, L.E., Neuman, W.A., Norton, M.A. & Hackel, L.A. (1994*b*). Design and operation of a 150 W near diffraction-limited laser amplifier with SBS wavefront correction. *IEEE Quan. Electron*. **QE-31**, 148–162.

Daree, K. & Kaiser, W. (1971). Competition between stimulated Brillouin and Rayleigh scattering in absorbing media. *Phys. Rev. Lett*. **26**, 816–819.

Deutsch, C., Bret, A., Firpo, M.C., Gremillet, L., Lefebrave, E. & Lifschitz, A. (2008). Onset of coherent electromagnetic structures in the relativistic electron beam deuterium–tritium fuel interaction of fast ignition concern. *Laser Part. Beams* **26**, 157–165.

Dombi, P., Racz, P. & Bodi, B. (2009). Surface plasmon enhanced electron acceleration with few cycle laser pulses. *Laser Part. Beams* **27**, 291–296.

Drake, J.F., Kaw, P.K., Lee, Y.C., Schmidt, G., Liu, C.S. & Rosenbluth, M.N. (1974). Parametric instabilities of electromagnetic waves in plasmas. *Phys. Fluids* **17**, 778–785.

Dromey, B., Bellei, C., Carroll, D.C., Clarke, R.J., Green, J.S., Kar, S., Kneip, S., Markey, K., Nagel, S.R., Willingale, L., Mckenna, P., Neely, D., Najmudin, Z., Krushelnick, K., Norreys, P.A. & Zepf, M. (2009). Third harmonic order imaging as a focal spot diagnostic for high intensity laser solid interactions. *Laser Part. Beams* **27**, 243–248.

Eichler, H.J., Konig, I.R., Piitzold, H.J. & Schwartz, J. (1995). SBS mirrors for XeCl lasers with a broad spectrum. *Appl. Phys. B* **61**, 73–80.

Eliseev, V.V., Rozmus, W., Tikhonchuk, V.T. & Capjack, C.E. (1996). Effect of diffraction on stimulated Brillouin scattering from a single laser hot spot. *Phys. Plasmas* **3**, 3754–3760.

Endo, A. (2004). High power laser plasma EUV light source for lithography. *Proc. SPIE*. **5448**, 704–711.

Erokhin, A.I., Kovalev, V.I. & FaïZullov, F.S. (1986). Determination of the parameters of a nonlinear response of liquids in an acoustic resonance region by the method of nondegenerate four-wave interaction. *Sov. J. Quan. Electr*. **16**, 872–877.

Estrabrook, E., Kruer, W.L. & Lasinski, B.F. (1980). Heating by Raman backscatter and forward scatter. *Phys. Rev. Lett*. **45**, 1399–1403.

Fernandez, J.C., Cobble, J.A., Failor, B.H., Dubois, D.F., Montgomery, D.S., Rose, H.A., Vu, H.X., Wilde, B.H., Wilde, M.D. & Chrien, R.E. (1996). Observed dependence of stimulated Raman scattering on ion-acoustic damping in hohlraum plasmas. *Phys. Rev. Lett*. **77**, 2702–2705.

Fuchs, J., Labuane, C., Depierreux, D., Baldis, H.A., Michard, A. & James, G. (2001). Experimental evidence of plasma-induced incoherence of an intense laser beam propagating in an underdense plasma. *Phys. Rev. Lett*. **86**, 432–435.

Gaeta, A.L. & Boyd, R.W. (1991). Stochastic dynamics of stimulated Brillouin scattering in an optical fiber. *Phys. Rev. A* **44**, 3205–3209.

Gao, W., Lu, Z.W., He, W. M., Dong, Y.K. & Hasi, W.L.J. (2009). Characteristics of amplified spectrum of a weak frequencydetuned signal in a Brillouin amplifier. *Laser Part. Beams* **27**, 465–470.

Gao, W., Lu, Z.W., He, W. M., Hasi, W.L.J. & Zhang, Z. (2008). Spectrum evolution of spontaneous and pump-depleted stimulated Brillouin scattering in liquid media. *Chin. Phys*. **17**, 3765–3770.

Giulietti, A., Macchi, A., Schifano, E., Biancalana, V., Danson, C., Giulietti, D., Gizzi, L.A. & Willi, O. (1999). Stimulated Brillouin scattering from underdense expending plasma in a regime of strong filamentation. *Phys. Rev. E* **59**, 1038–1046.

Gong, S., Hasi, W.L.J., Lu, Z.W., Dong, F.L., Lin, D.Y., He, W.M., Zhao, X.Y. & Fan, R.Q. (2009). Study on the choosing principles of SBS new medium perfluoro-compound for phase conjugation mirror and optical limiter. *Acta Phys. Sin*. **58**, 304–308.

Grassi, W. & Testi, D. (2008). Transitional mixed convection in the entrance region of a horizontal pipe. *5th European Thermal-Sciences Conference*, Eindhoven, The Netherlands.

Grofts, G.J., Damzen, M.J. & Lamb, R.A. (1991). Experimental and theoretical investigation of two-cell stimulated-Brillouinscattering systems. *J. Opt. Soc. Am. B* **8**, 2282–2288.

Han, K.G. & Kong, H.J. (1995). Four-pass amplifier system compensation thermally induced birefringence effect, using a novel dumping mechanism. *Jpn. J. Appl. Phys*. **34**, 994–996.

Hase, M., Itano, T., Mizoguchi, K. & Nakashima, S. (1998). Selective enhancement of coherent optical phonons using THz-rate pulse train. *Jpn. J. Appl. Phys*. **37**, L281–L283.

Hasi, W.L.J., Gong, S., Lu, Z.W., Lin, D.Y., He, W.M. & Fan, R.Q. (2008*b*). Generation of flat-top waveform in the time domain based on stimulated Brillouin scattering using medium with short phonon lifetime. *Laser Part. Beams* **26**, 511–516.

Hasi, W.L.J., Guo, X.Y., Lu, H.H., Fu, M.L., Gong, S., Geng, X.Z., Lu, Z.W., Lin, D.Y. & He, W.M. (2009*c*). Investigation on effect of medium temperature upon SBS and SBS optical limiting. *Laser Part. Beams* **27**, 733–737.

Hasi, W.L.J., Lu, Z.W., Fu, M.L., Lu, H.H., Gong, S., Lin, D.Y. & He, W.M. (2009*a*). Improved output energy characteristic of optical limiting based on double stimulated Brillouin scattering. *Appl. Phys. B* **95**, 711–714.

Hasi, W.L.J., Lu, Z.W., Fu, M.L., Lu, H.H., Gong, S., Lin, D.Y. & He, W.M. (2009*b*). Investigation of optical limiting based on the combination of stimulated Brillouin scattering and carbon nanotube/HT-270 suspension. *Laser Part. Beams* **27**, 533–536.

Hasi, W.L.J., Lu, Z.W., Gong, S., Li, Q., Lin, D.Y. & He, W.M. (2008*c*). Investigation on output energy characteristic of optical limiting based on the stimulated Brillouin scattering. *Appl. Phys. B* **92**, 599–602.

Hasi, W.L.J., Lu, Z.W., Gong, S., Liu, S.J., Li, Q. & He, W.M. (2008*a*). Investigation on new SBS media of Perfluorocompound and Perfluoropolyether with low absorption coefficient and high power-load ability. *Appl. Opt*. **47**, 1010–1014.

Hasi, W.L.J., Lu, Z.W., He, W.M. & Wang, S.Y. (2005). Study on Brillouin amplification in different liquid media. *Acta Phys. Sin*. **54**, 742–748 (in Chinese).

Hasi, W.L.J., Lu, Z.W., Li, Q. & He, W.M. (2007). Research on the enhancement of power-load of two-cell SBS system by choosing different media or mixture medium. *Laser Part. Beams* **25**, 207–210.

Hasi, W.L.J., Lu, Z.W., Liu, S.J., Li, Q., Yin, G.H. & He, W.M. (2008*d*). Generation of flat-top waveform in the time domain based on stimulated Brillouin scattering. *Appl. Phys. B* **90**, 503–506.

Hoffmann, D.H.H., Blazevic, A., Ni, P., Rosmej, O., Roth, M., Tahir, N.A., Tauschwitz, A., Udrea, S., Varentsov, D., Weyrich, K. & Maron, Y. (2005). Present and future perspectives for high energy density physics with intense heavy ion and laser beams. *Laser Part. Beams* **23**, 47–53.

Horowitz, M. & Fischer, B. (1996). Photorefractive effect in a $BaTiO_3$ crystal at the 1.5-μm wavelength regime by two-photon absorption. *Opt. Lett*. **21**, 1120–1122.

Hüller, S. (1991). Stimulated Brillouin scattering off non-linear ion acoustic waves. *Phys.Fluids B* **3**, 3317–3330.

Hüller, S., Masson-Laborde, P.E., Pesme, D., Labaune, C. & Bandulet, H. (2008). Modeling of stimulated Brillouin scattering in expanding plasma. *J. Phys*. **112**, 022031.

Ikesue, A. (2002). Polycrystalline Nd:YAG ceramics lasers. *Opt. Mater*. **19**, 183–187.

Jain, R.K. & Stenersen, K. (1984). Picosecond pulse operation of a dye laser containing a phase-conjugate mirror. *Opt. Lett*. **9**, 546.

Jakeman, E. & Ridely, K.D. (1996). Incomplete phase conjugation through a random phase screen. I. Theory. *J. Opt. Soc. Am. A* **13**, 2279–2287.

Jermann, F., Simon, M. & Krätzig, E. (1995). Photorefractive properties of congruent and stoichiometric lithium niobate at high light intensities. *J. Opt. Soc. Am. B* **12**, 2066.

Jiang, Z., Huang, C.-H., Leaird, D.E. & Weiner, A.M. (2007). Optical arbitrary waveform processing of more than 100 spectral comb lines. *Nat. Photon*. **1**, 463–467.

Jin, F. & Richardson, M. (1995). New laser plasma source for extreme-ultraviolet lithography. *Appl. Opt*. **34**, 5750–5760.

Joubert, C., Roblin, M.L. & Grousson, R. (1989). Temporal reversal of picosecond optical pulses by holographic phase conjugation. *Appl. Opt*. **28**, 4604.

Kalal, M., Kong, H.J., Martinkova, M., Slezak, O. & Yoon, J.W. (2008*a*), Current status of designing SBS PCM based IFE driver. *30th European Conference on Laser Interaction with Matter*. August 31-September 5, Darmstadt, Germany.

Kalal, M., Kong, H.J., Martinkova, M., Slezak, O. & Yoon, J.W. (2010*a*). SBS PCM technique applied for aiming at IFE pellets: First tests with amplifiers and harmonic conversion. *J. Kor. Phys. Soc*. **56**, 184–189.

Kalal, M., Kong, H.J., Slezak, O. & Yoon, J.W. (2008*b*). Some issues in development of SBS PCM based IFE driver. *3rd Workshop on SBS and Phase Conjugation*. August 25-26, Harbin, China.

Kalal, M., Kong, H.J., Slezak, O., Koresheva, E.R., Park, S. & Startsev, S.A. (2010*b*). Recent Progress Made in the SBS PCM Approach to Self-navigation of Lasers on Direct Drive IFE Targets. *J. Fusion Ener*. **29**, 527–531.

Kalal, M., Kong, J.H. & Alexander, N.B. (2007*a*). Consideration of SBS PCM technique for self-aiming of laser fusion drivers on IFE targets proposal and feasibility study. *3rd International Conference on the Frontiers of Plasma Physics and Technology*. March 5–9, Bangkok, Thailand.

Kalal, M., Martinkova, M., Slezak, O., Kong, H.J. & Alexander, N.B. (2007*b*). SBS PCM technique and its possible role in achieving IFE objectives. *J. Phys*. **112**, 032049.

Kanaka, Raju, P., Suzuki, T., Suda, A., Midorikawa, K. & Katsuragawa, M. (2010). Line-by-line control of 10-THz-frequency spacing Raman sidebands. *Opt. Expr*. **18**, 732–739.

Kappe, P., Strasser, A. & Ostermeyer, M. (2007). Investigation of the impact of SBS- parameters and loss modulation on the mode locking of an SBS-laser oscillator. *Laser Part. Beams* **25**, 107–116.

Katsuragawa, M. & Onose, T. (2005). Dual-wavelength injection-locked pulsed laser. *Opt. Lett*. **30**, 2421–2423.

Katsuragawa, M., Yokoyama, K., Onose, T. & Misawa, K. (2005). Generation of a 10.6-THz ultrahigh-repetition-rate train by synthesizing phase-coherent Raman-sidebands. *Opt. Expr*. **13**, 5628–5634.

Kaw, P.K., Schmidt, G. & Wilcox, T. (1973). Filamentation and trapping of electromagnetic radiation in plasmas. *Phys. Fluids* **16**, 1522–1525.

Kawanaka, J., Takeuchi, Y., Yoshida, A., Pearce, S. J., Yasuhara, R., Kawashima, T. & Kan, H. (2010). Highly efficient cryogenically-cooled Yb:YAG laser. *Laser Phys*. **20**, 1079–1084.

Kline, J.L., Montgomery, D.S., Rousseaux, C., Baton, S.D., Tassin, V., Hardin, R.A., Flippo, K.A., Johnson, R.P., Shimada, T., Yin, L., Albright, B.J., Rose, H.A. & Amiranoff, F. (2009). Investigation of stimulated Raman scattering using a short-pulse diffraction limited laser beam near the instability threshold. *Laser Part. Beams* **27**, 185–190.

Kmetik, V., Fiedorowics, H., Andreev, A.A., Witte, K.J., Daido, H., Fujita, H., Nakatsuka, M. & Yamanaka, T. (1998). Reliable stimulated Brillouin scattering compression of Nd:YAG laser pulses with liquid fluorocarbon for long-time operation at 10 Hz. *Appl. Opt*. **37**, 7085–7090.

Kong, H.J., Beak, D.H., Lee, D.W. & Lee, S.K. (2005*a*). Wave form preservation of the backscattered stimulated Brillouin scattering wave by using a Pre-pulse injection. *Opt. Lett*. **30**, 3401–3403.

Kong, H.J., Lee, J.Y., Shin, Y.S., Byun, J.O., Park, H.S. & Kim, H. (1997). Beam recombination characteristics in array laser amplification using stimulated Brillouin scattering phase conjugation. *Opt. Rev*. **4**, 277–283.

Kong, H.J., Lee, S.K. & Lee, D.W. (2005*b*). Beam combined laser fusion driver with high power and high repetition rate using stimulated Brillouin scattering phase conjugation mirrors and self-phase-locking. *Laser Part. Beams* **23**, 55–59.

Kong, H.J., Lee, S.K. & Lee, D.W. (2005*c*). Highly repetitive high energy/power beam combination laser: IFE laser driver using independent phase control of stimulated Brillouin scattering phase conjugate mirrors and pre-pulse technique. *Lasers Part. Beams* **23**, 107–111.

Kong, H.J., Lee, S.K., Lee, D.W. & Guo, H. (2005*d*). Phase control of a stimulated Brillouin scattering phase conjugate mirror by a self-generated density modulation. *Appl. Phys. Lett*. **86**, 051111.

Kong, H.J., Shin, J.S., Yoon, J.W. & Beak, D.H. (2009*a*). Phase stabilization of the amplitude dividing four-beam combined laser system using stimulated Brillouin scattering phase conjugate mirrors. *Laser Part. Beams* **27**, 179–184.

Kong, H.J., Shin, J.S., Yoon, .J.W. & Beak, D.H. (2009*b*). Wavefront dividing beam combined laser fusion driver using stimulated Brillouin scattering phase conjugation mirrors. *Nucl. Fusion* **49**, 125002.

Kong, H.J., Yoon, J.W., Beak, D.H., Shin, J.S., Lee, S.K. & Lee, D.W. (2007*a*). Laser fusion driver using stimulated Brillouin scattering phase conjugate mirrors by a self-density modulation. *Laser Part. Beams* **25**, 1–14.

Kong, H.J., Yoon, J.W., Beak, D.H., Shin, J.S., Lee, S.K. & Lee, D.W. (2007*b*). Laser fusion driver using stimulated Brillouin scattering phase conjugate mirrors by a self-density modulation. *Laser Part. Beams* **25**, 225–238.

Kong, H.J., Yoon, J.W., Shin, J.S. & Beak, D.H. (2008). Long-term stabilized two-beam combination laser amplifier with stimulated Brillouin scattering mirrors. *Appl. Phys. Lett*. **92**, 021120,

Kong, H.J., Yoon, J.W., Shin, J.S., Beak, D.H. & Lee, B.J. (2006). Long-term stabilization of the beam combination laser with a phase controlled mirror for laser fusion driver. *Laser Part. Beams* **24**, 519–523.

Kovalev, V.I. & Harrison, R.G. (2007). Threshold for stimulated Brillouin scattering in optical fiber. *Opt. Expr*. **15**, 17625–17630.

Kovalev, V.I., Kotova, N.E. & Harrison, R.G. (2009). "Slow Light" in stimulated Brillouin scattering: On the influence of the spectral width of pump radiation on the group index. *Opt. Expr*. **17**, 17317–17323.

Krall, N.A. & Trivelpiece, A.W. (1973). *Principle of Plasma Physics*. Tokyo: McGraw Hill-Kogakusha.

Kruer, W.L. (2000). Interaction of plasmas with intense laser. *Phys. Plasma* **7**, 2270–2278.

Lagemann, R.T., Woolf, W.E., Evans, J.S. & Underwood, N. (1948). Ultrasonic Velocity in Some Liquid Fluorocarbons. *J. Am. Chem. Soc*. **70**, 2994–2996.

Lanzerotti, M.Y., Schirmer, R.W. & Gaeta, A.L. (1996). Phase conjugation of weak continuous-wave optical signals. *Phys. Rev. Lett*. **77**, 2202–2205.

Laska, L., Jungwirth, K., Krasa, J., Krousky, E., Pfeifer, M., Rohlena, K., Velyhan, A., Ullschmied, J., Gammino, S., Torrisi, L., Badziak, J., Parys, P., Rosinski, M., Ryc, L. & Wolowski, J. (2008). Angular distribution of ions emitted from laser plasma produced at various irradiation angles and laser intensities. *Laser Part. Beams* **26**, 555–565.

Lee, S., Choi, D., Kim, C. J. & Zhou, J. (2007), Highly efficient diode side-pumped Nd:YAG ceramic laser with 210 W output power *Opt. Laser Techn*. **39**, 705–709.

Lee, S.K., Kong, H.J. & Nakatsuka, M. (2005*a*). Great improvement of phase controlling of the entirely independent stimulated Brillouin scattering phase conjugate mirrors by balancing the pump energies. *Appl. Phys. Lett*. **87**, 161109.

Lee, S.K., Lee, D.W. & Kong, H.J. (2005*b*). Stimulated Brillouin scattering by a multimode pump with alarge number of longitudinal modes. *J. Korean Phys. Soc*. **46**, 443–447.

Levis, R.J., Menkir, G.M. & Rabitz, H. (2001). Selective bond dissociation and rearrangement with optimally tailored, strong-field laser pulses. *Sci*. **292**, 709–713.

Liang, J.Q., Katsuragawa, M., Kien, F.L. & Hakuta, K. (2000). Sideband generation using strongly driven Raman coherence in solid hydrogen. *Phys. Rev. Lett*. **85**, 2474–2477.

Limpert, J., Deguil-Robin, N., Manek-Hönninger, I., Salin, F., Röser, F., Liem, A., Schreiber, T., Nolte, S., Zellmer, H., Tünnermann, A., Broeng, J., Petersson, A. & Jakobsen, C. (2005). High-power rod-type photonic crystal fiber laser. *Opt. Exp*. **13**, 1055–1058.

Loree, T.R., Watkins, D.E., Johnson, T.M., Kurnit, N.A. & Fisher, R.A. (1987). Phase locking two beams by means of seeded Brillouin scattering. *Opt. Lett*. **12**, 178–180.

Lu, Z.W., Dong, Y.K. & Li, Q. (2007). Slow light in multi-line Brillouin gain spectrum. *Opt. Exp*. **15**, 1871–1877.

Lu, Z.W., Gao, W., He, W.M., Zhang, Z. & Hasi, W.L.J. (2009). High amplification and low noise achieved by a double-stage non-collinear Brillouin amplifier. *Opt. Expr*. **17**, 10675–10680.

Maier, M. & Renner, G. (1971). Transient and quasistationary stimulated scattering of light. *Opt. Commun*. **3**, 301–304.

Mao, J.S., Zhao, J.Y., Li, Y.D., Xie, A.G., Fang, Z.S., Sannikov, V. & Gorshkov, A. (2001). HT-7 multipoint Nd laser Thomson scattering apparatus. *Plasma Sci. Techn*. **3**, 691–702.

Masse, J.E. & Barreau, G. (1995). Laser generation of stress waves in metal. *Surf. Coatings Techn*. **70**, 231–234.

Mccrory, R.L., Meyerhofer, D., Betti, D.R., Craxton, R., Delettrez, S.J.A., Edgell, D.H., Glebov, V.Yu., Goncharov, V.N., Harding, D.R., Jacobs-Perkins, D.W., Knauer, J.P., Mars Hall, F.J., Mckenty, P.W., Radha, P.B., Regan, S.P., Sangster, T.C., Seka, W., Short, R.W., Skupsky, S., Smalyuk, V.A., Soures, J.M., Stoeckl, C., Yaakobi, B., Shvarts, D., Frenje, J.A., Li, C.K., Petrasso, R.D. & Séguin, F.H. (2008). Progress in direct-drive inertial confinement fusion. *Phys. Plasmas* **15**, 055503.

Meister, S., Riesbeck, T. & Eichler, H.J. (2007). Glass fibers for stimulated Brillouin scattering and phase conjugation. *Laser Part. Beams* **25**, 15–21.

Miley, G.H., Hora, H., Osman, F., Evans, P. & Toups, P. (2005). Single event laser fusion using ns-MJ laser pulses. *Laser Part. Beams* **23**, 453–460.

Mitra, A., Yoshida, H., Fujita, H. & Nakatsuka, M. (2006). Sub nanosecond pulse generation by stimulated Brillouin scattering using FC-75 in an Integrated set-up with laser energy up to 1.5 J. *Jpn. J. Appl. Phys*. **45**, 1607–1611.

Miyamoto, R.Y. & Itoh, T. (2002) Retro directive arrays for wireless communications. *IEEE Microwave Mag*. **3**, 67–72.

Moses, E.I (2009). Ignition on the National Ignition Facility: A path towards inertial fusion energy. *Nucl. Fusion* **49**, 104022.

Myatt, J., Pesme, D., Huller, S., Maximov, A.V., Rozmus, W. & Capjack, C.E. (2001). Nonlinear propagation of a randomized laser beam through an expanding plasma. *Phys. Rev. Lett*. **87**, 255003.

Omatsu, T., Minassian, A. & Damzen, M.J. (2002). High quality 7.5 W continuous-wave operation of a Nd:YVO4 laser with a Rh:BaTiO3 phase conjugate mirror. *Jpn. J. Appl. Phys*. **41**, 2024–2027.

Ostermeyer, M., Kong, H.J., Kovalev, V.I., Harrison, R.G., Fotiadi, A.A., Megret, P., Kalal, M., Slezak, O., Yoon, J.W., Shin, J.S., Beak, D.H., Lee, S.K., Lu, Z., Wang, S., Lin, D., Knight, J.C., Kotova, N.E., Straber, A., Scheikhobeid, A., Riesbeck, T., Meister, S., Eichler, H.J., Wang, Y., He, W., Yoshida, H., Fujita, H., Nakatsuka, M., Hatae, T., Park, H., Lim, C., Omatsu, T., Nawata, K., Shiba, N., Antipov, O.L., Kuznetsov, M.S. & Zakharov, N.G. (2008). Trends in stimulated Brillouin scattering and optical phase conjugation. *Laser Part. Beams* **26**, 297–362.

Ozoki, T., Bom Elouga, L.B., Ganeev, R., Kieffer, J.C., Sazuki, M. & Kuroda, H. (2007). Intense harmonic generation from silver ablation. *Laser Part. Beams* **25**, 321–325.

Park, H., Lim, C., Yoshida, H. & Nakatsuka, M. (2006). Measurement of stimulated Brillouin scattering characteristics in heavy fluorocarbon liquids and perfluoropolyether liquids. *Jpn. J. Appl. Phys*. **45**, 5073–5075.

Pettazzi, F., Alonzo, M., Centini, M., Petris, A., Vlad, V. I., Chauvet, M. & Fazio, E. (2007). Self-trapping of low-energy infrared femtosecond beams in lithium niobate. *Phys. Rev. A*. **76**, 063818.

Pohl, D. & Kaiser, W. (1970). Time-resolved investigations of stimulated Brillouin scattering in transparent and absorbing media: Determination of phonon lifetimes. *Phys. Rev. B* **1**, 31–43.

Roblin, M.L., Gires, F., Grousson, R. & Lavallard, P. (1987). Enregistrement par holographie de volume d'une loi de phase spectrale: Application a la compression d'impulsion picoseconde. *Opt. Commun*. **62**, 209.

Rockwell, D.A. (1988). A review of phase-conjugate solid-state lasers *IEEE J. Quan. Electron*. **24**, 1124–1140.

Rosas, E., Aboites, V. & Damzen, M.J. (1998). Transient evolution and spatial mode size analysis of adaptive laser oscillators. *Opt. Commun*. **156**, 419–425.

Rozmus, W., Sharma, R.P., Samson, J.C. & Tighe, W. (1987). Nonlinear evolution of stimulated Raman scattering in homogeneous plasmas. *Phys Fluids* **30**, 2181–2193.

Salamin, Y.I., Harman, Z. & Keitel, C.H. (2008). Direct high-power laser acceleration of ions for medical applications. *Phys. Rev. Lett*. **100**, 155004.

Salamin, Y.I., Hu, S.X., Hatsagortsyan, K.Z. & Keitel, C.H. (2006). Relativistic high-power laser–matter interactions. *Phys. Rept*. **427**, 41–155.

Schäfer, C.A. (2010). Continuous adaptive beam pointing and tracking for laser power transmission. *Opt. Expr*. **18**, 13451–13468.

Schiemann, S., Ubachs, W. & Hogervorst, W. (1997). Efficient temporal compression of coherent nanosecond pulses in a compact SBS generator-amplifier setup. *IEEE J. Quan. Electron*. **33**, 358–366.

Scott, A.M. & Ridley, K.D. (1989). A review of Brillouin enhanced four-wave mixing. *IEEE J. Q.E*. **25**, 438–459.

Sen, P. & Sen, K. (1986). Correlation and competition between stimulated Raman and Brillouin scattering processes. *Phys. Rev. B*. **33**, 1427–1429.

Shahraam, A., Vladimyros, D. & Jesper, M. (1998). Nature of intensity and phase modulations in stimulated Brillouin scattering. *Phys. Rev. A*. **57**, 3961–3971.

Shin, J.S., Park, S. & Kong, H.J. (2010*a*), Compensation of the thermally induced depolarization in a double-pass Nd:YAG rod amplifier with a stimulated Brillouin scattering phase conjugate mirror. *Opt. Commun*. **283**, 2402–2405.

Shin, J.S., Park, S., Kong, H.J. & Yoon, J.W. (2010*b*). Phase stabilization of a wave-front dividing four-beam combined amplifier with stimulated Brillouin scattering phase conjugate mirrors. *Appl. Phys. Lett*. **96**, 131116.

Shuangyi, W., Zhiwei, L., Dianyang, L., Lei, D. & Dongbin, J. (2007). Investigation of serial coherent laser beam combination based on Brillouin amplification. *Laser Part. Beams* **25**, 79–83.

Shverdin, M.Y., Walker, D.R., Yavuz, D.D., Yin, G.Y. & Harris, S.E.. (2005). Generation of a single-cycle optical pulse. *Phys. Rev. Lett*. **94**, 033904–033907.

Siegman, A.E. (1986). *Lasers*. Mill Valley: University Science Books.

Sodha, M.S., Mishra, S.K. & Mishra, S. (2009). Focusing of dark hollow Gaussian electromagnetic beams in a plasma. *Laser Part. Beams* **27**, 57–68.

Sodha, M.S., Ghatak, A.K. & Tripathi, V.K. (1976). Self focusing of laser beams in plasmas and semiconductors. *Prog. Opt. E* **3**, 169–265.

Sokolov, A.V., Walker, D.R., Yavuz, D.D., Yin, G.Y. & Harris, S.E. (2000). Raman generation by phased and anti phased molecular states. *Phys. Rev. Lett*. **85**, 562–565.

Spalding, I.J. (1978). High power lasers next term for previous term processing of materials next term — A comparison of available systems. *Opt. Laser Techn*. **10**, 29–32.

Steinsiek, F., Foth, W.P., Weber, K.H., Schäfer, C.A. & Foth, H.J. (2003). Wireless power transmission experiment as an early contribution to planetary exploration missions. *Proc. 54th International Astronautical Congress*, IAC-03-R.3.06. Bremen, Germany.

Sternklar, S., Glick, Y. & Jackel, S. (1992). Noise limitations of Brillouin two-beam coupling: theory and experiment. *J. Opt. Soc. Am. B*. **9**, 391–397.

Suda, A., Oishi, Y., Nagasaka, K., Wang, P. & Midorikawa, K. (2001). A spatial light modulator based on fused-silica plates for adaptive feedback control of intense femtosecond laser pulses. *Opt. Expr*. **9**, 2–6.

Sumiyoshi, T., Sekita, H., Arai, T., Sato, S., Ishihara, M. & Kikuchi, M. (1999). High-power continuous-wave 3- and 2-μm cascade Ho3+: ZBLAN fiber laser and its medical applications. *IEEE J. Quan. Electron*. **5**, 936–943.

Suzuki, T., Hirai, M. & Katsuragawa, M. (2008*a*). Octave-spanning Raman comb with carrier envelope offset control. *Phys. Rev. Lett*. **101**, 243602.

Suzuki, T., Sawayama, N. & Katsuragawa, M. (2008*b*). Spectral phase measurements for broad Raman sidebands by using spectral interferometry. *Opt. Lett*. **33**, 2809–2811.

Tajima, T. & Dawson, J.M. (1979). Laser electron Accelerator. *Phys. Rev. Lett*. **43**, 267–270.

Tesla, N. (1904). The transmission of electrical energy without wires. *Elec. World Eng*. **35**, 429–431.

Thareja, R.K. & Sharma, A.K. (2006). Reactive pulsed laser ablation: Plasma studies. *Laser Part. Beams* **24**, 311–320.

Udaiyan, D., Crofts, G.J., Omatsu, T. & Damzen, M.J. (1998). Self-consistent spatial mode analysis of self-adaptive laser oscillators. *J. Opt. Soc. Am. B* **15**, 1346–1352.

Veiko, V.P., Shakhno, E.A., Smirnov, V.N., Miaskovski, A.M. & Nikishin, G.D. (2006). Laser-induced film deposition by LIFT: Physical mechanisms and applications. *Laser Part. Beams* **24**, 203–209.

Von Der Linde, D., Glass, A.M. & Rodgers, K.F. (1974). Multiphoton photorefractive processes for optical storage in LiNbO3. *Appl. Phys. Lett*. **25**, 155–157.

Wang, S.Y., Lu, Z.W., Lin, D.Y., Ding, L. & Jiang, D.B. (2007). Investigation of serial coherent laser beam combination based on Brillouin amplification. *Laser Part. Beams* **25**, 79–83.

Wang, Y.L., Lu, Z.W., He, W.M., Zheng, Z.X. & Zhao, Y.H. (2009*a*). A new measurement of stimulated Brillouin scattering

phase conjugation fidelity for high pump energies. *Laser Part. Beams* **27**, 297–302.

Wang, Y.L., Lu, Z.W., Li, Y., Wu, P., Zheng, Z.X. & He, W.M. (2010). Investigation on high-power load ability of stimulated Brillouin scattering phase conjugating mirror. *Appl. Phys. B* **98**, 391–395.

Wang, Y.L., Lu, Z.W., Wang, S.Y., Zheng, Z.X., He, W.M. & Lin, D.Y. (2009*b*). Investigation on efficiency of non-collinear serial laser beam combination based on Brillouin amplification. *Laser Part. Beams* **27**, 651–655.

Weaver, M.A.S.E. (2009). Efficient cooling of lasers, LEDs and photonics devices. Patent (IPC8 Class: AF21V2900FI).

Yang, A.L., Yang, J.G., Ding, L., Li, M.Z., Zhang, X.M. & Mang, Y.Z. (2001). Phase Jump in the Process of Stimulated Brillouin Scattering. *Chinese J. Lasers* **28**, 732–734.

Yao, X.S. & Feinberg, J. (1993). Temporal shaping of optical pulses using beam coupling in a photorefractive crystal. *Opt. Lett*. **18**, 622.

Yasuhara, R., Kawashima, T., Sekine, T., Kurita, T., Ikegawa, T., Matsumoto, O., Miyamoto, M., Kan, H., Yoshida, H., Kawanaka, J., Nakatsuka, M., Miyanaga, N., Izawa, Y. & Kanabe, T. (2008). 213 W average power of 2.4 GW pulsed thermally controlled Nd:glass zigzag slab laser with a stimulated Brillouin scattering mirror. *Opt. Lett*. **33**, 1711–1713.

Yau, H., Wang, P., Pan, E., Chen, J. & Chang, J.Y. (1997). Self-pumped phase conjugation with picosecond and femtosecond pulses using BaTiO3. *Opt. Commun*. **135**, 331.

Yoon, J.W., Shin, J.S., Kong, H.J. & Lee, J. (2009). Investigation of the relationship between the prepulse energy and the delay time in the waveform preservation of a stimulated Brillouin scattering wave by prepulse injection. *J. Opt. Soc.Am. B* **26**.

Yoshida, H., Fujita, H., Nakatsuka, M. & Fujinoki, A. (2004). Temporal Compression by Stimulated-Brillouin-Scattering of Q-switched Pulse with Fused Quartz Glass. *Jpn. J. Appl. Phys*. **43**, 1103–1105.

Yoshida, H., Fujita, H., Nakatsuka, M. & Yoshida, K. (1999). High resistant phase-conjugated stimulated Brillouin scattering mirror using fused-silica glass for Nd:YAG laser system. *Jpn. J. Appl. Phys*. **38**, 521–523.

Yoshida, H., Fujita, H., Nakatsuka, M., Fujinoki, A. & Yoshida, K. (2003). Fused-quartz glass with low optical quality as a high damage-resistant stimulated Brillouin-scattering phase-conjugation mirror. *Opt. Commun*. **222**, 257–267.

Yoshida, H., Fujita, H., Nakatsuka, M., Ueda, T. & Fujinoki, A. (2007). Temporal compression by stimulated Brillouin scattering of Q-switched pulse with fused-quartz and fused-silica glass from 1064 nm to 266 nm wavelength. *Laser Part. Beams* **25**, 481–488.

Yoshida, H., Hatae, T., Fujita, H., Nakatsuka, M. & Kitamura, S. (2009). A high-energy 160-ps pulse generation by stimulated Brillouin scattering from heavy fluorocarbon liquid at 1064 nm wavelength. *Opt. Expr*. **17**, 13654–13662.

Yoshida, H., Hataeh, T., Fujita, H., Nakatsuka, M. & Kitamura, S. (2010). A High-energy 160-ps Pulse Generation by Stimulated Brillouin Scattering from Heavy Fluorocarbon Liquid at 1064 nm Wavelength. *Opt. Expr*. **17**, 13654–13662.

Yoshida, H., Kmetik, V., Fujita, H., Nakatsuka, M., T. Yamanaka, T. & Yoshida, K. (1997). Heavy fluorocarbon liquids for a phase-conjugated stimulated Brillouin scattering mirror. *Appl. Opt*. **36**, 3739–3744.

Young, P.E., Baldis, H.A., Drake, R.P., Campbell, E.M. & Estrabrook, K.G. (1988). Direct evidence of ponderomotive Filamentation in laser-produced plasma. *Phys. Rev. Lett*. **61**, 2336–2339.

Zel'dovich, B.Ya., Pilipetskii, N.F. & Shkunov, V.V. (1982). Phase conjugation in stimulated scattering. *Sov. Phys. Usp*. **25**, 713–737.

Zel'dovich, B.Ya., Popovichev, V.I., Ragulsky, V.V. & Faizullov, F.S. (1972). Connection between the wave fronts of the reflected and exciting light in stimulated Mandel'shtam Brillouin scattering. *Sov. Phys. JETP* **15**, 109–112.

Zheng, W., Zhang, X., Wei, X., Jing, F., Sui, Z., Zheng, K., Yuan, X., Jiang, X., Su, J., Zhou, H., Li, M., Wang, J., Hu, D., He, S., Xiang, Y., Peng, Z., Feng, B., Guo, L., Li, X., Zhu, Q., Yu, H., You, Y., Fan, D. & Zhang, W. (2008), Status of the SG-III solid-state laser facility, *Journal of Physics: Conference Series* 112 032009

Zhou, B., Kane, T. J., Dixon, G. J. & Byer, R.L. (1985). Efficient, frequency-stable laser-diode-pumped Nd:YAG laser. *Opt. Lett*. **10**, 62–64.

Zhu, C.Y., Lu, Z.W., He, W.M., Ba, D.X., Wang, Y., Gao, W. & Dong, Y.K. (2007). Theoretical study on temporal behavior of Brillouin-enhanced four-wave mixing. *Acta Phys. Sin*. (in Chinese) **56**, 229–235.

Zhu, C.Y., Lu, Z.W., He, W.M., Guan, J. & Xu, X.C. (2008). Brillouin-enhanced four-wave mixing phase conjugation mirror with large signals. *Chinese J. Lasers* **35**, 845–848 (in Chinese).

https://doi.org/10.1017/S0263034611000644 Published online by Cambridge University Press